Elasto-plastic collapse load analysis of single mitred bends

Aliyu Shazali Mohammed

Civil Engineering

June 1995

Abstract

As a primary aim of this study, solution procedures have been developed for nonlinear analysis of Single Mitred Bends. An analysis of single mitred bends made of anisotropic material typical of metal matrix has also been considered. An assumed displacement finite element approach, based on the degenerate shell concept that incorporates bending-extensional coupling and some measure of transverse shear deformation is adopted. Attention has been devoted to achieving a computationally efficient mesh and an accurate numerical integration across the thickness of the single mitred bend.

A special purpose computer PLAMBS7 has been developed. A number of problems have been analyzed and results compared with solutions elsewhere in the literature. The range of problems included elastic, elasto-plastic, and elasto-anisotropic single mitred bends under pressure or in-plane bending. For the bending load, he effect of large deformation in relation to opening and closing moments on the elasto-plastic response of the mitre model has been explored.

Elasto-Plastic Collapse Load Analysis of Single Mitred Bends

by

Aliyu Shazali Mohammed

A Thesis Presented to the

FACULTY OF THE COLLEGE OF GRADUATE STUDIES

KING FAHD UNIVERSITY OF PETROLEUM & MINERALS

DHAHRAN, SAUDI ARABIA

In Partial Fulfillment of the
Requirements for the Degree of

MASTER OF SCIENCE

In

CIVIL ENGINEERING

June, 1995

ELASTO-PLASTIC COLLAPSE LOAD ANALYSIS OF SINGLE MITRED BENDS

BY

ALIYU SHAZALI MOHAMMED

A Thesis Presented to the

FACULTY OF THE COLLEGE OF GRADUATE STUDIES

KING FAHD UNIVERSITY OF PETROLEUM & MINERALS

DHAHRAN, SAUDI ARABIA

In Partial Fulfillment of the
Requirements for the Degree of

MASTER OF SCIENCE

In

CIVIL ENGINEERING

June, 1995

KING FAHD UNIVERSITY OF PETROLEUM & MINERALS
DHAHRAN, SAUDI ARABIA.

COLLEGE OF GRADUATE STUDIES

This thesis, written by

Aliyu Shazali Mohammed

under the direction of his Thesis committee, and approved by all its members, has been presented to and accepted by the Dean, College of Graduate Studies, in partial fulfillment of the requirements for the Degree of

Master of Sciences in Civil Engineering

Thesis Committee :

Dr. Abdulrahman A. Khathlan (Chairman)

Prof. Mohammed H. Baluch (Member)

Dr. Husain J. Al-Gahtani (Member)

Dr. Alfarabi M. Sharif (Member)

Dr. Alfarabi M. Sharif
Department Chairman

Dr. Ala H. Al-Rabeh
Dean, College of Graduate Studies

Date: June 1995

Dedication

for the blessing of *ALLAH* (SWT)

&

the graceful and guiding prayers
of *Safiya S. Othman*, my mother

Acknowledgement

I wish to express my appreciation to Dr. A.A. Khathlan who served as my major advisor for his critique and advice that enlightened the labor of this work. I also wish to thank the other members of my Thesis Committee: Prof. M.H. Baluch, Dr. H.J. Al-Gahtani, and Dr. A.M. Sharif for their advice and suggestions.

It has been a pleasure working with everyone at Civil Engineering Department. I want to especially thank the *Finite Element Computing and Damage Group* being headed by Prof. M.H. Baluch for my participation.

Acknowledgement is due to King Fahd University of Petroleum and Minerals (KFUPM) for the support of this research. The help and computing facilities offered by the Data Processing Center (DPC) at KFUPM is appreciated.

I also owe my research effort to my home country, *Nigeria*, and my state, *Kano*, who nurtured and structured my studies into the present level.

My deep appreciation must be extended to my parents *Muhammad. N. Is'haq* and *Safiya S. Othman* and my uncle *Umar Is'haq* for their support and encouragement when at times it must have been difficult. My thanks also go to my sisters and brothers: especially *Ibrahim N. Muhammad* for his gentle but firm guidance. And to all my friends who saw less of me and kept asking when it would finish: well, may *Allah* (SWT) bless, it's finished!

Contents

List of Tables

List of Figures

Abstract

Name: Aliyu Shazali Mohammed
Title: Elasto-Plastic Collapse Load Analysis of Single Mitred Bends
Major Field: Structural Engineering
Date of Degree: June, 1995

As a primary aim of this study, solution procedures have been developed for nonlinear analysis of **Single Mitred Bends**. An analysis of single mitred bends made of anisotropic material typical of metal matrix has also been considered. An assumed displacement finite element approach, based on the degenerate shell concept that incorporates bending-extensional coupling and some measure of transverse shear deformation, is adopted . Attention has been devoted to achieving a computationally efficient mesh and an accurate numerical integration across the thickness of the single mitred bend.

A special purpose computer program **PLAMBS7** has been developed. A number of problems have been analyzed and results compared with solutions elsewhere in the literature. The range of problems included elastic, elasto-plastic, and elasto-anisotropic single mitred bends under pressure or in-plane bending. For the bending load, the effect of large deformation in relation to *opening* and *closing* moments on the elasto-plastic response of the mitre model has been explored.

Master of Science Degree
Department of Civil Engineering
King Fahd University of Petroleum and Minerals
Dhahran, Saudi Arabia
June 1995

خلاصة الرسالة

اسم الطالب الكامل : علي شاذلي محمد

عنوان الرسالة : التحليل المرن - اللدن لحمل انهيار الأكواع الأحادية

التخصص : الهندسة الإنشائية

تاريخ الشهادة : يونيو ١٩٩٥م

تهدف هذه الدراسة إلى إيجاد طرق حل وتحليل غير خطي للأكواع الأحادية ، وقد أخذ في الاعتبار تحليل الأكواع الأحادية والمصنوعة من مواد غير متماثلة في جميع الاتجاهات . تم استخدام طريقة الشرائح الحدية والتي بنيت على مفهوم التفسخ القشري والمحتوية على الانحناء المتمدد وبعض التشكل الناتج عن القص العرضي . تم تكريس الاهتمام للحصول على شبكة فعالة حسابياً وتكامل عددي دقيق عبر سُمك الأكواع الأحادية .

تم عمل برنامج حاسوب متخصص والذي عن طريقه تم تحليل عدد من المسائل ومقارنة النتائج بالأخرى المتوفرة . ومن المسائل التي تم دراستها الأكواع الأحادية المرنة ، المرنة اللدنة والمرنة الغير متماثلة في جميع الإتجاهات تحت الضغط أو الإنحناء المستوي . وبخصوص أحمال العزوم فقد استكشف تأثير التشكلات الكبيرة المرتبطة بعزوم الإنحناء الفاتحة والغالقة على الاستجابة المرنة - اللدنة لنموذج الكوع .

درجة الماجستير في العلوم

جامعة الملك فهد للبترول والمعادن

الظهران ، المملكة العربية السعودية

يونيو ١٩٩٥

Chapter 1

INTRODUCTION

1.1 Background Details

Single mitred bends are essential components of high pressure vessels and piping systems. They are used widely in such fields as oil. nuclear, chemical, power and marine engineering. In such systems, mitred bends are chiefly employed to accommodate necessary configurational constraints as well as to give an added flexibility to the system so that reactions impinged on other critical vessel parts are kept as low as possible. Sufficient number of smooth bends can, in principle, be used to provide a certain level of flexibility. However where large diameter pipes are involved smooth bends increasingly become ineffective and are also difficult to construct. Hence mitred bends—of the single, or multi types, are introduced to provide a cheaper and practical solution than smooth bends.

In other situations, space in which piping systems are located is at premium or somewhat restricted and this necessitates the use of mitred bends. Their perceived advantage and space economy in this regard is a prime motive for the industrial application of mitred bends. Such technical applications of mitred bends have been promoting a high demand for further studies. Accordingly,most of the recent work on mitred bends has been enhanced by a desire to predict stress. stiffness or flexibility, and limit-loads in relation to

the mitre geometry which is quite unique from other piping system or vessel components.

1.2 Geometry and Definition of Bends

Geometrical details relating to the types of bends occurring in a typical piping system setup are principally identified in Fig. 1.1. The figure identifies a multi-mitred bend as consisting of a number of closely spaced obliquely-edged cylindrical segments called the mitred segments. A single mitred bend. on the other hand, is simply formed when two of the obliquely-edged cylindrical segments, obtained by slicing a straight cylindrical pipe segment at an angle. are joined or welded together along the oblique edge. The oblique edge is also known as a mitre-joint, mitre-plane or *mitre-edge*. An important parameter to a mitre problem is the *mitre-angle* α which is the angle subtended by the mitre-edge and a plane normal to one of the mitre segment axis (the normal-plane), see Fig. 1.1.

A further look at the mitred bends geometries undoubtedly suggests a sense of difficulty in their analysis than do smooth bends. The latter are simply toroidal in shape while the former are uniquely different. In terms of mechanical behavior, mitred bends are different from smooth bends, though in the limiting case a multi-segmented bend may permit simpler treatment when analyzed as a derived smooth bend. One explanation for the latter is because when an in-plane bending moment is applied to a multi-mitred bend, the mitre-edge would flatten in a manner similar to that arising when a smooth bend is subjected to a similar loading. Hence the limiting similarity.

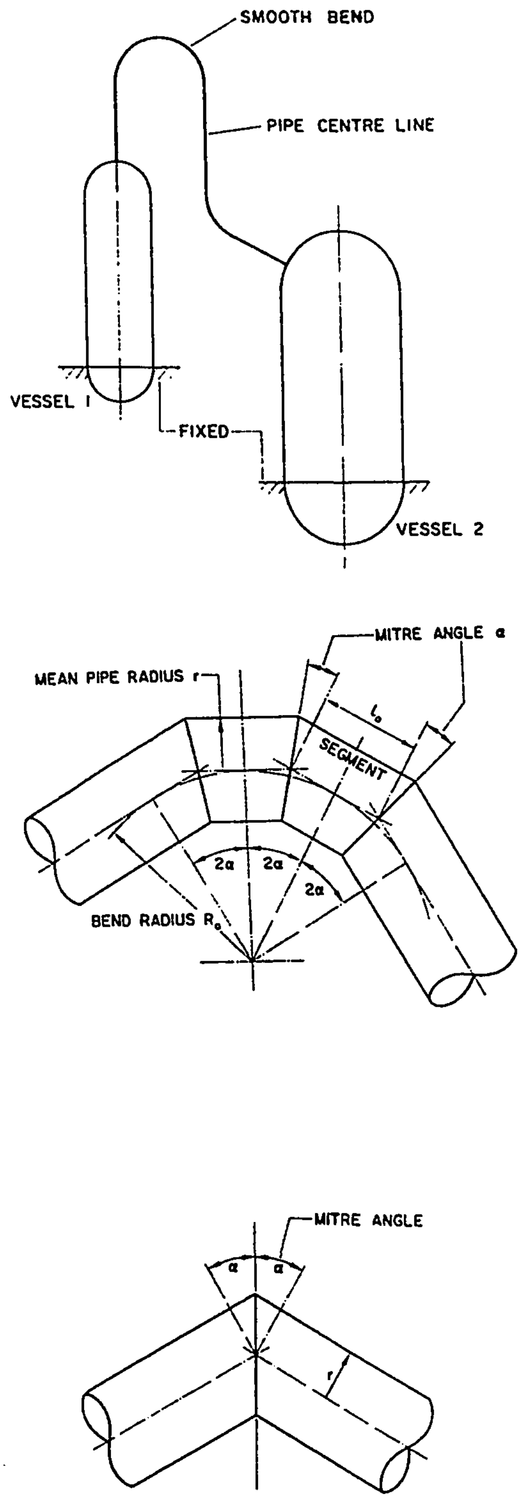

Figure 1.1: Mitre systems and geometry [1] (a) smooth bend (b) multi-mitred bend (c) single mitred bend.

1.3 Response Behavior of Mitred Bends

Generally when bends are included in a piping system they have the desirable effect of allowing greater flexibility in the system. Under in-plane bending moment such response implicitly manifests as a decreased nominal bending rigidity for mitre sections close to the mitre-edge. With a characteristic shell behavior, this gain in flexibility gradually decays down with sections remote from the mitre-edge. In the vicinity of the mitre-edge large reactive forces are however encountered. The latter has been of major concern and therefore a source of various other investigations.

Depending on the loading situation upon the mitred segment, the reactions around the mitre-edge may exert internal forces with normal or shear components; bending moments with components which bend the mitre segments in, or perpendicular to, the plane containing the mitre segments axes; and twisting moments may also exist. The behavior of straight cylindrical length of pipe under similar loading situation is straight forward. This is not the case for mitred bends, and not the least, smooth bends. The action of various types of these forces is to locally raise the stress level or concentration in the intersection region (the mitre-edge) with further rise in the stress concentration caused by the sharp discontinuity at the mitre-edge.

In the particular situation of in-plane bending, the increase in flexibility associated with the flattening of the mitre cross section is found to be much higher than would be predicted by simple bending theory. In the same manner, the local stresses set up in the vicinity of the mitre-edge are much larger than the simple bending theory predictions. Despite these intricacies, the peculiarities and problems of mitred bends do not simply end with such unexpected tendencies.

1.4 Problems of Single Mitred Bends

Characterized by the mitre angle (α), the sharp geometrical change occurring at the mitre-edge gives rise to different levels of local stresses or stress concentrations. These stresses exhibit rapid decay and fluctuation with respect to their amplitudes and wavelengths along the length of the mitred bend segment. Mitred bends under this condition are certainly more vulnerable to other dangers like growth of material defects, brittle fracture, enlargement of fatigue cracks and local plastification. In practical applications, single mitred bends would portray low fatigue strength at the mitre-edge; however, such dangers could not be tolerated. To circumvent these dangers, single mitred bends are often reinforced at the join plane between the two mitre segments. For unreinforced mitres, a lack of adequate information on their behavior exists. A brief overview of the latter has helped point out the need for such investigations and consequently formed the basis of the present study.

1.5 Motivations and Objective Search

From behavioral point of view, early codes gave no provision for mitred bends while later ones cater for them by formulas which are approximate and empirical. Many of these formulas were based on results obtained from fatigue tests. Closer examination of British and American piping standards revealed that no design guideline was available for high pressure application [2]. However, the application of high pressure technology has undergone tremendous growth in the industries.

Research demands, as in the study of material properties, have resulted in operation pressures measuring upto megapascals. Furthermore, most recent developments in mitred bends formation entail use of metal forming and jet

cutting under high pressure processes. Despite these, the authors of Ref. [2], BS 806 part 1, could only provide a limited guidance which until recently restricted the use of mitred bends or vessel components to design pressure not exceeding 2.1MPa. In pursuance of the problem, ASME [3] is currently extending its pressure vessels and piping code to include vessels components which operate at pressures just exceeding 1GPa.

From the foregoing discussion, the need for studies that identifies the broad context of mitre problems is imperative. A solution technique that predicts plastic response and collapse load or maximum pressure load for piping or vessel systems as well as varying degree of material properties is essential in this context. For single mitred bend design, the trade-off between safety factor, tensile strength, and wall thickness can be more efficiently optimized if such quantities like the failure loads can be deduced from the point of view of basic material properties including effects of anisotropy and strain hardening phenomena. Performing these investigations with the objective of providing complete information concerning plastification and ultimate loads, amongst other governing parameters, is a primary step for the understanding and better use of single mitred bends.

Chapter 2

LITERATURE OVERVIEW

2.1 General Introduction

Like other shell structures, stress analysis of mitred bends possesses a variety of fronts, depending upon the theory used. In general, it is not unknown that two-dimensional shell theories are inadequate for the study of certain mechanical properties associated with general shell behavior, even in the elastic sense. For mitred bends, the like of such detailed properties are distributions of displacements and stresses in relevant mitre intersections as well as composite behavior. Thus adequate prediction can be studied through three-dimensional elastic or inelastic analyses only. For the range of their applicabilities, the three-dimensional static analyses are considered benchmarks against which the two-dimensional. often theoretical, analyses can be judged. Such judgement are important particularly in cases where prediction of global mechanical properties like collapse loads are involved. Due to the complicated form of the governing equations of elasticity coupled with the intricate geometry of mitred bends, such three-dimensional analyses are theoretically impossible for the mitred bends. In the analytically theoretical sense mitre analyses have been largely approximate while in the computationally numerical sense the analysis of single mitred bends is rarely found in the literature. Nevertheless the evolution of appropriate methods

for the analysis of single mitred bends is increasingly needed to ensure the integrity of its service life.

2.2 Elastic Analysis of Mitred Bends

2.2.1 Introduction

Some commonly used analytical solutions to single mitred bends are based upon the thin-shell theories of classical mechanics, consisting of the analysis of deep and shallow shells. Several deep theories exist but the one based upon the strain-displacement relationships of Novozhilov [4] is often used. As a specialized theory of shallow shells. the simplified strain-displacement relationships of Vlasov [5] are also used. The latter method is more approximate than the former but is capable of achieving satisfactory performance.

A number of investigations for elastic stress analyses of mitred bends have been carried out. A common interest shared by these research studies concern mainly the high reactive forces or stresses that prevail in the vicinity of the mitre-edge. Depending on the loading situation upon the mitre segments the configurational changes and stress profiles in the loaded mitre would be radically different. Owing to these, and other conditional boundary intricacies, the more rigorous theoretical work to date on single unreinforced mitred bends has largely been confined to elastic analysis and to geometries approximating small mitre-angle (α).

Idealization of the mitred bends in such studies involved various assumptions that enabled the mitre to have the simplest mathematical definition which often limits the validity of the applied theoretical methods. The closeness, or otherwise, of these assumptions to experimental observations and basic cylindrical shell concepts is as varied as the different formulations involved. Generally, however, as the mitre-angle (α) increases, stress patterns

change and the approximations made to obtain the analytical solutions would make it impossible to predict experimentally observed patterns within adequate level of accuracy. For most practical applications the types of loadings considered are internal pressure and in-plane bending moment only.

2.2.2 Previous Analytical Work

2.2.2.1 Pressure Loading

The analysis of single unreinforced mitred pipe bends for this loading has received intensive research effort most especially in the sixties [6, 7, 8, 9, 10]. Owen and Emmerson [6] adopted the use of thin-shell theory to establish expressions for axial and hoop stresses in an unreinforced single mitred bend. In addition, their work included a comprehensive experimental test program of araldite model of the single mitred bends using the frozen-stress photoelastic technique. Stress distributions were reported and showed good agreement between the theoretical and the experimental values. Notably however considerable discrepancies were exhibited by the axial stresses occurring at the intrado and extrado vicinities of the mitre-edge. These discrepancies are attributable to approximations inherent in the theoretical analysis which include absence of three-dimensional effects.

Nonetheless, the work of Owen and Emmerson [6] has been considered the most comprehensive on the subject as it generally provides satisfactory predictions provided that the mitre-angle (α) is kept small. Its acceptability [2] to serve as a basis for making design proposals over the range of mitre-angle (α), upto 15^o, has been reported elsewhere [2]. Work of other investigators [11, 12, 13] were also reviewed in Owen and Emmerson paper [6]. Similar treatment was found in the work of Gill [1].

Dealing with a rigidly clamped mitred shell (for which α was therefore

arbitrary) and subjected to internal pressure, Kornecki [12] presented a solution based on equations of thin-shell theory. The solution was divided into a membrane analysis and an edge effect analysis while an asymptotic method was used for integrating the governing equations of each part of the analysis. As thin-shell theory was used, first order approximation in the thickness-ratio (inverse of the thinness-ratio, being radius/thickness ratio) is an expressed limitation of the theory. A further restriction of the analysis was the consideration of fixed (clamped) boundary condition which is not a true idealization of the mitre-edge conditions in the single mitred bend. Green and Emmerson [12], using an idea of Johnson and Reissner [14], started their analysis with the three-dimensional equations of elasticity to examine the stresses in two long cylindrical shells which were subjected to internal pressure and to bending moments applied at the ends in the plane of symmetry. Similar to the clamped oblique-edged shells, Green and Emmerson stated that their solution for internal pressure agreed well with that of Kornecki [12]. In retrospect, Owen and Emmerson [6] also reported that their work could be specialized to yield solutions similar to the perfectly clamped mitred bend, which applies for arbitrary mitre angle and is equivalent to that obtained by Korenecki [12], or similar to unstiffened mitred bends of small mitre-angle, which is equivalent to that obtained by Green and Emmerson [11].

A unique approach to a similar problem was taken by Van der Neut [13] who considered a pressurized torus with a finite number of discontinuities to approximate an oblique-edged cylindrical shell subjected to edge moments and forces which varied slowly along the oblique edge. The resulting relations were used in examining a mitre bend as cylindrical shell subjected to internal pressure for which the edge moments and forces correct for the discontinuity in geometry. The longitudinal stress given by this solution showed variations

around the circumference at sections remote from the discontinuous oblique-edge. Such variations are however not known to occur, nor are they confirmed by experiment. Not surprisingly, Van der Neut [13] himself admits that "this type of redistribution is contrary to what would be expected." An alternative approach, that was devoid of the latter problem of impossible state of stress, was presented by Murthy [7]. He examined the same mitre problem treated in [11] except that it was stiffened. The problem was overcome by assuming the mitre-angle (α) to be small such that $\tan^2 \alpha$ was neglected compared to unity. The analysis conceived of the mitre problem as being equivalent to that of a long pipe under internal pressure closed at one end and supported at an oblique-plane by a diaphragm. which is capable of resisting only forces normal to its plane. Results obtained in this way were found comparable to that of Green and Emmerson [11]. although basic shell theory equations were used, by Murthy [7], as the starting point for the rigidly connected mitred bend problem.

In investigating the problem of Kornecki [12]. Corum [8] treated a clamped oblique-edged cylindrical shell subjected to pressure and, separately, to one of other six different loading cases, namely: three mutually perpendicular moments and three mutually perpendicular forces applied at the free end. Apart from the use of basic relations of shell theory for a cylindrical shell, their work involved fewer approximations and extensive experimental results were also given. However, when compared to the experimental values, the theoretically obtained stress distributions showed substantial differences which are much more pronounced at the extrado and intrado side of the mitre-edge domain. These differences could not be unexpected because the edge effects introduced for the theoretical solutions were approximate. As in previous cases, the need for this approximation is necessitated by the difficulty in

theoretically taking proper account of the oblique mitre geometry and hence imposing appropriate boundary conditions along the oblique mitre-edge.

The problems considered by Kornecki [12] and Corum [8] are equivalent to the problem of two cylindrical shells joined over an elliptic face and reinforced by an infinitely rigid ring along the line of intersection, the mitre-edge. In a different paper, however, Murthy [9] dealt with the problem of an unreinforced intersection which is different from that of both Kornecki's and Corum's. Similar but stiffened problems were also examined earlier in Refs. [11, 13, 7]. An improvement offered by the latter work of Murthy [9] is that not much restriction is placed on the mitre-angle (α), tentatively up to 45^o as reported in the paper. Nonetheless, errors which are quite significant for moderately thick shell situations were admitted. A further limitation is that Murthy solution [9] permits results for stresses occurring at the unreinforced mitre-edge only.

2.2.2.2 In-Plane Bending

Works highlighted so far were mainly focused on internal pressure loading. In most cases, practical solutions have been reasonably achieved from such analyses, more especially for small mitre-angle up to 30^o. However, the same type of analyses do not hold good when adopted for the action of in-plane bending moments. Major attempts to directly or indirectly address the issue of in-plane bending are in Refs. [1, 15, 16, 17, 10].

An established trend was that upon application of an in-plane bending moment, mitred bends exhibit behavior similar to that of curved pipes under the same loading condition. However, the behavior of curved pipes or smooth bends is far less complex and, unlike the mitred bends, had received considerable attention and had been better understood since early studies [1].

Within the frameworks of similar studies, Jones and Kitching [15], developed an approximate analysis based on energy methods in a manner similar to that used for curved pipe in order to predict stress behavior of unreinforced single mitred bends when subjected to in-plane bending. The analysis was not completely rigorous but the simplifying assumptions involved were found to be reasonable in the light of experimental evidence that availed in their work. Nonetheless, comparison of stress distributions between the theoretical and experimental solutions for the portion along the mitre-edge was noted to show different tendencies. particularly in the intrado and extrado regions of the mitre-edge where the theory over estimates peak stresses. With the exception of the crown, the decay of stresses in the longitudinal direction, along the mitre segment, was not reported.

Theoretical works concerning in-plane bending of mitred bends had been conducted jointly and individually by Green and Emmerson [11] and Corum [8]. Experimental results obtained from another work [6] have indicated that the predictions of Ref. [11], which is based on the general three-dimensional equations of elasticity but valid for small values of mitre-angle (α), is unsatisfactory for in-plane bending. In dealing with the current aspect of loading condition, Corum [8], had presented results of his investigation using approximate methods derived from basic shell theory of cylinders. His results showed presence of significant bending from the mitre-edge upto and including the supposedly membrane zone of the mitred bend. Typical of the several assumptions involved. it is indicative of the latter phenomena that the bound of applicability of the theoretical analysis are therefore rather limited.

In a separate development. Kitching in collaboration with Bond did conduct a series of studies in order to present a method of analysis specifically for multi and single mitred bends [16, 17, 18]. Based on similar method of

approach utilizing energy method, their theoretical analyses was sought to incorporate harmonic analysis on radial displacements and Donnell's equations [19] for thin cylindrical shells. A major assumption in the analysis was in approximating the strain energy as mostly accounted by the semi-membrane or the slow axial-decay component of the deformation pattern. To this part of the analysis there must be added an edge-effect solution in order to satisfy all the boundary conditions at the obliqued mitre-edge. These assumptions are not strictly correct and the theory showed tendencies of overestimating maximum stresses.

Chan and Sanders [20] considered the use of fewer simplifying assumptions in analyzing single mitred bend subjected to pure bending moment. Obtained from thin-shell theory, their analysis employed method of matched asymptotic solutions of the derived governing equations. The analysis was noted to show strong singularity at those portion of the mitre-edge where stresses are greatest. Consequently, further assumptions had to be made in order to replace this part of the analysis by a continuous solution to the shallow shell equations. Comparison of such theoretical results with experimental results of Jones and Kitching [21] were not entirely conclusive.

2.2.3 Previous Experimental Work

2.2.3.1 Pressure Loading

Historically, engineering solutions to single mitred bend problems have often been empirically formulated using results obtained from experimental tests of the mitre models. Recourse to literature has indicated that experimental testing by use of electrical resistance strain gages. stress probing methods, and photoelastic techniques are not uncommon. Accordingly, a number of experiments have been conducted on mitred bends but for elastic pressure

loading most of the information available is contained in two investigations [6, 21].

The theoretical work of Owen and Emmerson [6] contained comprehensive experimental study carried out on single mitred bends under internal pressure. Their study used eight araldite models in which the frozen-stress photoelastic technique was used to obtain measurement of stresses in the small mitre-angle models. Provided the mitre-angle (α) is small, the theory of Ref. [11] was reported to show good agreement with the measured stresses. The only exception being at the intrados and extrados of the mitred bend where experimental values are known to be difficult to obtain and theoretical values somewhat overestimated peak stresses. As the mitre-angle becomes larger, the degree of discrepancy between theory and experiment considerably increases. Using stress probing method, Jones and Kitching [21] obtained measurements of stress in a right-angled single unreinforced mitred bend subjected to various types of loads including internal pressure. In all two models of the mitre specimens, having a thinness ratio (radius/thickness ratio) of 19, were tested.

A representative paper that has carried an experimental study of single mitred bend under internal pressure was also reported by Sawa [22]. The latter study was based on stress freezing technique and reported results showed that stress concentration occurred at the intrado side of the mitre-edge. Considerable influence of the mitre-angle (α) on the reported stress concentration values was also noted.

2.2.3.2 In-Plane Bending

Experimental works have been carried out on this related problem by Kitching [23], Jones and Kitching [21], and Kitching and Thompson [24]. The

experimental results of Ref. [23] were measured by mechanical means on a 180° mitre pipe bend in which the pipe radius to bend radius ratio was 0.3075 and the segmental mitre-angle was 22.5°. As reported in Ref. [1], assessment of results obtained from the above study did pave way for some modifications in hitherto existing theoretical methods which were needed in turn for better but subsequent experimental measurements.

Jones and Kitching [21] presented a comprehensive study on a right-angled single unreinforced mitred bend subjected to in-plane bending. A remark about this study was relayed by Gill [1]. A later inference deduced out of the study concerned its role in making obsolete a hitherto idea of using the so-called equivalent smooth bend radius as an empirical means of designing mitred bends based on prevailing design codes meant for smooth bends only. In another investigation, Kitching and Thompsom [24] conducted measurements of strain, transverse deflection and change in radius on two sizes of single unreinforced mitred bends under in-plane bending. For each of the two sizes, three different mitre-angle specimens were used and observations made with various combinations of leg lengths for each of the specimens. In their concluding remarks, the above authors expressed disquiet quite similar to the one mentioned above about the use of the equivalent smooth bend radius in design of mitre bends. Entailed limitations regarding the use of the equivalent bend concept for short lengths of the mitre segment has been particularly highlighted. However, notwithstanding the entailed limitations, cautious recommendations and procedures were also given in the work of Kitching and Thompsom [21].

Parallel to the forgoing developments, Corum [8] used an epoxy resin cylindrical model having a radius to thickness ratio (thinness ratio) of 15 and inclined at an angle of 45° in order to test the applicability of his theory

to a relatively thick cylindrical shell with such a large angle of inclination. The experimental setup was instrumented with strain gages and tested under in-plane bending mode and, separately, under other loading modes that were been investigated together. Consistency in loading was ensured because of later comparison which was found reasonably good for the majority of the loads. For sufficiently thin shell situations, Corum [8] pointed that his theoretical results would provide satisfactory solution for all the seven loading modes that were considered in the study.

The use of photo-elastic stress freezing technique for the study of stress distribution in mitred pipe bends subjected to uniform in-plane bending was reported in the work of Sawa [25]. A bend angle of 90° (mitre-angle of 45°) with twelve combinations of wall thicknesses and fillet radii were all together tested. A wide range of results, including reinforcing effect of the fillet radius at the bend portion of the mitre on the stress concentration factors, were reported and discussed.

Similar elastic experimental studies on single mitred bends have been reported in Refs. [6] and [18]. However expressed limitations on these and indeed other experimental studies generally concern experimental imperfections of manufacture, like out-of-circularity of pipe: variation of pipe wall-thickness; welding imperfections: reinforcing effects of weld; and non-linearity of stress distribution across the wall-thickness of the mitre shell occuring at positions close to the the mitre-edge.

2.2.4 Previous Numerical Work

Analysis of mitred bend problems is an area that is typical of fatigue and similar hot-spot problems [26, 27. 28. 29, 30], and [31, 32, 33, 34, 35] which have benefitted from the power and advancements in digital computing. Survey

of the available literature have revealed that various forms of finite element methodologies have been employed for the stress analysis of several class of high-pressure piping system components [36, 37, 38]. Specifically, however, only a few of the surveyed literatures [39, 40, 41, 42, 17] were concerned with the analysis of mitres and the ones principally on single mitred bends are even fewer and they have not been comprehensive. The published literatures on single mitred bend were found mainly dealing with elastic analysis and internal pressure or in-plane bending [42, 17, 40, 41].

The early work of Kitching and Bond [17] included a computer program developed for efficient analysis of multi-mitred bend based on related theoretical work conducted by Kitching [16]. A number of refinements were made possible by the computer program. Presently, the development of the finite element method as an effective tool of analysis has permitted a new trend to emerge in the formulation and solution of mitre problems. The desire to accurately represent the stringent boundary conditions and the unique geometry at the mitre-edge as well as the ability to model various loading conditions with ease has been a prime factor in the emerged trend. Following this trend, Pan et.al. [40] presented a three dimensional stress analysis of mitred elbows. The doubly-curved triangular thin-shell elements of the MARC [43] finite element fleet was used for the study. A feature of the study was the formulation of seven reference load cases that would serve as unit loads for any later investigation involving combination of similar loads as might be considered for the mitred elbow.

In 1984, a new finite ring element method was proposed by Watanabe and Ohtsubo [41]. This element was a refined extension of a similar one developed in a separate work [38] by the same authors. The refined element was specially derived to enhance efficient analysis of mitred pipe bends. A

range of numerical data obtained from the study was also used to provide empirical formulas for flexibility and stress indices for in-plane and out-of-plane bending of the mitred bend. A limitation, though, of their element was its failure to respond to zero strain mode and therefore could not satisfy the correct representation of rigid body motion or condition of zero membrane strains. Despite its acclaimed efficiency, their element was reported to be computationally expensive elsewhere [36].

The use of semi-analytical concepts for the analysis of single mitred bends was proposed by Khathlan [42] in the early nineties. An obvious reason behind this somewhat mixed/hybrid formulation is to combine the advantages of both the analytical and the numerical methods in an optimum way. The approach also offered added flexibility in overcoming mitre associated difficulties and the limiting simplifying assumptions for achieving better performance and results. The method was used to examine stresses in a single mitred bend under internal pressure or in-plane bending. Stresses can only be determined at the plane of the joint (the mitre-edge) but results showed good agreement for the tested range of mitre-angle, (α), upto 45°.

A numerical study of mitred bend under pressure loading was also reported by Skopinski and Mellorovich [39]. Finite element analysis incorporating thin-shell theory in the Novozhilov [4] variant was used. Based on this, a development was made of a four-angled element of arbitrary shell rotation whose characteristics were further determined using the Khellinger-Reissner change in variable principle. The overall algorithm was found feasible and experimental model studies were also carried out for approbation of the numerical analysis. Only a few distribution of stresses were reported and the degree of correlation between the experimental and the numerical results was apparently inadequate. The work of Cook [37] was an attempt to find

a simple yet efficient numerical idealization of a pipe elbow problem. He employed a standard asymmetric analysis which was augmented by a single global degree-of-freedom, a technique regarded as an expression of the global-local method [44]. An entailed deficiency of the study is that loads must not vary in the circumferential direction and thus proper modelling could not be achieved for end force on the 90^o pipe bend.

So far, various literature reviews directly related to the study have been presented to clearly indicate important aspects involved in mitre analysis. Typical of the review, mitre analyses, whether in the experimental, theoretical, or computational sense, are largely confined to elastic rather than inelastic behavior. Implied limitations towards this is apparent in recent codes which tend to restrict the design of mitre components to the effect of guarding against gross plastic deformation or delayed shakedown to elastic action under service conditions. Satisfaction of these requirements would inadvertently result in conservative and grossly uneconomical design. However, this is not surprising but only serve to explain the fact that difficulty do really exist in ascertaining the complexities of the oblique mitre-edge as well as its acute influence on both local and gross behavior of the mitred bend—most especially during the post-yield phase. To improve upon stated offerings as well as to ensure the safety, reliability, and continued mitre usage, current research efforts have begun to show similar tendencies and interest in that direction. Taking proper cognizance of this has been an important haul-mark of the present study.

2.3 Current Trends

2.3.1 Introduction

Despite the hyper-sensitive nature of mitred bends in the pressure vessel or piping systems, mitred bends must safely sustain various effects of thermal and mechanical loads. Under the effect of these loading situations the response of the mitre would take a variety of forms, the simplest of which is elastic behavior. If however the vessel structure undergoes elasto-plastic deformations, several complicated possibilities may arise. The structure may shakedown to elastic action, may incur alternating or reversed plasticity, or may lead to ratcheting behavior sometimes called "progressive deformation" or "progressive failure".

In practical applications, all these kinds of behavior can occur to a certain degree which therefore make the response of the mitre structure very complicated. Hence, not surprising, only a few such problems which are associated with the simplest idealization were solvable analytically upto the present [45, 46, 47, 48]. However, an informative review in this regard have shown that experimental and theoretical studies concerned with providing a better understanding of similar yielding characteristics were reported for thick-walled cylindrical vessel subjected to burst pressure [49]. A strain-to-failure theory which ensured complete monitoring of expansion characteristics upto and including the burst pressure was considered in the theoretical study. Similar, albeit numerical, treatment of the problem was conducted by Logman and Wahab [3]. They employed incremental theory of plasticity for which Mendelson [50] method of successive elastic solutions to the elastoplastic and residual stress problems were utilized. On the basis of Hodge plastic yield condition, the problem of limit analysis of circular cylindrical shells having different boundary conditions was considered for analytical solution

by Cinquini [51]. His solution was complete in the sense of the limit analysis theory. Although the just mentioned studies were geometrically less complex, an interesting point noted out of it was that different yield conditions and methods of solution including linear programming were feasible within the frame of plasticity studies [52, 53].

In seeking a rational basis for the elasto-plastic study of single mitred bends, considerations based on purely analytical treatment, as was the case for the cited simpler geometries, would be much more frustrating if not entirely untenable. In this regard the analytical approach should be complemented by a systematic numerical tool and a limited number of experiments. The latter are required for verification purposes only. For the former, the use of finite element method has achieved prominence owing to the ease with which complex inelastic behavior can be dealt with.

2.3.2 Elasto-Plastic Mitres

The most recent report on numerical investigation into the plastic collapse of single mitred pipe bends was given by Kitching, et.al. [54] for in-plane bending only. Typical of such analyses, the investigation was carried out using a powerful general purpose finite element program called ABACUS [55]. The element type employed for the discretization of the unreinforced single mitred bend was the isoparametric doubly curved quadrilateral element. Both material and geometrical nonlinearities were considered but no strain hardening was assumed for the analysis. Results of the analysis were used for comparison with a parallel experimental study conducted on two models, mitre-angle 30^o and 45^o, of the single mitred bends made from an aluminum alloy. Owing to a premature failure of the 30^o test model, results from the experimental study were limited to the 45^o model. For the 45^o model, the

degree of correspondence between the finite element ABACUS and the experiment results was not that appreciable. Prior to material collapse, the experimental results of the 45° model showed significant strain hardening but this was not considered for the ABACUS analysis. The decision for lack of strain hardening consideration was not clear.

With the exception of the above investigation, literature search has indicated that no conclusive study has been made about the inelastic load analysis of even the simplest single mitre geometry—presumably that of mitre-angle not exceeding 15°. Those available are only problems related to pipe bends, elbows, and tubular joints, some of which have been reported to some extent [56, 57, 58, 59, 60].

In the elastic-plastic range, Hellen [56] calculated the limit moment using both the BERSAFE system [61] and experimental technique for pipe bend under in-plane bending. Bunhnell [57, 58] studied elastic-perfectly plastic behavior of pipes and elbows under pressure with bending. Calculations were performed with modified version of the BOSOR5 computer program [62] and buckling effect under external pressure was also considered. The effect of material nonlinearity on the analysis of welded elbows subjected to in-plane bending was jointly investigated by Suzuki and Nasu [59]. The four-node shell element belonging to the program ADINA [62] was used for the study. Geometrical nonlinearity was included in the analysis and results obtained were closely confirmed by experiment. Moreover, verification of the results with regard to response caused by opening and closing moments showed similar tendencies as those reported by Kitching, et.al [54]. Kawashima and Ito [60] numerically solved a similar problem using elastic-plastic curved tubes under simultaneous bending and axial force. The rigid body-spring model [63] was utilized in the employed numerical method.

The significance of the forgoing literature presentation lies with the demonstrated feasibilities of performing elasto-plastic analysis for the kind of structural objects under consideration. More importantly,it serves to indicate the level of agreement an analyst can expect when using similar computer based methods capable of inelastic analysis. Before concluding the literature survey, it has been of interest to the present study to consider the problem of elastic stress analysis in anisotropic mitres.

2.3.3 Elastic Anisotropic Mitres

The existence of literature on the above aspect of single mitred bends is scarce and not known to the present study. Thus, both theoretical and experimental limitations exist with regard to analysis and characteristic response of single mitred bends stacked with arbitrary fiber orientations. A dual report recently relayed jointly by Kitching and Hose [64, 65] was primarily concerned with smooth bends. Even for the smooth bends, this type of study had not been investigated before.

Extending an earlier method adopted by Kitching and Bond [17], Kitching and Hose [65] presented an approach for analytical analysis of anisotropic pipe bends subjected to an in-plane bending moment. To enhance computation a computer program was written to solve the linear simultaneous equations that were derived. Derivation of the equations was based on minimization of the total potential energy in the system considering constant flattening analysis [17, 1]. Close agreement of results was observed when compared with experimental measurements obtained for the range of the analyzed geometries. However outside strains(stresses) at the crown of the bend appeared over-predicted. In another investigation [64], the effect of the variation of mitre wall-thickness was studied by the joint authors. In the

latter study, Kitching and Hose [64] used an appropriate laminate theory incorporating an extension of their earlier work [65]. Results were expressed in closed form, and their practical implications were discussed. Terms such as wall thickness, flexural modulus and transverse shear modulus were shown to impact a profound effect relative to those anticipated in a straight pipe having the same construction and subjected to pure bending moment. These variations are not unrealistic but highlight the importance of similar tendencies expressed elsewhere in the literature [66, 67, 68].

Though confined to simpler geometrics and in-plane bending, the works in Refs. [65, 64] furnished useful arguments that showed the relevance of such an investigation towards anisotropic mitres. The arguments indicated strong correlation that is in tune with recent interest and increased usage of advanced fibrous materials. With this in place, the broader and specific objectives of the present research study are conveniently expressed in the following section, with subsequent chapters achieving the realization of these objectives upto application.

2.4 PRESENT STUDY

2.4.1 Introduction

In the preceeding sections, a cross examination of problems and limitations concerning mitre analysis have been highlighted. Reported works on elastic mitres were preponderant, but those on inelastic mitres were rather restricted. Many of the works on elastic mitres possess limitations of some kind and they failed to embrace analysis which takes full advantage of recent practical applications associated with material nonlinearities, anisotropic behavior, extreme loading situations, and combination of these. Closer study of the reported analytical works showed persistent problem of assessing the

reliability of hot-spot stresses because behavior in these areas is propitiously inelastic. In order to develop a methodology suitable for this level of extraction, the feasibility of the finte element method would rather become more obvious. The relative ease with which complex geometrical, material and associated loading nonlinearities can be dealt with by the finite element method is one of the key factors of its prominence. Its versatility and successes towards nonlinear analyses in practice is well documented [69]. The present study is, therefore, an attempt to broadly permit an effective analysis of single mitred bends without restriction on geometry, material property, boundary and loading conditions.

2.4.2 Scope Specification

As the title, **Elasto-Plastic Collapse Load Analysis of Single Mitred Bend** ,indicates, the primary scope of this study is focused on developing a solution procedure for a complete elasto-plastic analysis of single unreinforced mitred bends. Inherent in this level of extraction is the prediction of plastic collapse load at which the mitre structure is deemed to behave in a fully (perfectly) plastic manner.

Based upon the finite element discretization, special attention would be paid in the study to achieve a computationally efficient element mesh that could offer the ability to obtain satisfactory simulation of the mitre model. A relatively wide selection of element based on three types of basic-elements together with their transition counterparts is therefore provided. Following this, the problem of numerical integration across the wall thickness of the single mitred bend will be assessed for its applicability to the problem in an optimal manner.

Consistent with acquiring greater generality, the on-going study will ex-

tend to cover the analysis of literature-scarce situations of elastic-anisotropic mitres. Being a pioneer one, this aspect of anisotropic single mitred bend analysis was never investigated. Accommodation of variable material properties for the anisotropic mitre construction would be made possible by the layered approach.

Another important expedition of this study is the consideration of geometrical nonlinearities that arise due to large deformation in the mitre analysis. A key interest for the geometrical inclusion is in assessing the influnce of *opening* and *closing*-moments on the post-yield response characteristics of the single mitred bend subjected to in-plane bending.

Therefore by way of fulfilment the broader scope of the present research study; as may be seen from the point of view of stress, material and/or geometric synthesis of single mitred bends, has been intended to permit investigation of :

1. elasto-plastic behavior of single mitred bends;
2. collapse load prediction with respect to experimental definitions;
3. maximum elastic stresses (or stress concentration factors) in single unreinforced mitred bends;
4. effect of loading types (pressure and in-plane bending) on maximum elastic stresses and post-yield behavior of mitred bends;
5. influence of mitre-angle α as an important characteristic of single mitred bends;
6. influence of mitre thinness-ratio (a/t);
7. differences between simple isotropic, transversely isotropic and cross-ply elastic-anisotropic single mitred bends;

8. feasibility of simple-layered approach to the mitre analysis;

9. computationally efficient and stable meshing strategy including development of transition elements; and

10. the effectiveness of the proposed enhanced numerical integration across-the-thickness.

Central to the study is the creation of a FORTRAN based computer program that implements the relevant developments. This special purpose program is called **PLAMBS7** which stands for Plastic Load Analysis of Mitred BendS and the seven (**7**) represents the latest version number in the program development sequence. Special features and programming logic of **PLAMBS7** are highlighted later and verification of the code will be made on representative set of problems. For all practical intent, the range of mitre problems to be treated using **PLAMBS7** involved internal pressure and in-plane bending moment only.

Chapter 3

COMPUTATIONAL ELASTOPLASTICITY

3.1 Introduction

3.1.1 General

In this chapter, ideas underlying the formulation of theoretical relations for a general continuum within the realm of the degenerate shell concept would be discussed. Included in the formulation is establishment of elasticity relations which take into account material nonlinearity in the elasto-plastic sense. A full Huber-Mises yield criterion is then employed.

Following the developments of Owen and Figueiras [70], the initial stiffness approach, the tangential approach and the combined approach are adopted. In addition, an associated flow rule based on the assumption that the plastic potential is the anisotropic yield function is used to define the elastoplastic incremental constitutive relations. Consolidation of these concepts is here been made as a prelude to similar but computational treatment presented in subsequent chapters.

3.1.2 Basic Requirements

Essentially, plastic behavior is characterized by an irreversible straining which is not time dependent and which can only be sustained once a certain level of

stress has been reached. In this regard, the mathematical theory of plasticity [71] has been used to provide a theoretical description of the relationship between stress and strain for such a material which exhibits an elastoplastic response.

In order to formulate a nonlinear theory governing elastoplastic material response, three requirements have to be met:

1. An explicit relationship between stress and strain must be formulated to describe material behavior under elastic conditions— before the onset of plastic deformation.

2. A yield criterion, indicating the stress level at which plastic flow commences, must be postulated.

3. A relationship between stress and strain must be developed for post yield behavior— when the deformation is made up of both elastic and plastic components.

However, it has been noted that a general theory which is applicable to different classes of nonlinear materials is not yet established [72, 70]. In the course of the present study, the Huber Mises law which closely approximates to the metal plasticity behavior is found suitable.

3.2 Elastic Laws

3.2.1 Generalized Hook's Law

Anisotropic materials consisting of unidirectional fibers embedded in a matrix are of interest in this study. For the most general case of anisotropy the number of independent elastic constants is 21. but this number is considerably reduced if the material internal composition possesses symmetry of any kind [72, 70, 73].

Consequently, a state of anisotropy which possesses three mutually orthogonal planes of symmetry at each layer is assumed. Fiber reinforced composite structures almost invariably possess this kind of symmetry—with the mid-layer surface being a symmetric plane at each point. Implicit in the fiber construction is the assumption that the shell thickness consists of perfectly bonded layers whose principal material properties can be transformed with respect to a specified local reference coordinate axes. By taking the subscripts *1,2 and 3* as referring to the principal material axes (m-axes) of anisotropy and that the axes coincide with the local reference system of orthogonal axes (r-axes: x, y, z), the equations of the generalized Hook's law can be written as:

$$\underline{\sigma}_m = \underline{D}_m \underline{\epsilon} \tag{3.1}$$

where $\underline{\sigma}_m$ and $\underline{\epsilon}_m$ are vectors of stress and strain respectively, $\underline{D}_m$ is a *6 x 6* matrix of elastic constants. To allow for 'degeneration' process, it is assumed that the resultant stress in the out-of-plane direction (z-direction) is zero, i.e. $\sigma_3 = \sigma_z = 0$. The explicit expression of the vectors involved (in m-axes) is then:

$$\begin{aligned} \underline{\sigma}_m &= [\sigma_1,\ \sigma_2,\ \tau_{12},\ \tau_{13},\ \tau_{23}] \\ \underline{\epsilon}_m &= [\epsilon_1,\ \epsilon_2,\ \gamma_{12},\ \gamma_{13},\ \gamma_{23}] \end{aligned} \tag{3.2}$$

and

$$\underline{D}_m = \begin{bmatrix} \overline{D}_{11} & \overline{D}_{12} & 0 & 0 & 0 \\ & \overline{D}_{22} & 0 & 0 & 0 \\ & & \overline{D}_{33} & 0 & 0 \\ & symm. & & \overline{D}_{44} & 0 \\ & & & 0 & \overline{D}_{55} \end{bmatrix}$$

where

$$\begin{aligned}
\overline{D}_{11} &= E_1/\Delta \\
\overline{D}_{22} &= E_2/\Delta \\
\overline{D}_{12} &= E_2\nu_{12}/\Delta \\
\overline{D}_{33} &= G_{12} \\
\overline{D}_{44} &= k_1 G_{23} \\
\overline{D}_{55} &= k_2 G_{23}
\end{aligned} \tag{3.3}$$

and

$$\Delta = 1 - \nu_{12}\nu_{21}$$

The terms k_1 and k_2 are shear correction factors in the $\overline{13}$ and $\overline{23}$ planes, respectively. These are well defined in Ref. [70].

3.2.2 Coordinate Transformation

Generally, the principal axes of anisotropy (m-axes: 1,2,3) are not oriented without a certain angle θ with respect to the local reference axes (r-axes: x,y,z). Therefore the new constitutive relations of Eq. 3.1 for such situation must be transformed from the principal material axes (m-axes:) into the local reference axes (r-axes). Noting that a cartesian operator transforms [74] local strains (ϵ_r) into principal ones (ϵ_m) according to:

$$\underline{\epsilon}_m = \underline{T}_\epsilon \epsilon_r \tag{3.4}$$

the invariance of the stress virtual work yields:

$$\underline{\sigma}_m = \underline{T}_\sigma \sigma_r$$

$$= \underline{T}_\epsilon^{-1T}\sigma_r \tag{3.5}$$

while the invariance of the elastic strain energy density gives:

$$\underline{D}_r = \underline{T}_\epsilon^{\,T}\underline{D}_m T_\epsilon \tag{3.6}$$

where

$$\underline{T}_\epsilon = \begin{bmatrix} \underline{T}_{\epsilon 1} & 0 \\ 0 & \underline{T}_{\epsilon 2} \end{bmatrix} \tag{3.7}$$

in which

$$\underline{T}_{\epsilon 1} = \begin{bmatrix} \cos^2\theta & \sin^2\theta & \sin\theta\cos\theta \\ \sin^2\theta & \cos^2\theta & -\sin\theta\cos\theta \\ -2\sin\theta\cos\theta & 2\sin\theta\cos\theta & \cos^2\theta - \sin^2\theta \end{bmatrix} \tag{3.8}$$

and

$$\underline{T}_{\epsilon 2} = \begin{bmatrix} \cos\theta & \sin\theta \\ -\sin\theta & \cos\theta \end{bmatrix} \tag{3.9}$$

From Eq. 3.1, Eq. 3.4 and 3.5 we can write:

$$\underline{\sigma}_r = \underline{D}_r\underline{\epsilon}_r \tag{3.10}$$

where $\underline{D}_r$ is a transformed elasticity matrix in local reference frame. whose form, as given in Eq. 3.6, becomes:

$$\underline{D}_r = \begin{bmatrix} D_{11} & D_{12} & D_{13} & 0 & 0 \\ & D_{22} & D_{23} & 0 & 0 \\ & & D_{33} & 0 & 0 \\ & symm. & & D_{44} & D_{45} \\ & & & & D_{55} \end{bmatrix} \tag{3.11}$$

3.3 The Yield Criterion

3.3.1 Generalized Huber Mises Law

For the present study, the outset of material nonlinearity is based on the full three-dimensional Huber-Mises yield criterion which has been generalized

to consider anisotropic metals [72, 70]. In its general form, the criterion determines the stress level at which plastic deformation begins according to:

$$F(\sigma, \chi) = f(\sigma) - Y(\chi) = 0 \tag{3.12}$$

in which f is function of the deviatoric stress invariants and the yield level Y is a function of hardening parameter χ. By defining the plastic potential, or effective stress, $\overline{\sigma}$, in a manner similar to Huber-Mises yield function for anisotropic materials, the following can be written:

$$\begin{aligned} f = \overline{\sigma}^2 &= [\alpha_{12}(\sigma_{11} - \sigma_{22})^2 + \alpha_{23}(\sigma_{22} - \sigma_{33})^2 \\ &\quad + \alpha_{13}(\sigma_{33} - \sigma_{11})^2 + 3\alpha_{44}\tau_{12}^2 + 3\alpha_{55}\tau_{13}^2 \\ &\quad + 3\alpha_{66}\tau_{23}^2] \end{aligned} \tag{3.13}$$

where the σ's are stress components, the α's are the additional so called anisotropic parameters. The subscripts *1,2,3* refer to the usual notation for the three principal material axes (m-axes) of anisotropy. To develop this expression, the assumption $\sigma_{33} = \sigma_z = 0$ is imposed to yield:

$$\overline{\sigma}^2 = a_1\sigma_1^2 + 2a_{12}\sigma_1\sigma_2 + a_2\sigma_2^2 + a_3\tau_{12}^2 + a_4\tau_{13}^2 + a_5\tau_{23}^2 \tag{3.14}$$

where $\sigma_1 = \sigma_{11}, \sigma_2 = \sigma_{22}, \tau_{12}, \tau_{13}, \tau_{23}$ are non-zero stress components and $a_1, a_{12}, a_2, a_3, a_4$, and a_5 are the simplified form of the anisotropic parameters which are determined experimentally. In matrix form Eq. 3.14, referred to m-axes, can be written as:

$$\overline{\sigma}^2 = \underline{\sigma}_m^T \underline{A}_m \underline{\sigma}_m \tag{3.15}$$

where $\underline{A}_m$ is the matrix of anisotropic parameters assuming the principal material axes (m-axes: 1,2,3) coincide with the local reference axes (r-axes),

and is written as:

$$\underline{A}_m = \begin{bmatrix} \overline{a}_1 & \overline{a}_{12} & 0 & 0 & 0 \\ & \overline{a}_{22} & 0 & 0 & 0 \\ & & \overline{a}_3 & 0 & 0 \\ & symm. & & \overline{a}_4 & 0 \\ & & & 0 & \overline{a}_5 \end{bmatrix}$$

3.3.2 Coordinate Transformation

In general, the principal material axes *(m-axes: 1,2,3)* do not coincide with the local reference axes (r-axes: x,y,z), but are rotated by a certain angle, say θ, Fig. 3.1. Therefore the matrix of anisotropic parameters transforms from *m-axes* to *r-axes* according to the following sequence of transformations:

$$\underline{\sigma}_m = \underline{T}_\sigma \sigma_r \tag{3.16}$$

where $\underline{T}_\sigma$ is the transformation matrix (referred to m-axes) which can be deduced from Eq. 3.5 as:

$$\underline{T}_\sigma = \underline{T}_\epsilon^{-1T} \tag{3.17}$$

and $\underline{T}_\epsilon$ is explicitly defined previously in Eq. 3.7. Using Eq. 3.16 in Eq. 3.15 the effective stress, expressed in the local reference axes (r-axes: x,y,z) is then:

$$\overline{\sigma}^2 = \underline{\sigma}_r^T \underline{A}_r \underline{\sigma}_r \tag{3.18}$$

in which $\underline{A}_r$ is the required new matrix of anisotropic parameters given by

$$\overline{A}_r = \underline{T}_\sigma^T \underline{A}_m \underline{T}_\sigma \tag{3.19}$$

which according to Eq. 3.17, becomes:

$$\underline{A}_r = \underline{T}_\epsilon \underline{A}_m T_\epsilon^{-1} = \begin{bmatrix} a_1 & a_{12} & 0 & 0 & 0 \\ & a_{22} & 0 & 0 & 0 \\ & & a_3 & 0 & 0 \\ & symm. & & a_4 & 0 \\ & & & & a_5 \end{bmatrix} \tag{3.20}$$

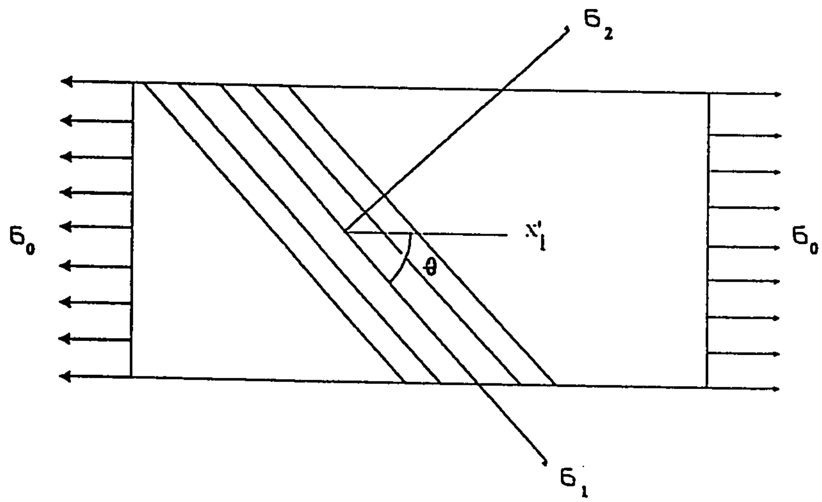

Figure 3.1: Anisotropic fiber orientation.

3.4 Elasto-Plastic Laws

3.4.1 Elasto-Plastic Model

In the present study, the approach reported by Owen and Figueiras [70], and Hinton and Owen [72], utilizing the shell stress components coupled with the extended Huber-Mises yield surface as presented in Hill [71, 75] for anisotropic materials, is followed. In this approach, equivalent, or effective stress, $\overline{\sigma}$, is first computed in conformance with the Huber-Mises criteria; then the equivalent stress level at which further plastic deformation takes place is computed to correspond to an associated plasticity theory—the Prandtl-Reuss flow rule [71] to be specific.

3.4.2 Incremental Flow Rule

The incremental flow theory is chosen for the present work over the deformation theory. This choice incurs the merits as well as the generality of the incremental flow theory most especially its suitability for adaptation in computer analysis [76]. Following this, the development of the elasto-plastic constitutive relations for the chosen displacement based finite element formulation is on the basis of incremental strains being related to incremental stress components. In developing these relations. the strain increments are assumed to be divisible into elastic and plastic components.

$$d\underline{\epsilon} = d\underline{\epsilon}^{e} + d\underline{\epsilon}^{p} \tag{3.21}$$

where $d\underline{\epsilon}^{e}$ and $d\underline{\epsilon}^{p}$ are the incremental elastic and plastic strain components, respectively. Following the developments in Refs. [77, 72],the following elasto-plastic incremental stress-strain relationship is therefore used:

$$d\underline{\sigma} = \underline{D}_{T} d\underline{\epsilon} \tag{3.22}$$

where

$$\underline{D}_T = \underline{D} - \frac{\underline{D}\,\underline{a}^* \underline{D}\,\underline{a}^T}{A + \underline{a}^T\,\underline{D}\,\underline{a}^*} \tag{3.23}$$

It is noted that the triple product terms in the numerator and denominator of the preceding equation are scalars, and thus Eq. 3.23 can be factored (with $\underline{a}^* = \underline{a}$) as:

$$\underline{D}_T = \underline{D}\left[1 - \frac{\underline{a}^* \underline{D}\,\underline{a}^T}{A + \underline{a}^T\,\underline{D}\,\underline{a}^*}\right] \tag{3.24}$$

This matrix reflects the effect of material nonlinearity on the elastoplastic behavior of the structure.

If the yield surface is defined in terms of a uniaxial stress, the scalar hardening parameter **A** can be deduced based on work hardening hypothesis and yield function. This has been found [77] to be equal to the local slope $H\prime$ of the uniaxial stress-plastic-strain curve and can be explicitly written as:

$$A = H\prime = \frac{\partial \sigma}{\partial \epsilon^p} = \frac{E_T}{1 - E_T/E} \tag{3.25}$$

In other words, the parameter **A** represents the tangent to the effective stress-plastic-strain curve and is a function of the accumulated effective plastic strain $\bar{\epsilon}^p$. æ

Chapter 4

SHELL FINITE ELEMENTS

4.1 Introduction

The development of an appropriate procedure for the determination of displacements and stress distributions in mitred bends is of fundamental importance in the prediction and assessment of the mitre strength and structural integrity. In addition to stress-singularity peculiarities, mitred bends possess unique characteristic shell behavior whose understanding from research point of view have continued to attract increased attention. Several analytical and experimental methods by which estimates of peak stresses occurring in mitre shells can be obtained have been examined. Analytical methods to the problems are limited in scope and are not, in general, applicable to arbitrary shapes, load conditions, and irregular support and boundary conditions as could be found in mitred bends. The survey of the literature has indicated that closed-form solutions were only tenable for the relatively simpler smooth bends and relatively approximate solutions for mitred bends of small mitre-angle. However, as the most viable method for analysis of similar structural objects, finite element technique is effectively handy, and could provide relative ease based on which mitre joint complexities could be dealt with. The choice of a particular shell finite element for proper discretization is important in this regard.

4.2 Curved Shell Elements

Four distinct approaches to finite element geometric discretization of generally curved shells have been in use [78]. These are based on; flat elements; asymmetric shell elements; curved elements on the basis of classical shell theories; and elements derived or degenerated from asymmetric or three-dimensional solid elements and specialized to handle thin and moderately thick shells. Depending upon the shell problem, these elements were employed by several investigators with convenience but varying degree of successes [79, 70, 78, 76, 80, 81, 82, 83, 74, 84]. Simplicity is the major attractive feature of the flat elements. However in curved shell situations, they give rise to a number of shortcomings such as the presence of discontinuity bending moments at element juncture lines which do not appear in the continuously curved actual situations. Although their range of applicability have been extended to include nonlinear effect [85]. asymmetric shell elements with straight or curved edges along the meridian are suited for the analysis of shells of revolution only.

On the basis of classical shell theories curved shell elements have been formulated with a view to overcoming limitations in the use of flat elements for shell analysis. Different shell theories had been developed from three-dimensional field equations in which various assumptions appropriate to shell behavior were incorporated. Common formulations for these include Hellinger-Reissner principle [76], Kirchhoff hypothesis [86], Mindlin and Reissner theories [87, 88, 89, 90, 91]. Similar to plate bending elements, curved elements based on Kirchhoff theory encounter difficulties of imposing continuity and compatibility requirements necessary for finite element formulation [88]. Mindlin-Reissner element bypassed these difficulties but

introduced its own problems notably that of locking [87, 89]. A somewhat different class of elements provided the semiloof plate and shell elements, and these were derived based on thin plate and shell theories. The excellent performance of these elements in vibration and stability analysis of thin shells have been reported for more sophisticated models of analysis [92, 73].

For nonlinear analysis [93] an alternative element that was found easier to apply is the degenerate element which was first presented by Ahmad et al. [90] for the linear analysis of moderately thick shells. Using the so-called degenerate process, this element was derived from an approach that avoided the complexities of fully general shell theories. It allowed direct discretization of the three-dimensional equations of continuum mechanics, a procedure known for retaining a measure of transverse shear deformation effects. Without direct recourse to any particular shell theory the approach can be applied to the nonlinear finite element modelling of arbitrary shell geometries [78, 74, 94]. Representative works that have carried over the degenerate shell formulation to geometric and material nonlinear analysis as well as to combined geometric and material nonlinearities can be found in [72, 84, 74, 83, 95, 70]. A particular application of the concept to 9-noded Lagrangian element was presented in the work of Parisch [96]. To understand clearly the various aspects involved, basic details related to the ideals of degeneracy are considered below.

4.3 Degeneracy

4.3.1 Basic Philosophy

Eversince the degenerate concept of formulating general shell elements was proposed by Ahamd et al. [93], the approach has found wide acceptance in subsequent developments of the elements [83]. This was partly due to

the need to analyze moderately thick shell problems and partly their advantages. The degenerate procedure begins by discretizing directly the three-dimensional equations of continuum mechanics. The three-dimensional formulation is then degenerated, in terms of nodal variables in the shell midsurface, by introducing the assumption that 'originals' normal to the mid-surface are inextensible and remain straight. Furthermore, normal sections do not necessarily remain normal after deformation and therefore allowing a measure of transverse shear deformation in the formulation.

The inherent hypotheses underlying the degenerate solid approach and the classical shell theory are the same except that reduction to resultant form is typically carried out numerically in the former and analytically in the latter. Obviously, the approach using classical theory directly is more complex mathematically. The degenerate formulation allows independent study of shear effects from the bending ones and only C^0-continuity isoparametric representation is sufficient in the finite element approximation. Its capability to represent the coupling effects between membrane and bending actions is another attractive feature in its use for higher order elements. In practical applications, however, degenerate based finite element formulations are not devoid of problems.

4.3.2 Locking Problems and Remedies

4.3.2.1 Shear and Membrane Lockings

Degenerate elements perform satisfactorily well when used with thick and moderately-thick shells. However their performance become rapidly deteriorated when applied to shells in the 'thin' limit. This phenomenon is called locking. Two types of locking have been identified and have been the subjects of many publications [78, 93, 97, 98, 99]. First type of locking stems

from overconstraining effect of the condition of zero transverse shear energy involved in the formulation of thin-shells. This is known as *shear locking.* A shear locked element cannot take up pure bending mode without inducing parasitic transverse shear energy which is readily in excess in the case of thin-shells. The second type of locking is known as *membrane locking* and is associated with the overconstraining effect of the condition of zero membrane strains or rigid modes in curved shells. Its physical interpretation is the inability of an element to bend without stretching and this causes bending-dominated deformation to become replaced by a membrane-dominated deformation [98].

4.3.2.2 Remedies and Limitations

To alleviate locking associated deficiencies, several techniques have been devised in many investigations [78, 100, 98, 101, 97, 83, 95, 89, 87, 96] which reduced or even circumvented shear or membrane locking. Popular techniques include but not limited to selective or reduced integration [96],heterosis elements [72, 84, 102], stabilization methods [103],discrete Kirchhoff elements [86, 88, 73, 92], mixed or hybrid formulations [101, 100, 87],covariant or assumed strain methods [97, 98, 95, 83], mode decomposition, γ-projector and free-formulations. However, there is no general concensus in favor of any particular approach due to a number of distinct limitations.

Huang and Hinton [104] recognized that even though locking in shell elements results from artificial strain energy terms that exist at all points within the elements except at reduced integration sampling points,the actual use of the reduced or selective scheme is not always successful in overcoming locking.Use of such scheme for problems with highly constrained boundaries results in matrices that are rank deficient [72, 96] and these endanger

spurious or zero energy modes called hourglass modes.To remove hourglass modes, stabilization matrices were introduced, though stabilization methods involved certain parameters which still lack physical interpretations [97].An alternative use of Heterosis was also reported.However for problems with irregular meshes overstiffening effect is said to occur and unreliable solutions may result with elements of small aspect ratio [87].

Covariant methods are very successful in the treatment of shear locking, except that in the case of higher order curved elements the approach is not readily satisfactory for membrane locking [83]. In terms of handling shear locking, it has been indicated that the hybrid or mixed approaches are equivalent to the displacement-based formulations with reduced integration [78]. Findings based on Ref. [97] also showed that use of reduced integration for shear strain often introduce the beneficial effects of reduced membrane locking. Unfortunately, such reduction is accompanied by deterioration of the membrane-bending coupling, an essential characteristics of shell behavior.

In addition to shear-locking and membrane-locking, another class of problems found in low-order shell elements is that of drilling degrees-of-freedom (DDOF) which is associated with rotations about the normal to the shell surface [105]. Reference [98] provides a useful discussion to such problems but are not of concern for the present study, however. Further upto date review specifically on locking in thin shell elements can be found in the works of Yang, et.al. [78], Parisch [96], and Choi and Paik [97].

4.4 Element Requirements

In selecting a specific type of element, a number of requirements have to be taken into consideration. The element had to be based on a three-dimensional degenerated elasticity formulation, enabling the modelling of both 'thin' and

'thick' shells. The inclusion of transverse shear deformation in the element formulation was therefore deemed essential. Furthermore the desirability of the element to be amenable to mitre models both in the linear and nonlinear situations must be upheld. The requirement of the element permissibility to geometric nonlinearity was also under consideration. Without limitation on the range of generality of the mitre joint geometry, the element must be capable of incorporating the complex mitre loading and boundary conditions.

Not to mention the cited but unforceable locking drawbacks, the selection of a particularly single degenerate shell element of the isoparametric family that could fulfill the above mentioned requirements was a difficult task. Consequently the present study has opted for three distinct types of the degenerate isoparametric elements. These elements are the 8-noded Serendipity, the 9-noded Lagrangian, and the Heterosis elements. Being formulated on sufficiently higher order in-plane displacement fields,the adopted elements possess the decided advantage of capturing high deformation gradients and modelling shells of curved irregular geometries.

Numerical study [101, 96] on the part of the 9-noded Lagrangian element has indicated its superiority over the 8-noded Serendipity element. Therefore from computational stand point of the present research study, due preference will be given to this element as much as possible. The added choice of the Heterosis element was to allay concern regarding locking problems which may plague the reliability of the 9-noded Lagrangian element.

Chapter 5

MODELS IMPLEMENTATION

5.1 Introduction

Like analysis of general shells, the finite element analysis of mitred bends can take a variety of forms. But depending upon the theory of classical mechanics used different levels of accuracy can be achieved. As a specialization of the classical theories, the present study has chosen to analyze the mitre shell using finite elements based on the degenerated solid element–known as the superparametric shell element [95]. In line with this assertion, the following treatment of this aspect of formulation basically follow the work of Hinton and Owen [72] and a similar one by Weaver and Johnston [94].

5.2 Degenerate Shell Concepts

In simple terms, degeneration process allows curved elements for shell analysis to be devised by specializing a solid element to be thin in one direction while introducing constraint conditions on nodal displacements [94]. An instance of this is where a hexahedron solid element based on a quadratic displacement field is specialized to become a quadrilateral degenerate shell element that is curved in three-dimensional space. Inherent in the degener-

ation process are the explicit assumptions that:

1. Normals to the mid-surface remain straight but not necessarily normal to the mid-surface after deformation.

2. Stresses normal to the mid-surface are negligible.

These assumptions are illustrated in Fig. 5.1. The assumption that the resultant in the the out-of-plane direction (z-direction) are zero implies that there are only five independent strains defined at a point and does not necessarily preclude the development of normal stresses if so desired in the formulation [106].

Five degrees of freedom are specified at each of the degenerated nodal points. These correspond to three displacements (u, v, w) and two rotations (β, α) of the 'normal' at each of the nodes. Thus while allowing for membrane and bending deformations, the independent definition of the rotational and translational displacement degrees of freedom permits a measure of transverse shear deformation which is deemed essential for moderately thick shells.

As described in Ref. [72], the above approach is equivalent to using a general shell theory and that it reduces to the hypothesis of Mindlin [90] and Reissner [91] when applied to plates. In other words the first assumption constitutes a tacit statement that Mindlin/Reissner plate theories also prevail in the foregoing formulation. In addition, the present approach facilitates the inclusion of different yield criteria since the difficulties involved in defining a yield condition and flow rule in terms of stress resultants in the classical theory do not arise [76].

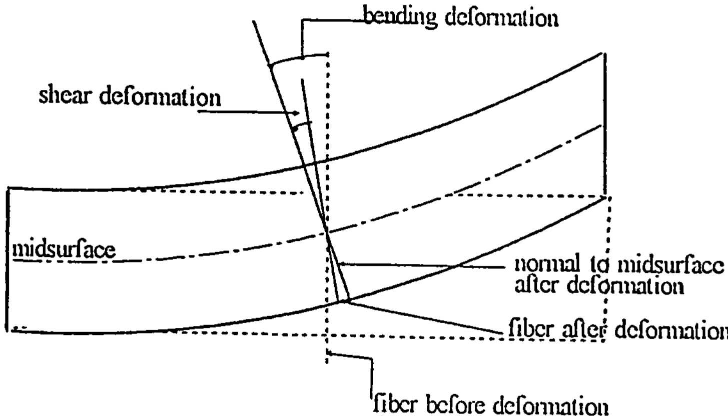

Figure 5.1: Degenerate shell concept: assumption regarding deformation.

5.3 Basic Elements

5.3.1 8-noded Serendipity

The 8-noded Serendipity element, Fig. 5.2a, is commonly used as a basis of the popular family of 'isoparametric' elements [105] which are deduced mainly by inspection and intuition, (see appendix B). When compared to other elements, Fig. 5.2b and c, the most conspicuous feature of the Serendipity element is the absence of an interior node which therefore minimizes the likelihood of mapping distortion for irregular meshes found in mitred bends. As discussed earlier in section 4.3.2, good results can be achieved when this element is used with reduced integration. However. for very thin shell situations results using reduced integration become increasingly stiff and therefore locked in a similar manner as if normal integration rule were used.

5.3.2 9-noded Lagrangian

In the the light of reduced or selective integration schemes, the performance of 9-noded Lagrangian element, Fig. 5.2b, is considered superior to that of 8-noded Serendipity element [94, 101]. However a major drawback not exhibited by the 8-noded Serendipity element when reduced integration is used, is that the 9-noded Lagrangian element may result in very erratic solutions caused by the appearance of spurious mechanisms. Consequently, additional consideration is taken as a safeguard by incorporating the use of the third type of the basic elements, the Heterosis element. It should be noted that the implementation of the 9-noded Lagrangian element used in this study is based purely on Lagrangian shape functions [107] where each of the functions satisfies the required interpolatory property at each of the nine nodes in terms of the five independent degrees of freedom (u, v, w, α, β).

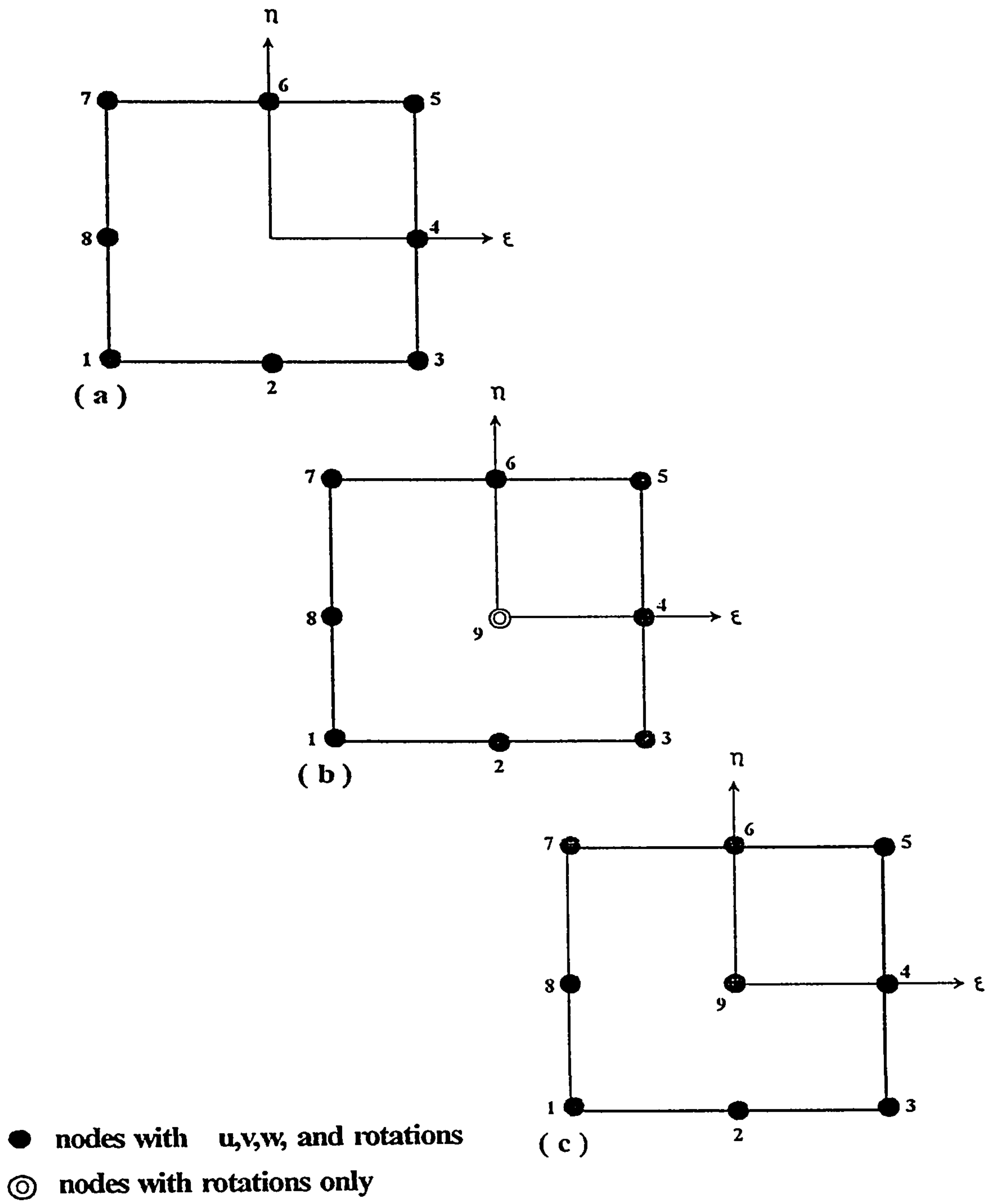

Figure 5.2: Basic-elements (a) 8-noded Serendipity (b) Heterosis (c) 9-noded Lagrangian

5.3.3 Heterosis Element

The Heterosis element under consideration is the quadratic 9-noded element with 42 degrees of freedom as shown in Fig. 5.2c. The eight side nodes have five degrees of freedom each; three translations (u, v, w) and two rotations $(\beta,\ \alpha)$. The ninth central node has only the two rotational degrees of freedom. Consequently, a hierarchical formulation of Ref. [72] is adopted in the Heterosis implementation. As such the shape functions of the eight boundary nodes belong to the serendipity shape functions, whereas the hierarchical shape function for the central ninth node is the bubble function.

Regarded as paragon of plate behavior [105]. the Heterosis element under reduced integration yields correct stiffness rank and achieves higher accuracy than the 9-noded Largrangian element. Moreover, the appearance of spurious mechanism is improbable, but mapping distortion introduced by irregular meshes may somewhat deteriorate the performance of the Heterosis element [105].

5.4 Generic Coordinate Systems

5.4.1 Generic Element Description

A typical quadratic degenerated shell having curved geometry as shown in Fig. 5.3a is considered as a representative element for the three basic elements employed in the present formulation. The element may have variable thickness and such variation is defined by specifying the position of the two opposite nodes on the top and bottom surfaces of the shell element. This will facilitate the use of local fiber (or nodal) coordinate system at each node to maintain displacement continuity when the element is used for mitre problems with geometric discontinuities at the mitre joint. For deriving the element equations, the mid-surface of the mitre shell is taken as a reference

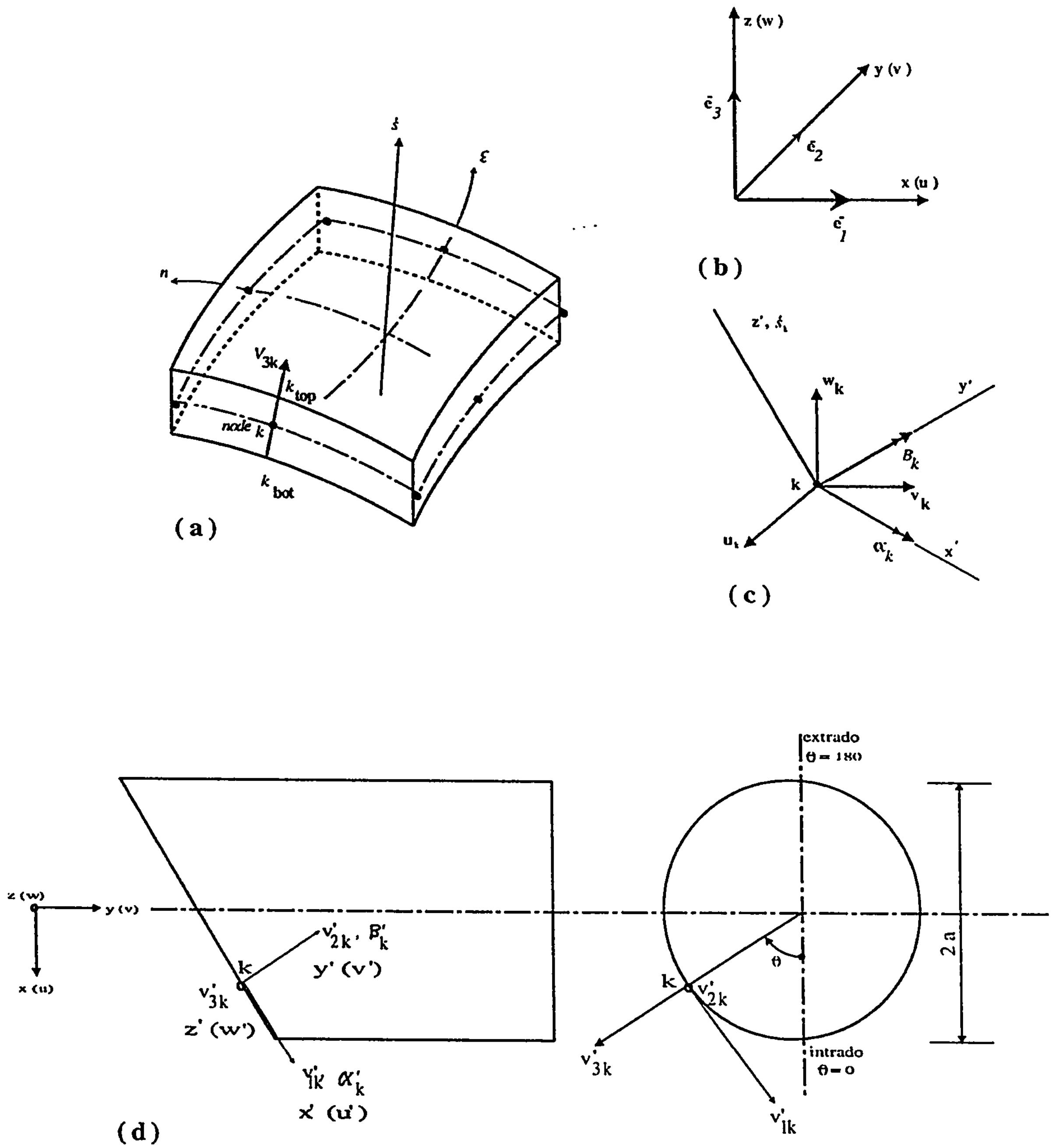

Figure 5.3: Element configuration and coordinate systems (a) element geometry (b) global-structure coordinate (c) local-fiber coordinate (d) mitre-edge coordinate

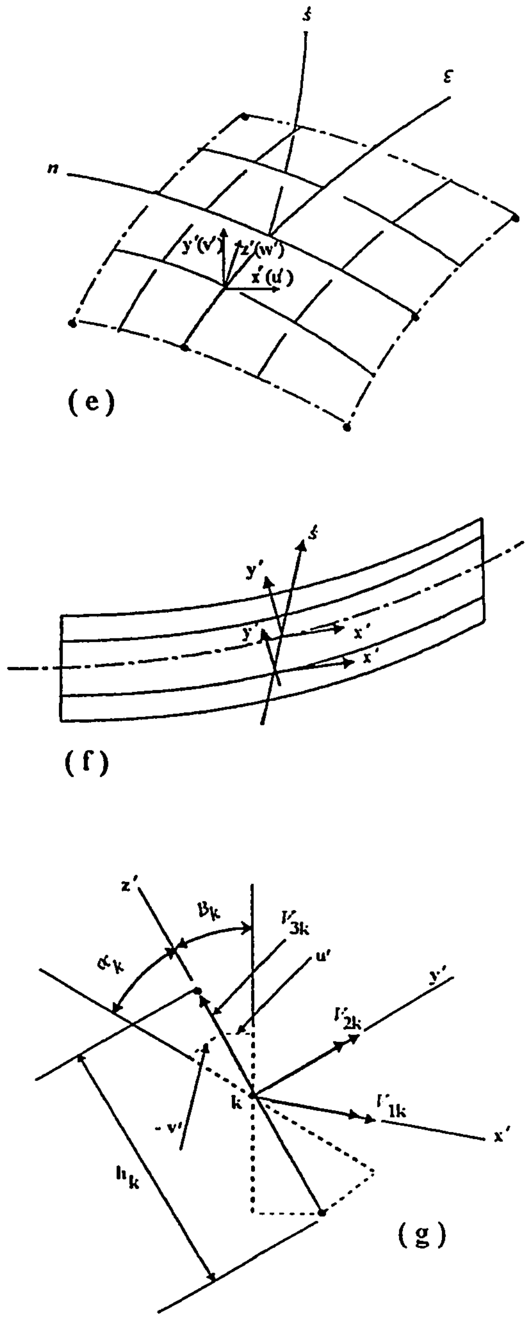

Figure 5.3: Element configuration and coordinate (continued) (e) curvilinear coordinate (f) local-lamina coordinate (g) nodal vectors.

datum.

For reasons of convenience five different coordinate systems, Figs. 5.3- 5.3, will be utilized for the present implementation. Some of these coordinate systems are partly discussed in Ref. [72].

5.4.2 Global Structure Coordinates–x_i

The global structure reference frame, Fig. 5.3b, is a rectangular cartesian (x,y,z) system with the corresponding base vectors designated by e_i (i = 1,2,3). It is freely chosen and used to defined the structure geometry and translational (u,v,w) degrees of freedom at each node. Nodal coordinates as well as the global stiffness matrix and applied force vector are referred to this system. The following notation, depicted in Fig. 5.3b, is used.

$$x_i(i=1,3) \quad and \quad x_1 = x,\ x_2 = y,\ x_3 = z$$

$$u_i(i=1,3) \quad and \quad u_1 = u,\ u_2 = v,\ u_3 = w$$

$\bar{e}_i(i=1,3)$ is a unit vector in the x_i direction.

5.4.3 Local Fiber Coordinates–v_{ik}

A local fiber coordinate system ($\underline{v}_{ik}$; $i = 1,3$) is constructed at each node (k), Fig. 5.3c. The associated orthogonal base vectors are $\bar{v}_{1k}$,$\bar{v}_{2k}$,$\bar{v}_{3k}$. The direction of $\underline{v}_{3k}$ is chosen to coincide with the fiber direction at a given node, k, as follows:

$$\underline{v}_{3k} = (\underline{x}_k^+ - \underline{x}_k^-)/h_k \tag{5.1}$$

$$h_k = \parallel \underline{x}^+ - \underline{x}_k^- \parallel \tag{5.2}$$

where $\underline{x}_k^+$ is the position vector of the kth node on the top surface of the shell; $\underline{x}_k^-$ is the position vector of the kth node on the bottom surface of the shell; h_k is the thickness of the shell at the kth node (see Fig. 5.3g) and $\parallel \bullet \parallel$

denotes the Euclidean norm (or length) of the embraced vector. There are several ways to define the direction of vectors $\bar{v}_{ik}, i = 1, 2$–see for example Refs. [94, 72, 108]. These vectors are orthogonal to the vector $\underline{v}_{3k}$ and parallel to the global xz-plane. Thus

$$\bar{v}_{1k} = (\bar{e}_2 \times \underline{v}_{3k}) / \parallel \bar{e}_2 \times \underline{v}_{3k} \parallel \tag{5.3}$$

$$\bar{v}_{2k} = \bar{v}_{3k} \times \bar{v}_{1k} \tag{5.4}$$

In the case that $\bar{v}_{3k}$ is parallel to $\bar{e}_2$ in Eq. 5.3, the latter is replaced by $\bar{e}_3$–that is $\bar{v}_{1k}$ is taken to be in the direction of minus $\bar{e}_1$. With reference to Fig. 5.3g, the unit vector $\bar{v}_{3k}$ defines the direction of the 'normal' at node k. which is not necessarily perpendicular to the mid-surface at k. The unit (tangential) vectors $\bar{v}_{1k}$ and $\bar{v}_{2k}$ define the rotations (α_k and β_k respectively) of the corresponding 'normal'.

The advantage of this definition for the vector $\bar{v}_{3k}$ not necessarily perpendicular to the shell mid-surface is that as a result there are no gaps or overlaps along element boundaries. Therefore this effectively ensures interelement compatibility. Furthermore. the definition adopted for $\bar{v}_{1k}$, Eq. 5.3, provides an easy identification of its direction. and hence that of α_k and β_k, in a general mitre or curved shell structures.

5.4.4 Mitre-Edge Coordinates—$v_{ik'}$

The mitre-edge coordinate system is a coordinate set used to locate a mitre nodal point k on the mitre joint as shown in Fig. 5.3d. Mitre nodal-point vectors are expressed in terms of unit vectors $\underline{v}_{ik'}$ (i=1,2,3) which respectively are tangent, normal, and binomal to the helicoidal mitre edge at k. It is convenient to use the helicoidal mitre edge associated angles γ, ψ and $\alpha\prime$ at node k wherein γ is the hoop angle compliment. ψ is the helix angle and $\alpha\prime$ the corresponding local mitre angle all referred to any given node k of the

helicoidal mitre edge or mitre edge plane.

The significance of this coordinate system is that when, often, the helicoidal mitre edge orbit forms a symmetric plane, the translational displacement quantities (u,v,w), typically referred to the earlier global structure coordinate x_i, would become easier to handle as displacement boundary conditions. Otherwise, the specification of the latter conditions in the global structure coordinate system would undoubtedly be prohibitive if not impossible. In this regard, the expediency offered by referring all mitre edge associated displacement boundary conditions to the mitre-edge coordinate-system $\underline{v}_{ik'}$ (i=1,2,3) is considered the most central core of the ongoing displacement finite element analysis of the single mitred bends.

In order to transform a system of translational displacements vector ($\underline{A}_s$) in the global structure coordinate to a corresponding system translational displacements vector ($\underline{A}_m$) in the mitre-edge coordinate, a rotation transformation matrix, $\underline{R}_{ms}$, similar in form to that for space transformation in space-truss or frame analysis [109] is generally required in the form:

$$\underline{A}_m = \underline{R}_{ms}\underline{A}_s \tag{5.5}$$

where $\underline{A}_m$ is a vector consisting of $(u, v, w)_k$ in the mitre-edge axes ($\underline{v}_{ik'}$) and $\underline{A}_s$ is a vector consisting of $(u, v, w)_k$ in the global structure axes ($\underline{x}_i$). The form of the rotation matrix $\underline{R}_{ms}$ depends upon the particular orientation of the mitre 'node' k defined explicitly in terms of the angle set $(\gamma, \psi, \alpha')_k$ as shown in Fig. 5.3d.

There are various way in which the orientation angles $(\gamma, \psi, \alpha')_k$ can be defined, but the one involving the hoop angle (θ) and the mitre angle (α) are suitabily obtainable in Refs. [16, 10, 15]. For a given mitre node (k), the more precise definition of these rotation angles takes the following relation:

$$\gamma_k = \pi/2 - \theta_k$$

$$\psi_k = \tan^{-1}(\tan \alpha_k \sin \theta_k) \tag{5.6}$$

$$\alpha_{k'} = \tan^{-1}(\tan \alpha_k \cos \theta_k \cos \psi_k)$$

It follows therefore that three successive rotations are necessary to permit explicit determination of the single transformation matrix ($\underline{R}_{ms}$) in the form:

$$\underline{R}_{ms} = \underline{R}_{\alpha'} \underline{R}_{\psi} \underline{R}_{\gamma} \tag{5.7}$$

where $\underline{R}_{\gamma}, \underline{R}_{\psi}$ and $\underline{R}_{\alpha'}$ are, rspectively, the three rotation matrices required to successively account for rotation angle γ, ψ and α' so that transformation from $\underline{x}_i - axes$ to $\underline{v}_{ik'} - axes$ is materialized. Writing these matrices in expanded form gives

$$\underline{R}_{\gamma} = \begin{bmatrix} \cos\gamma & 0 & -\sin\gamma \\ 0 & 1 & 0 \\ \sin\gamma & 0 & \cos\gamma \end{bmatrix} \tag{5.8}$$

$$\underline{R}_{\psi} = \begin{bmatrix} \cos\psi & \sin\psi & 0 \\ -\sin\psi & \cos\psi & 0 \\ 0 & 0 & 1 \end{bmatrix} \tag{5.9}$$

$$\underline{R}_{\alpha'} = \begin{bmatrix} 1 & 0 & 1 \\ 0 & \cos\alpha' & -\sin\alpha' \\ 0 & \sin\alpha' & \cos\alpha' \end{bmatrix} \tag{5.10}$$

Considering Eq. 5.5 it can be seen that the case of transforming translational displacement from mitre-edge coordinates to global structure coordinates, with $\underline{R}_{ms}$ being orthogonal, yields:

$$\underline{\Delta}_s = \underline{R}^T_{ms} \underline{\Delta}_m \tag{5.11}$$

It should be noted that the rotation transformation matrix $\underline{R}_{ms}$ is valid for all nodal points on the mitre-edge. In essence $\underline{R}_{ms}$ constitutes of rows which define the direction cosines of such a 'node' with respect to the global structure coordinate, hence the following expression:

$$\underline{R}_{ms} = [\underline{v}_{1'}, \underline{v}_{2'}, \underline{v}_{3'}]^T_k \tag{5.12}$$

5.4.5 Curvilinear Natural Coordinate–ξ, η, ζ

In this system, Fig. 5.3e, ξ, η are two curvilinear coordinates in the middle plane of the shell element and ζ is a linear coordinate in the thickness direction, Fig. 5.3a. It is assumed that ξ, η and ζ vary between -1 and +1 on the respective faces of the element. The relations between the curvilinear coordinates, Fig. 5.3e, (ξ, η, ζ) and the global structure coordinates, Fig. 5.3b, (x, y, z) are given by expressions 5.17, which will later define the element geometry in the isoparametric implementation.

5.4.6 Local Lamina Coordinates–$X_{i'}$

This is a (primed) cartesian reference system, Fig. 5.3f, defined at each integration point in an element such that two of its axes are tangent to the lamina (or middle) surface of the shell. The integration points are locations where strains and stresses are also calculated. The lamina coordinate is specified by three orthogonal base vectors $\underline{x}_{i'}$ *i=1,2,3* of which $\underline{x}_{3'}$ (z') is always perpendicular to the lamina (face ζ = constant), being obtained by the cross product of the ξ and η directions:

$$\underline{x}_{3'} = \left(\frac{\partial x_i}{\partial \xi}\right) \times \left(\frac{\partial x_i}{\partial \eta}\right) \tag{5.13}$$

To maintain consistency in relating the definition of principal material axes *p-axes* to the definition of the lamina system of axes *l-axes*, the direction of $x_{1'}$ (x') is defined in a similar manner to that of direction v_{ik} in the global structure coordinate system. The direction $x_{2'}$ (y') is then obtained by the cross product of the $x_{3'}$ and $x_{1'}$ directions:

$$\underline{x}_{2'} = \underline{x}_{3'} \times \underline{x}_{1'} \tag{5.14}$$

Further exposition of this definition can be found in Refs. [72, 110].

Since the lamina system of axes varies from integration point to integration point, an orthogonal relationship exists between the global structure coordinate system ($\underline{x}_s$) and the local lamina coordinate system ($\underline{x}_l$ according to:

$$\underline{x}_s = \underline{T}_{sl}\underline{x}_l \tag{5.15}$$

where $\underline{T}_{sl}$ is a transformation matrix consisting of direction cosine between the global structure coordinate and the local lamina coordinate systems. The quantities $\underline{x}_s$ and $\underline{x}_l$ respectively denote the position vectors of a generic point of the mitre shell with respect to the global structure and local lamina coordinate systems. The definition of $\underline{T}_{sl}$ is thus given by:

$$\underline{T}_{sl} = [\underline{\bar{x}}\prime, \underline{\bar{y}}\prime, \underline{\bar{z}}\prime]^T \tag{5.16}$$

where $\underline{\bar{x}}\prime, \underline{\bar{y}}\prime, \underline{\bar{z}}\prime$ are unit vectors in the direction of the $x\prime, y\prime$ and $z\prime$ axes respectively.

5.5 Generic Element Equations

5.5.1 Geometric Equations

Following the isoparametric based finite element formulation, the initial geometry of a generic element (see Fig. 5.3a) can be described in terms of a set of the curvilinear natural coordinate axes ξ, η, ζ by applying the element shape functions to the nodal coordinates as follows:

$$X_i(\xi, \eta, \zeta) = \sum_{k=1}^{N} f_k x_{ik}^0 + \sum_{k=1}^{N} f_k \zeta \frac{h_k}{2} \bar{v}_{3k}^i \tag{5.17}$$

where

- i=1,2,3 refers to the three global structure directions *(x,y,z)*;
- N–is the number of nodes per element;

- $f_k = f_k(\xi, \eta)$ $(k = 1, N)$ are the element shape functions corresponding to the surface ζ = constant;

- h_k–is the shell 'thickness' at node k, i.e. the respective 'normal' length;

- ξ, η, ζ–are the curvilinear natural coordinates of the point under consideration; and

- x^0_{ik}–are the nodal coordinates corresponding to the surface $\zeta = 0$, the middle-surface.

More explicitly, expression 5.17 can be written as

$$\begin{bmatrix} X \\ Y \\ Z \end{bmatrix} = \sum_{k=1}^{N} f_k \begin{bmatrix} x^0_k \\ y^0_k \\ z^0_k \end{bmatrix} + \sum_{k=1}^{N} f_k \zeta \frac{h_k}{2} \begin{bmatrix} \bar{v}^x_{3k} \\ \bar{v}^y_{3k} \\ \bar{v}^z_{3k} \end{bmatrix} \qquad (5.18)$$

Specific representation of the interpolation shape functions f_k appearing in this equation can be found in Ref.[107]. The ones relevant to the three basic elements under consideration are given in appendix B.

5.5.2 Kinematic Equations

Generic displacements (u_i ; $u_1 = u$, $u_2 = v$, $u_3 = w$) at any point k on the shell (mid-surface) are taken to be in the directions of the global structure axes, Fig. 5.3a, whereas the two small rotations α_k and β_k are defined about the two tangential fiber axes defined earlier by $\underline{v}_{ik}$ and $\underline{v}_{2k}$, and indicated in Fig. 5.3g. Hence for a typical node k, the nodal displacement vector q_k would consist of:

$$\underline{q}_k = [u_k \; v_k \; w_k \; \beta_k \; \alpha_k]^T \qquad (k = 1, N) \qquad (5.19)$$

To derive the element kinematic (displacement) equations, the usual assumptions involving degenerate shell concept (section 5.2) are employed. Thus,

the generic displacement vector $u_i = (u, v, w)$ at a generic point of the mitre-shell element is given in terms of the components of the nodal displacement vector $q_k = [u_k\ v_k\ w_k\ \beta_k\ \alpha_k]^T$ as follows:

$$u_i = \sum_{k=1}^{N} f_k u_{ik} + \sum_{k=1}^{N} f_k \zeta \frac{h_k}{2} \mu_{ik} \underline{\Phi}_k \tag{5.20}$$

In this formula, the symbol $\underline{\mu}_{ik}$ and $\underline{\Phi}_k$ denote the following submatrices:

$$\mu_{ik} = \begin{bmatrix} v_{1k}^x & -v_{2k}^x \\ v_{1k}^y & -v_{2k}^y \\ v_{1k}^z & -v_{2k}^z \end{bmatrix} \tag{5.21}$$

$$\underline{\Phi}_k = [\beta_k\ \alpha_k]^T$$

Column 1 in the array $\underline{\mu}_{ik}$ contains positive values of the direction cosines of the first tangential vector $\underline{v}_{2k}$, and column 2 has the negative direction cosines for the second tangential vector (see Fig. 5.3g) being all referred to the local fibre coordinate set ($\underline{v}_{ik}$). More explicitly, Eq. 5.20 can be written as:

$$u_i = \begin{bmatrix} u \\ v \\ w \end{bmatrix} = \sum_{k=1}^{N} f_k \begin{bmatrix} u_k \\ v_k \\ w_k \end{bmatrix} + \sum_{k=1}^{N} f_k \zeta \frac{h_k}{2} \begin{bmatrix} v_{1k}^x & -v_{2k}^x \\ v_{1k}^y & -v_{2k}^y \\ v_{1k}^z & -v_{2k}^z \end{bmatrix} \begin{bmatrix} \beta_k \\ \\ \alpha_k \end{bmatrix} \tag{5.22}$$

Referring to Fig. 5.3g, the second summation in the above equations is as a result of local generic translations $u\prime$ and $-v\prime$ (in the directions of v_{1k} and v_{2k}) which arise due to the nodal rotations β_i and α_i respectively. The form of this local translations can be given as:

$$\begin{aligned} u\prime &= \zeta \frac{h_k}{2} \beta_k \\ v\prime &= \zeta \frac{h_k}{2} \alpha_k \end{aligned} \tag{5.23}$$

Contribution of these terms to the (global) generic displacements at any point *(k)*, constitutes the second summation in Eq. 5.22. In symbolic form,

Eq. 5.22 can be represented by

$$\underline{u}_k = \underline{f}_k \underline{q}_k \tag{5.24}$$

which succinctly represents the contribution to the global generic displacements from a given typical node *(k)* of the mitre shell element. The array $\underline{f}_k$, in Eq. 5.24, represents a matrix of modified shape functions and q_k is the nodal displacement vector given by Eq. 5.19. By combining the terms in Eq. 5.22, the form of matrix $\underline{f}_k$ is:

$$\underline{f}_k = \begin{bmatrix} f_k & 0 & 0 & \delta_k v^x_{1k} & -\delta_k v^x_{2k} \\ 0 & f_k & 0 & \delta_k v^y_{1k} & -\delta_k v^y_{2k} \\ 0 & 0 & f_k & \delta_k v^z_{1k} & -\delta_k v^z_{2k} \end{bmatrix} \tag{5.25}$$

in which δ_k represents the term $f_k \zeta h_k/2$. For the complete set of element nodes (*k=1,N*), the symbolic representation of Eq. 5.24, becomes

$$\underline{u} = \underline{f}\ \underline{q} \tag{5.26}$$

where

$$\underline{f} = [\underline{f}_1, \ldots, \underline{f}_k, \ldots, \underline{f}_N]$$

is the combined matrix of the degenerate element, and

$$\underline{q} = [\underline{q}_1^T, \ldots, \underline{q}_k^T, \ldots, \underline{q}_N^T]$$

is the vector of the element nodal displacement variables.

For specifying displacement boundary conditions occurring at the helicoidal mitre edge, the following considerations have to be taken into account during the formulation of the kinematic relations. The first consideration involves the components of the nodal displacement vector $\underline{q}_k = (u_k, v_k, w_k, \beta_k \alpha_k)$ being referred to the global structure coordinate axes must now be referred to mitre-edge coordinate axes as $\underline{q}_k\prime = (u_k\prime, v_k\prime, w_k\prime, \beta_k\prime, \alpha_k\prime)$.

Therefore by taking recourse to Eq. 5.20, the generic displacement vector in terms of the components of the new vector $\underline{q}_k\prime$ must take the form:

$$u_i = \sum_{k=1}^{N} f_k R_{ms}^T u_{ik}\prime + \sum_{k=1}^{N} f_k \zeta \frac{h_k}{2} \mu_{ik}\prime \underline{\Phi_k}\prime \tag{5.27}$$

or in symbolic form

$$\underline{u}_k = \underline{f}_k\prime \underline{q}_k\prime \tag{5.28}$$

where

$$R_{ms}^T = [\underline{v}_1\prime, \underline{v}_2\prime, \underline{v}_3\prime]_k \quad \text{see Eq. 5.12}$$

$$u_{ik}\prime = [\underline{u}_k\prime, \underline{v}_k\prime, \underline{w}_k\prime]$$

and

$$\mu_{ik}\prime = \begin{bmatrix} v_{1k}\prime^x & -v_{2k}\prime^x \\ v_{1k}\prime^y & -v_{2k}\prime^y \\ v_{1k}\prime^z & -v_{2k}\prime^z \end{bmatrix} \tag{5.29}$$

Following similar development to that of Eq. 5.25. the new form of $\underline{f}_k\prime$ in Eq. 5.28 is:

$$\underline{f}_k\prime = \begin{bmatrix} f_k v_{1k}\prime^x & f_k v_{2k}\prime^x & f_k v_{3k}\prime^x & \delta_k v_{1k}\prime^x & -\delta_k v_{2k}\prime^x \\ f_k v_{1k}\prime^y & f_k v_{2k}\prime^y & f_k v_{3k}\prime^y & \delta_k v_{1k}\prime^y & -\delta_k v_{2k}\prime^y \\ f_k v_{1k}\prime^z & f_k v_{2k}\prime^z & f_k v_{3k}\prime^z & \delta_k v_{1k}\prime^z & -\delta_k v_{2k}\prime^z \end{bmatrix} \tag{5.30}$$

In essence, Eq. 5.30 is deemed to supplant Eq. 5.25 whenever contribution to generic displacement vector $\underline{u}_k$ is to be accrued from mitre associated nodes which are specified as having displacement boundary condition(s). In this regard all specifications relating to the mitre nodes boundary conditions (viz: translational and/or rotational displacement boundary conditions and their respective joint loads) are locally referred to become 'parallel' to actual helicoidal mitre edge configuration. By taking this consideration at the kinematic level, a consistent formulation of the structure stiffness matrix is

ensured, although the nodal quantities related to the vector $\underline{q}_k$ are locally defined (with respect to the new local base vectors $\underline{v}_{1k}\prime, \underline{v}_{2k}\prime, \underline{v}_{3k}\prime$– constituting the mitre edge coordinate systems) while the remaining quantities relating to the vector $\underline{q}_k$ are still globally referred.

An alternative to such consideration could have been taken at the actual stiffness computational level, instead of the above **B-matrix** level. However the former would entail increased computational cost since the nonlinear analysis often requires several stiffness recalculations while the **B-matrix** is needed to be calculated only once. Hence the obvious choice of this consideration at the kinematic equations (**B-matrix**) level.

5.5.3 Strains, Stresses and Stifness Matrices

5.5.3.1 Strains

The local lamina coordinate system (Fig. 5.3f) is to be adopted in defining strain components. In this system of coordinates, it is relatively easy to impose the degenerate shell assumption of zero normal lamina-stress ($\sigma_{z\prime}$) and it is also a natural system to define the constitutive relations, especially for extension to anisotropic materials. Furthermore, the local lamina system of coordinates is the most convenient for expressing the stress components (and their resultants) for mitre shell analysis and design.

Referring to the local lamina coordinates ($x\prime, y\prime, z\prime$), the five significant strain components at a given generic point of the mitre shell are:

$$\underline{\epsilon} = \begin{bmatrix} \epsilon_{x\prime} \\ \epsilon_{y\prime} \\ \gamma_{x\prime y\prime} \\ \gamma_{x\prime z\prime} \\ \gamma_{y\prime z\prime} \end{bmatrix} = \begin{bmatrix} \frac{\partial u\prime}{\partial x\prime} \\ \frac{\partial v\prime}{\partial y\prime} \\ \frac{\partial u\prime}{\partial y\prime} + \frac{\partial v\prime}{\partial x\prime} \\ \frac{\partial u\prime}{\partial z\prime} + \frac{\partial w\prime}{\partial x\prime} \\ \frac{\partial v\prime}{\partial z\prime} + \frac{\partial w\prime}{\partial y\prime} \end{bmatrix} \tag{5.31}$$

where $u\prime, v\prime$ and $w\prime$ are the displacement components in the local lamina coordinate system ($x_{i}\prime$). Equation 5.31 contains certain derivatives of the local generic displacements with respect to the local lamina coordinates. These local derivatives are obtained from the global derivatives of the (global) generic displacements u,v, and w [72].

The strain matrix $\underline{B}$, relating the strain components (in the local lamina system) to the element nodal variables $\underline{q}$ (in the global structure system), can be constructed as

$$\underline{\epsilon} = \underline{Bq} \tag{5.32}$$

where $\underline{\epsilon}$ and $\underline{q}$ are defined in Eqs. 5.31 and 5.26 respectively, and $\underline{B}$ is a matrix with five rows and a number of columns equal to the number of nodal variables.

5.5.3.2 Stresses

Neglecting the stress in the direction perpendicular to the mitre shell midsurface ($\sigma_{z}\prime = 0$), in accordance with the degenerated shell assumption, the five stress components in the local lamina system are:

$$\underline{\sigma} = \begin{bmatrix} \sigma_{x\prime} \\ \sigma_{y\prime} \\ \tau_{x\prime y\prime} \\ \tau_{x\prime z\prime} \\ \tau_{y\prime z\prime} \end{bmatrix} = \underline{D\epsilon} \tag{5.33}$$

where $\underline{\epsilon}$ is defined in Eq. 5.31. The elasticity matrix $\underline{D}$ is a 5x5 matrix, whose derivation and specific form were considered in chapter 3.

5.5.3.3 Stiffness Matrix

The element stiffness matrix $\underline{k}^e$ is derived in the usual way from the principle of virtual work and can be written as:

$$\underline{k}^e = \int_{-1}^{+1}\int_{-1}^{+1}\int_{-1}^{+1} \underline{B}^T \underline{DB} \mid \underline{J} \mid d\xi d\eta d\zeta \tag{5.34}$$

In this expression, matrices $\underline{B}$ and $\underline{J}$ are functions of ξ, η and ζ.

Integration of Eq. 5.34 through the thickness direction may be computationally expensive but is more appropriate for mitre shells in which proper account has to be taken of point to point variation of the local lamina system of axes as well as the through the thickness variation of the Jacobian matrix ($\underline{J}$). For a nonlinear stiffness to be formed. the elasticity matrix $\underline{D}$ in Eq. 5.34 must be replaced by the elasto-plastic or tangent-elasticity matrix ($\underline{D}_T$) derived earlier as shown in Eq. 3.23.

For the purpose of calculating the generic element internal force vector $\underline{f}^e$, the following classical expression is used

$$\underline{f}^e = \int_{-1}^{+1}\int_{-1}^{+1}\int_{-1}^{+1} \underline{B}^T \underline{\sigma} \mid \underline{J} \mid d\xi d\eta d\zeta \tag{5.35}$$

in which $\underline{\sigma}$ is defined in Eq. 5.33. It should be noted that all integration is done numerically and as such all integrals must be replaced by summation of the integrands over a selected quadrature rule–the Legendre-Gauss quadrature rule being the one adopted in this work.

5.6 Large Deformation

For the inclusion of large deformation, or geometrical nonlinearity, a total Lagrangian formulation is adopted [72]. The formulation accounts for large translations and moderate rotations for which the Piola-Kirchhof stress and Green-Lagrange strain fields are used to respectively define the current state of stress and strain.

The displacement field gives the current (deformed) configuration in relation to an initial position. During the nonlinear process, the usual infinitesimal strain-displacement matrix, $\underline{B}_O$, is calculated only once and its nonlinear part, $\underline{B}_L$, is used to get an update of the current B-matrix:

$$\underline{B} = \underline{B}_O + \underline{B}_L \tag{5.36}$$

Similar update of the stiffness matrix results in

$$\underline{K} = \underline{K}_O + \underline{K}_L \tag{5.37}$$

where $\underline{K}_O$ is the usual infinitesimal stiffness part and $\underline{K}_L$ is the geometric stiffness defined as

$$\underline{K}_L = \int_V d\underline{B}_L^T \underline{\sigma} dV \tag{5.38}$$

In order to determine $\underline{K}_L$, explicit evaluation of $\underline{B}_L$ must be made. For the degenerate shell elements employed in this work, the specific and appropriate terms involved can be found in [72].

5.7 Numerical Integration

5.7.1 In-plane Integration

For exact integration (mxm gauss points) of the expression in Eq. 5.34, the highest grade polynomial (m) in the expression must be considered. However by integrating the expression numerically in the plane of the mitre shell (surface ζ = constant), the shear and membrane stiffness terms become overestimated, i.e. locking phenomena was manifested. In such a case the beneficial effects of a reduced integration technique (m-1 x m-1 gauss points) on the isoparametric shell element have been established in a number of investigations [72, 83]. Another way to enhance numerical stability of the numerical technique is by using selective integration wherein the reduced (m-1 x m-1)

integration is used in evaluating all transverse shear stiffness terms and the exact (m x m) integration is used for the calculation of the remaining stiffness terms.

5.7.2 Across-Thickness Integration

In its simplest form, integration across the thickness of the mitre shell can be implemented using layered model wherein stress dependent quantities such as in Eq. 5.34 are evaluated by the mid-point rule (separate layers). However central to the present study is the development and use of an extended layered approach in addition to the simple-layered model.

5.7.2.1 Simple-Layered Models

In its own right, the layered approach [77, 72] facilitates integration through the element thickness. Nonetheless, its major significance lies in its ability to accommodate across the thickness variation in anisotropic material properties as well as in allowing to monitor the spread of plastification across an element thickness.

To employ a layered model a shell element must simply be subdivided into a series of layers, Fig. 5.4. Each of the resulting layers is then considered to contain one mid-layer integration point which duly serves as as stress sampling point, Fig. 5.4a. In this way, the actual stress distribution of the shell is simply modelled by a piece-wise constant approximation Fig. 5.4b.

In the present implementation, layers are to be numbered sequentially, starting at the bottom surface of the mitre shell element. Different layer thickness can be employed but the number of layers in each element must be the same. The specification of the layer thickness is done with respect to the third component of the curvilinear natural coordinate axes, ζ.This permits a

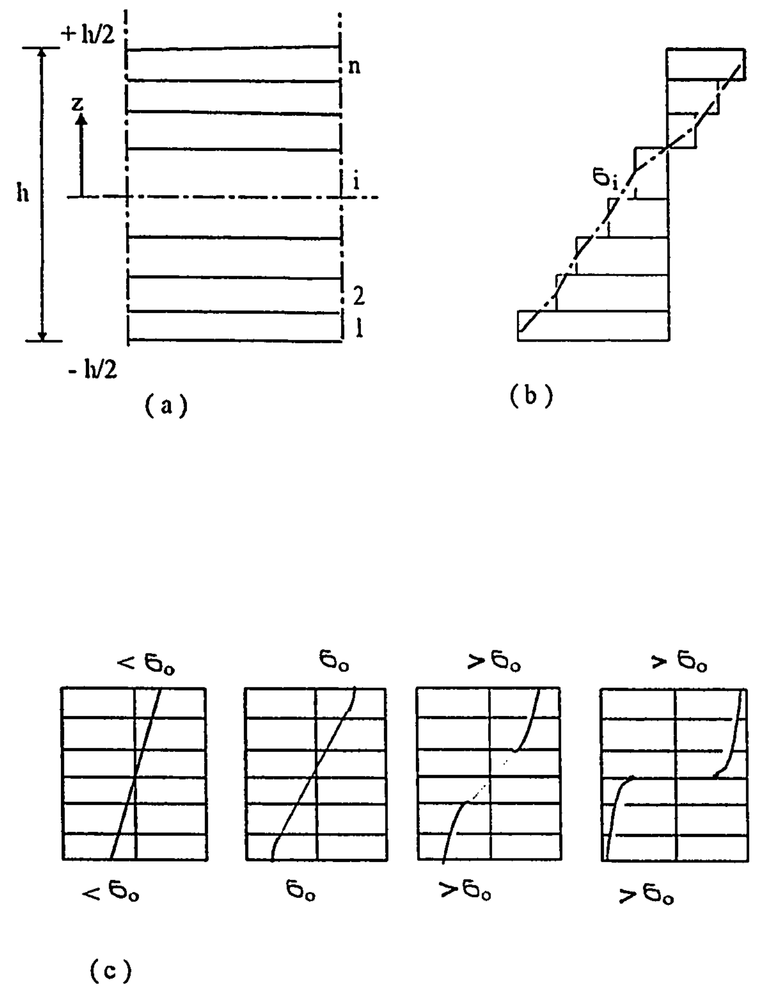

Figure 5.4: Layered element model (a) across-thickness discretization (b) layer stress representation (c) layer plastification.

convenient way in specifying the variation of the layer thickness as a function of the normalized fractional value of the absolute shell thickness.

It is understood that the foregoing assertions could not be detrimental if only elastic mitre analysis were to be considered. To improve on its inherent beneficial offerings, the simple layered model must therefore be propped up in some way so that it can reasonably extend to account for inelastic analysis too.

5.7.2.2 Extended-Layered Models

The possibility of extending the use of layered model for accurate inelastic analysis is sought using higher order quadrature rule that is greater than the default mid-point rule, used in the simple layered model. Calling it extended layered model, the increased order layered model is considered most appropriate since the computational overhead it entails will pale to insignificant when due account is taken of proper variation of across the thickness properties including elastic-plastic stiffnesses. The desirability of a relatively higher order rule is also suggested by the need for faster and uniform convergence of the inelastic stresses which often assume complicated distributions with sharp slope discontinuities at the elastic-plastic interfaces. Fig. 5.4c.

In using this so-called extended-layered model four folds benefits are apparently accrued. First, it is seen that since stiffness terms are calculated by integrating a quasi-parabolic function of the ζ (miter shell thickness) direction, two gauss points in each layer are effectively enough for linearly elastic anisotropic single mitred bend problems. For isotropic situation of a similar problem, it follows therefore that only a single layer is required to obtain the desired mitre analysis. The above remark is particularly important because a large number of the mitre analysis runs to be used for the validation of this

study are elastic runs. Moreover, many of the inelastic runs would require preliminary elastic modelling or trouble shooting. As such the advantage of using as fewer number of layers as permissible is obvious. Secondly, the use of the relatively higher order rule permits accurate modelling of the complicated helicoidal mitre edge geometry even at the face of a large mitre angle (α). The absence of this latter capability in many of the reviewed literatures is therefore a major motivation for this improvement. For the third point, it is obvious that fewer number of layers are required when the extended layered approach is used and this is quite an advantage due to its reduced requirements on data input and preparations. Consequently the likelyhood of input data modelling error akin to numerical models is also reduced. Fourth. greater numerical accuracy is ensured in addition to savings in time required to bring the complicated elasto-plastic stress distribution into normalized global equilibrium of the general elasto-plastic solution algorithm, as highlighted later in sections 6.1.1and 6.1.5.

5.7.3 Stress Resultants

A sign convention nomenclature assigned for the stress resultants is illustrated in Fig. 5.5. The stress resultants are obtained by numerical integration of the corresponding stress components with respect to the thickness coordinate ζ:

$$N_x = \int_{-\frac{h}{2}}^{\frac{h}{2}} \sigma_x dz = \frac{h}{2} \sum_{i=1}^{n} \sigma_x^i \Delta\zeta^i \tag{5.39}$$

$$M_x = -\int_{-\frac{h}{2}}^{\frac{h}{2}} \sigma_x dz = -\frac{h^2}{4} \sum_{i=1}^{n} \sigma_x^i \zeta^i \Delta\zeta^i \tag{5.40}$$

$$Q_x = \int_{-\frac{h}{2}}^{\frac{h}{2}} \tau_{xz} dz = \frac{h}{2} \sum_{i=1}^{n} \tau_{xz}^i \Delta\zeta^i \tag{5.41}$$

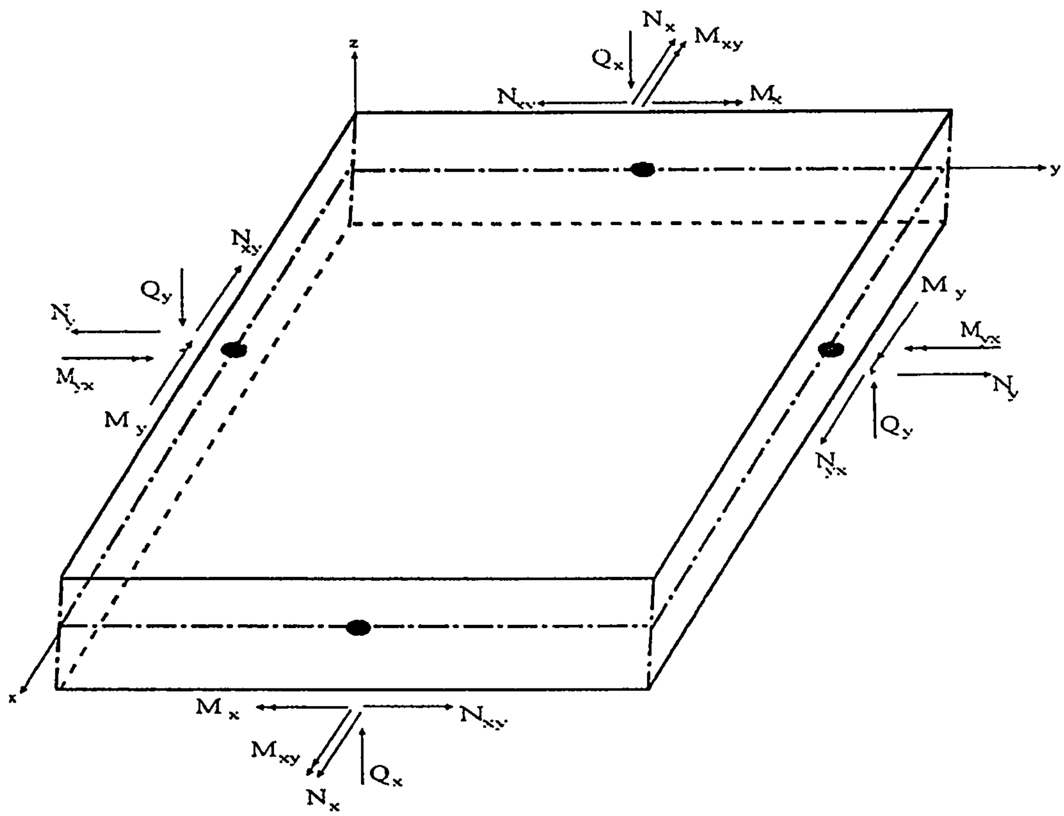

Figure 5.5: Stress resultant nomenclature.

where $i=1,n$ and n is the number of layers. Similar expressions can be described for N_y, M_y, M_{xy}, and Q_y resultants.

5.8 Domain Discretization

5.8.1 General Considerations

In view of the complex mitre geometry, a particular interest is in place for this study to consider a meshing strategy that will offer the ability to adjust a desired mitre mesh according to the perceived behavior of a given loaded single mitred bend. Thus in addition to proper choice of the three basic elements together with their transition counterparts, a further improvement in the solution quality of the mitre will be required to be sought in an optimal manner [111, 112, 113].

The review of the literature has served to indicate the mesh-critical nature of mitred-shell problems. This criticality depends not only on the complex mitre edge geometry but also on the type of loading. In the vicinity of the plane of the mitre edge where stress values and decay rate are generally higher, a greater degree of freedom *DOF* density–the number of DOF per unit area of the mitre domain–is necessary. From literature point of view, such arguments are in line with the work of Burnett [107] who amply explained the relationship between a desired solution quality and the DOF density. Similar treatment including the criteria for goodness of a mesh and a step-by-step procedure of mesh selection. improvement and refinement have been found useful from Refs. [114, 115]and [116].

5.8.2 Meshing Strategies

In order to take proper account of the oblique nature of the mitre edge geometry, the determination of a discretization strategy that is capable of

satisfactorily representing the stress raising effects of the mitre edge is important. A uniform mesh consisting of elements all about the same size and shape and repeated in fairly regular pattern is the easiest type to construct. However such a mesh will provide more-or-less uniform DOF density and hence it is generally most appropriate in the large but remote areas of the mitre edge where mitre stress distributions tend to be least complicated. In the portion of the mitre edge where the mitre solution is most complicated, a greater DOF density is necessary in order to maintain a fair level of accuracy. As such the mesh must be locally refined.

Various techniques exist for changing the DOF density. The ones shown in Fig. 5.6 reflect four basic but feasible schemes. Nonetheless, for reasons of compatibility with the adopted three basic elements, two favored mesh possibilities, as shown in Fig. 5.7, were isolated from which a more suitable scheme was explored. The first meshing scheme (Fig. 5.7a) uses transition-element having incomplete quartic as its highest graded polynomial version of the basic elements whereas the second uses linear-constraints.

Although simplifying mesh design and reducing the number of nodes or mesh density required in a particular mitre mesh, the use of linear-constraints, also known as 'pinched-nodes', entails a loss of symmetry in the matrix equation. Thus, because the present study employs a *FRONT*al solver, the loss of matrix symmetry due to pinched nodes may offset the gain in computational efficiency due to fewer nodes or DOF. Consequently, the idea of possible use of the linear constraint equations or pinched nodes scheme was discarded.

The implementation of the transition follow similar development and implemention of their basic elements. However, the distinction between the assigned names: *transition* Serendipity, Lagrangian and Heterosis elements

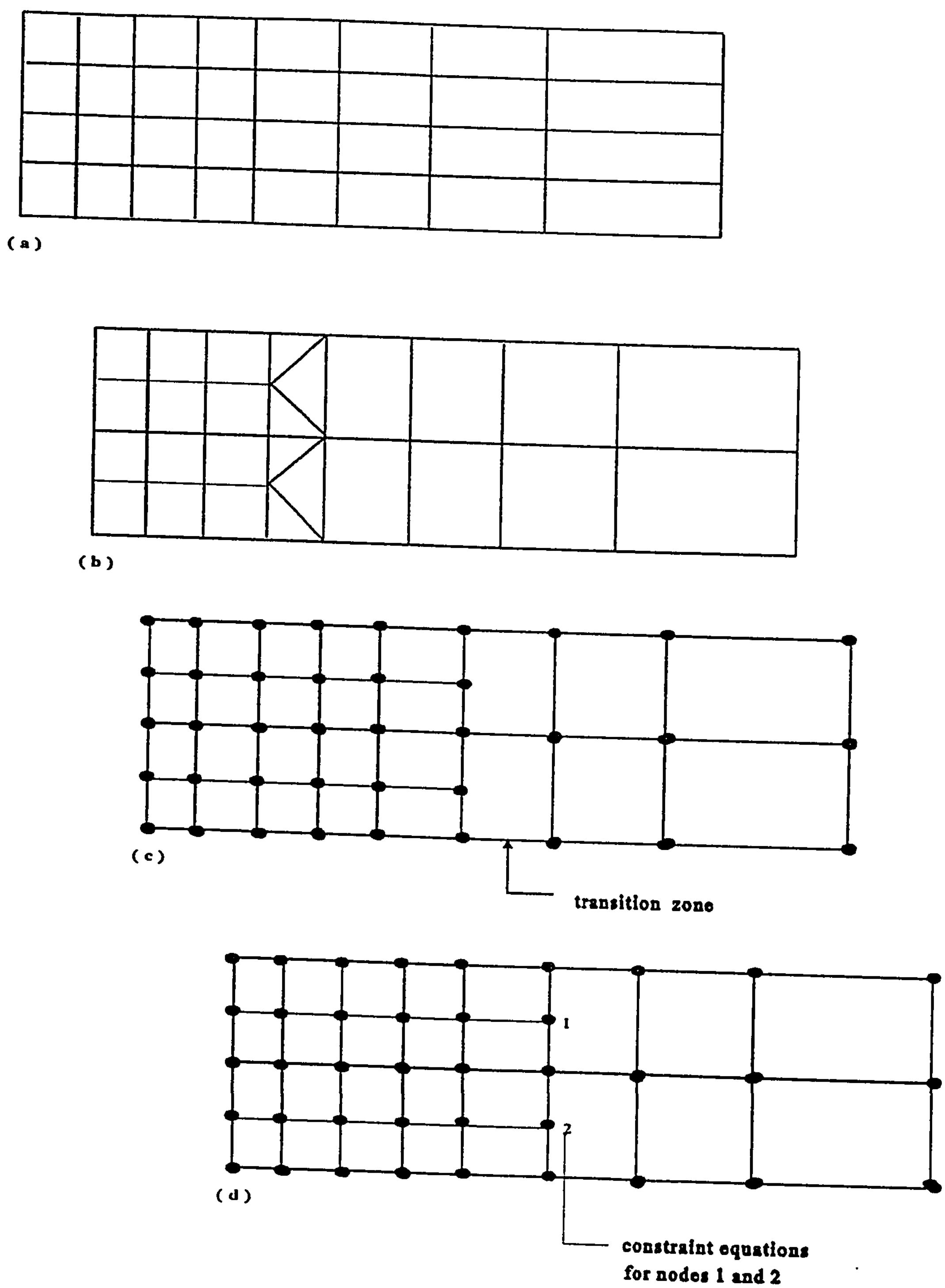

Figure 5.6: Representation for DOF density change (a) basic-elements (b) triangular-elements (c) transition-elements (d) 'pinched-nodes' (linear constraints).

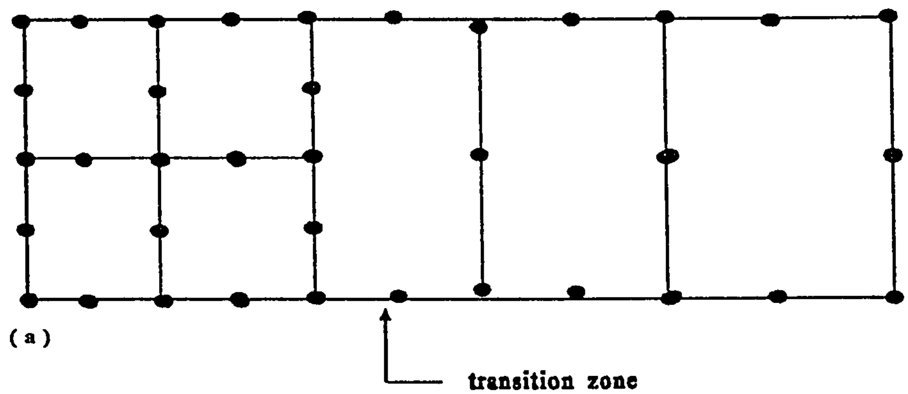

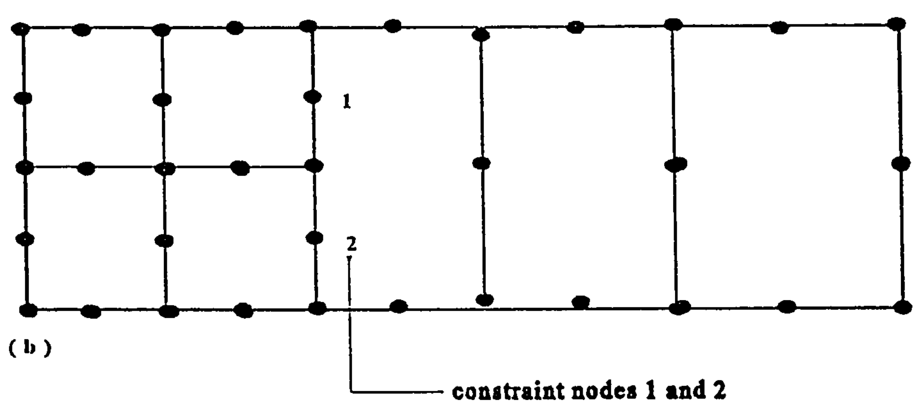

Figure 5.7: Mesh refinement possibilities (a) transition-mesh (b) linear constraint-mesh.

and the corresponding *basic* Serendipity, Lagrangian and Heterosis elements is an important one. This fact become appropriately translated in the computer implementation phase in which a library of these six distinct elements is provided. Further exposition on this is relegated to appendix B.

5.8.3 Transition-Elements

As already discussed, the prime motive in the development and implementation of the three transition elements is to provide flexibility in changing the DOF density in addition to that which could, by default, be provided by their basic counterparts. Owing to compatibility considerations, the isoparametric implementation of the transition elements was maintained to be similar in form to that of the basic elements. The only major point of departure lies with the fact that each of the transition elements is in excess of two nodes on one of its sides. Nonetheless, it is this side (having the two additional nodes) which effectively permitted the DOF density change—by its use in connecting as many as two adjacent rows/columns of the basic elements on one its side to as many single rows/columns of the basic elements on a side opposite to that side.

From the trial solution [107] point of view, the transition elements are incomplete quartic elements having the side with 'excess' nodes as completely quartic in ξ or η and the remaining sides completely quadratic in both ξ and η. Being complete isoparametric quadratic elements, the basic elements have all their four sides quadratic in both ξ and η. Hence in allowing some degree of 'compatibility' the three quadratic sides of transition elements are assigned the same shape functions as those in use for the corresponding three sides of the basic elements. The remaining quartic side suggested the use of a Lagrange type basis function that collocates through all the five

quartic nodes, lying on the quartic side. Implementation of this is therefore straight forward once the necessary but obvious adjustments are made in the constructed quartic basis functions–in such a way that all interpolatory properties between the quartic and the other quadratic nodal bases (shape functions) are duly satisfied as each of the individual transition elements might deemed. Details of the various forms of the shape functions utilized, including the specific form of the restricted quartic non-conforming Lagrange type bases, are referred to appendix B.

Following the construction and implementation of the transition shape functions, a point of further concern involves the ability of the quartic side in ensuring a smooth transition as well as stable change in size of the basic elements on either side of the transition level or 'front'. Because of the restricted non-conforming quartic nature of the Lagrangian functions involved, the need to use a higher quadrature rule to ensure numerical integration of the transition element at the same level of accuracy as the basic element counterpart is immediately apparent. In this regard various numerical integration rules have been systematically experimented. This experimentation was found most crucial during the inelastic phase of the analysis, mainly tested using loaded plates and/or cylindrical shells. As a general rule therefore, an integration rule that is one-point higher than the one to be specified for the basic elements is considered adequate in integrating stiffness and load integrands whenever a transition element is encountered in the computer solution algorithm.

Chapter 6

IMPLEMENTATION TO COMPUTER CODE PLAMBS7

6.1 Implementation Preliminaries

6.1.1 Incremental Solution Techniques

Finite element solutions of plasticity problems in general are dependent upon load path discretization and this poses a number of problems concerning error control in practice [117, 118]. For instance all that some problems may require is the load level at which first limit point manifested. Without using an appropriate solution technique that allows the limit point to be passed, even this information may not be available or reliable. However contemporary available solution procedures generally permit 'limit' or collapse load prediction based on equilibrium iterations. These iterations are mainly dictated by the provision of very small load increments close to the 'limit' point.

6.1.2 The Equations of Equilibrium

In elasto-plastic space, the equations of equilibrium can be linearized in several ways [72, 119]. A common approach is the load path dependent technique wherein the total applied load is subdivided into a number of incremental

segments. By identifying the status of the solution procedure at a given load increment step(r), the basic unknown in that step is the array of nodal displacements increment, $\Delta \underline{U}_i^r$. The subscript i denotes an iteration number within the increment. If the vector $\Delta \underline{f}^r$ represents an incremental segment of the discretized load path then the incremental equilibrium equation to be solved would take the form:

$$\underline{K}_{i-1}^r \Delta \underline{U}_i^r = \Delta \underline{f}^r \tag{6.1}$$

where $\underline{K}_{i-1}^r$ is the stiffness matrix at the beginning of the i_{th} iteration.

6.1.3 Stiffness Algorithms

The use of different algorithms consisting of an initial stiffness, a tangential stiffness, and two options of the combined tangential and initial stiffness have been reported in the literatures [78, 120]. However the account of what prevails in the present subsections follow that of Refs. [77, 72].

6.1.3.1 Tangential Stiffness

The tangential stiffness technique involves adjusting the stress-strain relations and accounting for plastic deformation in all iterations i of every load increment r in order to evaluate an upto date global stiffness matrix $\underline{K}_i^r$ in Eq. 6.1. A limited number of iterations is all that may be performed to achieve a desired degree of convergence. Figure 6.1a gives a tacit illustration of the incremental and the iterative processes involved.

6.1.3.2 Initial Stiffness

Also termed the residual force method [78], the initial stiffness technique involves the adjustment of elastically obtained stresses based on Eq. 6.1 and

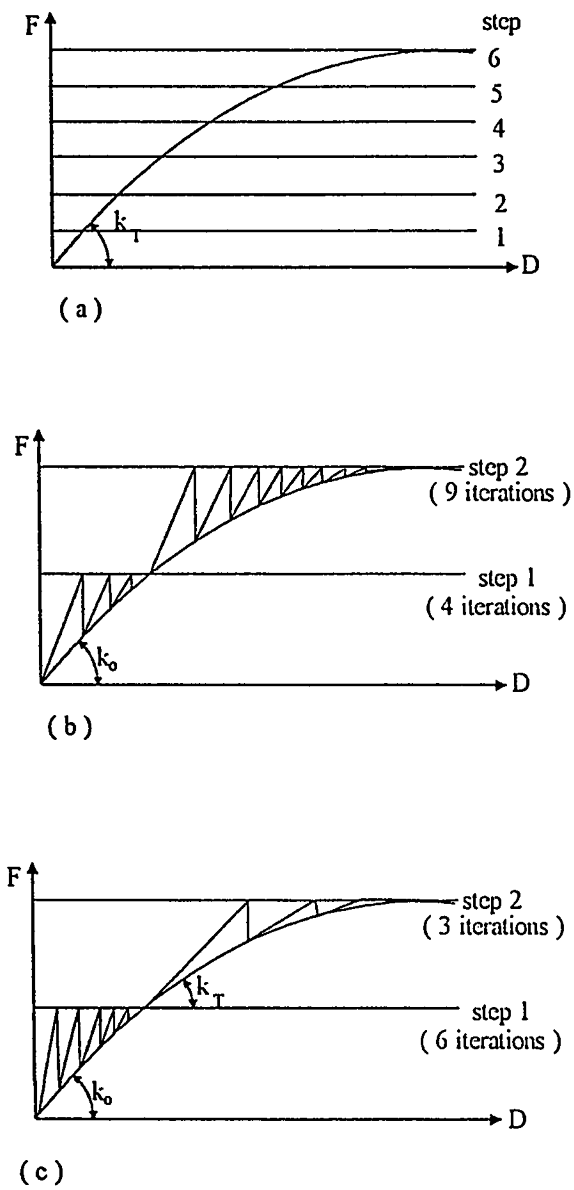

Figure 6.1: Elasto-plastic solution algorithms (a) tangential method (a) initial method (a) hybrid method

using an initial stiffness matrix $\underline{K}_{o'}$ that is calculated only once. This approach usually entails a lot of plastic strains which would be treated as fictitious loads in addition to the actual applied loads for determination of residual forces. The residual forces (see section 6.1.4 below) must then be made to vanish in an iterative manner, Fig. 6.1b.

6.1.3.3 Hybrid Stiffness

A combination of the tangential stiffness and the initial stiffness techniques, resulting in the so-called hybrid method, Fig. 6.1c, provides various other options that could be used in assuring an optimally converged equilibrium of the nonlinear stress-strain equations. Adopted in the present study are two options which in practice provide the optimum algorithm to the desired solution as follows.

1. the structure stiffness is updated at the beginning of a load increment and maintained constant during iteration to equilibrium, so that $\underline{K}^r_{i-1}$ in Eq. 6.1 is replaced by $\underline{K}^r_o$:

2. the structure stiffness is updated after the first iteration of each load increment, i.e. $\underline{K}^r_1$ is used in Eq. 6.1.

In implementing these algorithms, Fig. 6.1. an input option must be specified for use in selecting a required type stiffness. By taking a closer look at the plots in Fig. 6.1, it can be noted that in using the method of Fig. 6.1b the iterative process converges slowly (higher total number of iterations) while holding $\underline{K}_{o'}$ constant, but reformulation of $\underline{K}_{o'}$ is only performed initially, and unloading could be followed accurately. However when plasticity becomes wide spread, better convergence (fewer total number of iterations) is obtained by occasional recalculation of $\underline{K}^r_i$ and its reinversion, as in method

of Fig. 6.1c. Continued use of $\underline{K}_i^r$, as in method of Fig. 6.1a, gives faster convergence (least total number of iterations) at a greater expense of computer cost due to repeated formulation and reinversion of $\underline{K}_i^r$.

6.1.4 Residual Force Systems

Following the formulation of the nonlinear structure stiffness, the problem of load unbalance owing to the nonlinearity arise. Frequently, the calculated stress distribution ($\underline{\sigma}_i^r$) do not equilibrate the applied loads. The source of this equilibrium unbalance is largely as a result of the cited corrective procedures that are necessary to satisfy the yield condition at the end of the *ith* iteration. This occurs whenever different constitutive relationships are used for stiffness definition and stress computation [117].

Referring to the equilibrium of a typical element, the following residual force $\underline{\psi}_i^r$ will exist such that

$$\underline{\psi}_i^r = \underline{f}_i^r - \underline{P}_i^r \tag{6.2}$$

in which $\underline{f}_i^r$ is the segment of the externally applied load path and $\underline{P}_i^r$ is the internal equivalent vector due to the induced stress field $\underline{\sigma}_i^r$ satisfying the yield condition as given by

$$\underline{P}_i^r = \int_V \underline{B}^T \underline{\sigma}_i^r dV \tag{6.3}$$

where $\underline{B}$ is the matrix relating strains and displacement (constant for infinitesimal deformation problems), and V denotes the volume of the element.

6.1.5 Convergence Criteria

During the iterative procedure, the incremental displacement– nodal translations and rotations degrees of freedom– are computed using Eq. 6.1. These

are then added to previously computed and accumulated ones such that successive approximations to the true displacements are obtained according to the following recurrence relation:

$$\underline{U}_i^r = \underline{U}_{i-1}^r + \Delta\underline{U}_i^r \tag{6.4}$$

For convergence, the iteration would normally require to be terminated when either or both of the following occurs [77, 72, 78]

1. the Euclidean norm of the incremental displacements ($\Delta\underline{u}$) becomes less than a certain percentage, of the Euclidean norm of the accumulative displacement vector ($\underline{U}$).

2. the norm of the residual forces ($\underline{\psi}$) becomes less than a certain percentage, of the norm of the total applied load vector ($\underline{f}$).

Since load increments are employed in this study to effect the incremental technique, the latter convergence criteria is used in terminating the iterations (i) of any given incremental load step (r) as per the following equation:

$$\sqrt{\frac{\sum_{i=1}^{N}(\underline{\psi}_i^r)^2}{\sum_{i=1}^{N}(\underline{f}_i^r)^2}} \leq \textbf{TOLER}\ \% \tag{6.5}$$

6.2 Program Implementation

6.2.1 About PLAMBS7

In line with the major scope of the present study, a special-purpose finite element computer FORTRAN code has been developed to undertake the displacement and stress analyses of a variety of unreinforced single mitred bend problems under consideration. The computer program is called **PLAMBS7** which stands for Plastic Load Analysis of Mitred BendS and the seven(**7**) signifies the latest hierarchical number in its development sequence.

The computer implementation embraces all the previous aspects involving the incremental plasticity procedures. Specific issues of these procedures; viz-a-viz the initial stiffness algorithm, the tangential stiffness algorithm, and two options of the combined approaches are duly considered. Also included are the preceding theoretical and computational treatments presented in earlier chapters. As such, **PLAMBS7** is based on a general physical, mathematical and numerical structure that is implemented in the computer code in a modular style. This allows for straightforward modifications and additions to the code.

6.2.2 PLAMBS7 Programming Philosophy

PLAMBS7 is a problem-oriented program allowing the ability to obtain a sufficiently accurate and rational solution of a special class of mitre objects– that of single mitred bends. As a historical background to its development, most of the subroutines incorporated in **PLAMBS7** closely follow the programming philosophy and style of coding employed in the elasto-plastic solution computer program PLASTOSHELL. The robust function, reliability, and structure of the latter program are amply described in Ref. [72]. The reliability of such an approach has provided a stable base from which further built-up is made of new ideas that are central to the working program **PLAMBS7** . The inherent robustness and specialized nature of **PLAMBS7** has made it quite efficient in analyzing single mitred bend problems.

The problem orientation nature of **PLAMBS7** enables ease of automation for the analysis of the single mitre model with minimum amount of input. The program undertakes the various operations required for nonlinear analysis that includes material as well as anisotropic effects using the

layered approach. Moreover,as bequeathed by its historical development, **PLAMBS7** could as well account for geometrical nonlinear effects. For the most practical applications, the present study concerns only mechanical loads of the internal pressure and in-plane bending moment types. However, **PLAMBS7** can be a good model for a wide variety of other loads.

In what follows, the program structure and brief description of some principal features inherent in **PLAMBS7** are presented. A set of data input instructions is included in appendix A for the program. The program listing was fairly commented. This would aid tracing its logic in a straightforward manner.

6.2.3 Program Structure

Based on a structured top-down approach, the programming structure of **PLAMBS7** is modular wherein each subprogram unit is assigned explicitly to perform a particular task. A schematic diagram of the main logic involved is shown in Fig. 6.2. It is seen therefore that the program **PLAMBS7** essentially consists of an input data subroutine, generally functional subroutines, and specially developed and unified subprograms. The figure particularly highlights the order in which such principal subroutines are called by the main or master routine.

The naming of the each of the subroutines is kept as mnemonic as the principal task of the concerned routine would suggest. These program tasks are cycled by the **MASTER** routine by taking control of the call-sequence, the load increment loop (**IINCS**) as well as the convergence iteration loop (**IITER**).

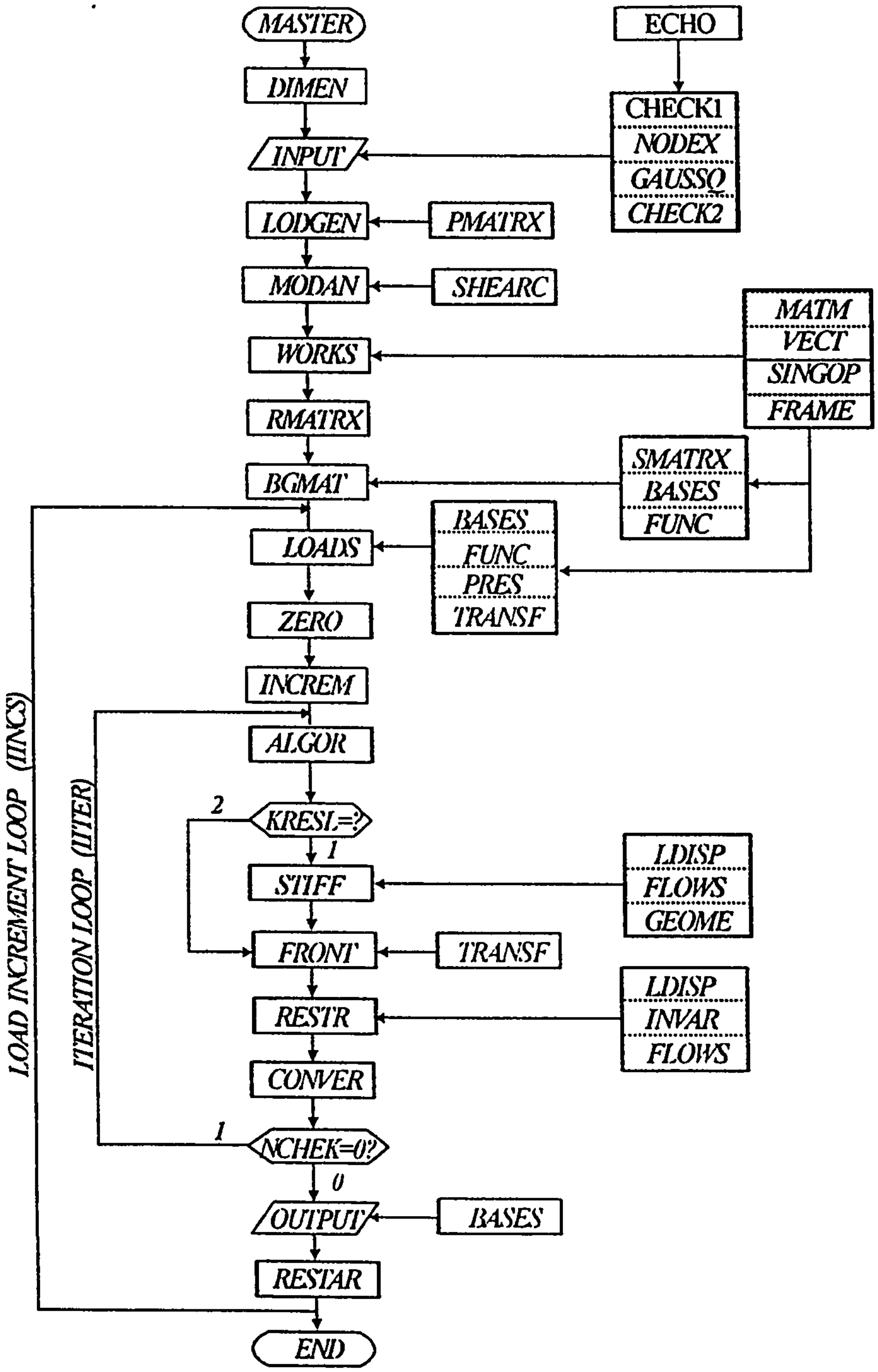

Figure 6.2: **PLAMBS7** program structure showing its logic flow and operational sequence.

6.2.4 Program Features and Description

A tremendous amount of data must be evaluated by **PLAMBS7** with precision. This requires great computational effort, and considerable numerical intricacy is required to minimize this effort. As demonstrated by the implementation of **PLAMBS7** , much emphasis has been placed on general applicability, numerical robustness, accuracy, and clarity in coding. In some instances computational efficiency is somewhat diminished to preserve these qualities. Suggestive of its operational sequence, shown in Fig. 6.2, the modular structure of **PLAMBS7** allows for code readability as well as implementation of any eventual changes which may, however, improve the efficiency. The modular structure would also ease major changes such as simultaneous study of anisotropy and elasto-plasticity as may be the case for future research studies into non-idealized composites.

The computer coding of **PLAMBS7** has been done in FOTRAN-77 and its execution conducted under AMDAHL 5580 in the VM/CMS operating environment. **PLAMBS7** is self-contained in the sense that it makes neither reference nor call to any external routine other than the usual FORTRAN built-in functions. Therefore modification of the code to run on any other installation of FORTRAN-77 compiler would not be major. The code has ran accurately using single precision with 32 bit word real and integer variables. Should the code require to run on other machines with other word lengths or other bit to byte ratios, the stated number of significant figures in the variables should at least be preserved.

All vector and array dimensions in the **PLAMBS7** computer code which vary between mitre models are combined for user convenience in the **MASTER** and **DIMEN** subroutines. Therefore, depending on a particular (size of the) mitre problem to be solved, user-required changes may be lim-

ited to rightsizing these dimensioning arrays in the **MASTER** and **DIMEN** subroutines. The subroutine **DIMEN** is used to control the size of dynamic part of the dimensioning array variables. Furthermore, the automated general nature and flexibility of the input data, particularly for boundary conditions (recieved in subroutine **INPUT**) and loading conditions (received in subroutine **LOADS**), allows easy adaptability to user-friendly and graphic input-output programming. It is important to note that, manual construction and data preparation for the mitre mesh require considerable labor, as such it may be worthwhile to obtain/develop automatic/interactive software for this purpose, especially since mesh construction is often required.

Designed to carry out a distinct set of tasks, each subroutine in **PLAMBS7** is clearly distinguished from others as succinctly depicted in Fig. 6.2. Various *channel* or *tape* numbers are also employed in the program **PLAMBS7** to aid in temporary data re-use as well as dumping of permanent data during the execution phase of the program. The former enhances the capability of **PLAMBS7** to run with minimal demand on the amount of computer core memory. The channels employed consist of channel number: 5 (input file channel); 6(data echo to the monitor); 3 (program output); 1,2,4,7, and 8 (scratch files): and 12 (permanent file required for *restart* of a problem. Almost all input data required for a given mitre problem are accepted using subroutine **INPUT**. Such data include control options, mesh topology, boundary conditions. and material properties. For loading data , the subroutine **LOADS** is specifically meant for that. In conjunction with subroutines **CHECK1, CHECK2** and **ECHO**, the subroutine **INPUT** possesses an in-built capability to perform some input error checks and diagnosis. This therefore allows the most common input modelling errors to be dealt with in the early stage of a given mitre analysis. In the case of

the mesh topology, the subroutine **NODEX** can be used to automatically generate midside/central nodes with only corner nodes specification.

The primary tasks of **PLAMBS7** include computation of displacements, stresses and force resultants for a given discretization of the mitre system. However **PLAMBS7** may also be used to simulate simpler/complex functions which are subsets/supersets of the above processes. Non-mitre shell or plate problems are potential cases in this regard. A deliberate but desirable feature of **PLAMBS7** is its use of three-dimensional analysis for accurate analysis. Within the two-dimensional curvilinear surface of the mitre shell, the third dimensionality is provided by the thickness direction as suggested by the third component of the curvilinear natural coordinate as earlier discussed in section 5.4.5. The third direction which is given as normalized input may be made to vary from point-to-point in situations where mitre of variable thickness is simulated.

A number of various load sources can be handled if directly specified in a conventional form required by **PLAMBS7** or more specifically the main load handling subroutine **LOADS**. Lacking this special method, on the part of **LOADS**, a fairly general load 'preprocessing' subroutine, **LODGEN** has been included separately in order to further preserve **PLAMBS7** modularity. In using the subroutine **LODGEN** together with another auxiliary subroutine **PMATRX**, the necessary theoretical implementation involved is based on *consistent* load formulation which is the simplest and most economical approach preserving the mathematical elegance and geometric flexibility of the entire finite-element implementation. They allow the *end-cap* part of internal pressure and in-plane bending induced longitudinal cosine load, both distributed and 'axially' directed at the free-end of the mitre, to be replaced by statically equivalent nodal loads. The approach

is robust and accurate since it had been employed using proper standard finite-element approximation terms. In specifying these loads, a user provided option **ILOAD** together with the internal pressure (**ILOAD** $=$ **0**) or in-plane bending (**ILOAD** $=$ **1**) value is all that is required for automatic account of the corresponding load.

Mitre edge boundary conditions can be specified locally by virtue of the mitre edge coordinate system (in subroutine **RMATRX**). In this way the necessity of analyzing the entire or half of the mitre structure is no longer required. Only a quarter of the model is sufficient. Moreover the ability to prescribe mitre edge associated boundary conditions in this coordinate is of particular importance since no single other coordinate system could otherwise be used in this regard. The necessary account for this is efficiently taken during the execution phase of subroutine **BGMAT** instead of **STIFF**. Subroutine **BGMAT** forms the B-matrix which is used repeatedly in the incremental **IINCS** and iterative **IITER** loops to generate the structure stiffness matrix. By avoiding the use of **STIFF** in this regard, the expense entailed by repeated generation or execution of **STIFF** is significantly curtailed.

A relatively large cache of elements is available in **PLAMBS7** via the subroutine **BASES**. This was meant to qualify **PLAMBS7** against unforseen numerical difficulties that are often not uncommon in finite element analysis. Based on suitably high order displacement field, the elements easily lend themselves to simulation of irregular helicoidal geometries of the mitred bends.

Other computing economy and practical efficiency provided by **PLAMBS7** involves combination of various factors. Amongst these is the use of the FRONTal method [121] of equation solving which reflects the novel features of Irons [122] classical program. This technique is implemented us-

ing the subroutine **FRONT**. The FRONTal equation solving technique has earned the reputation of being inexpensive to use [72]. Its efficiency [123] and advantages [124] over other algorithms such as *banded* and *skyline* equation solvers makes it not just another fancy algorithm but in all regards a paragon of finite element analysis.

As a further safeguard against unforeseen numerical instabilities, various options of numerical integration–normal, selective and reduced–are flexibly usable in **PLAMBS7** . This aspect has been very crucial owing to the *what-if or if-then* prediction of the mitre analysis. The subroutine **GAUSSQ** is central towards this. To accommodate large loading regimes, **PLAMBS7** is designed to provide a **RESTART** facility. The restart capability would essentially enable an earlier executed problem to restart from a converged state it had previously stopped. The implementation of such a task is done by the combination of subroutines **ZERO** and **RESTAR**, Fig. 6.2. Finally, a primary as well as secondary set of results in terms of displacements, stresses and stress resultants could be generated and printed. Controlled by a user-specified output option, **PLAMBS7** is designed to provide various levels of these output which could be for any iteration and/or increment. The subroutine **OUTPUT** is a direct proxy towards this.

Chapter 7

APPLICATIONS, RESULTS AND DISCUSSIONS

7.1 Introduction

The major focus of this chapter is to document the verification and utilization of the special purpose program **PLAMBS7** . The range of problems considered encompasses single mitred bends differing in loading type, material and geometrical nonlinearities as well as anisotropic construction. In line with outlined scope of the study, only pressure and in-plane bending are considered. Extracting as much detailed information as the analyzed problems would allow has been a major reason for the latter emphasis. Before embarking on this, some aspects of the study which are quite ancillary to the forthcoming presentation are considered in the following section.

7.2 Model Development

7.2.1 General Considerations

Single mitred bends used in this study are generally those with equal leg length (L) on either side of the mitre plane. The mitre wall thickness (t) has been taken to be constant throughout the mitre domain. Owing to this, geometrical symmetry has readily prevailed and as such only a quarter of

the whole mitre structure has been considered for analysis. The symmetry consideration has the decided advantage of allowing reduced computation cost and mesh generation complexities that are inherent in the mitre analysis.

7.2.2 Mitre Mesh Modelling

For numerical modelling of the mitre joint, a pre-processing Finite Element package is undoubtedly desirable [125]. The same can also be said about the need for post-processing routines. This fact is further supported by the complexity of the helicoidal discontinuity forming the oblique mitre plane. As such, the development of an appropriate mitre mesh model for this study has not been an easy task.

Proper discretization in space is vital in obtaining accurate simulation of the mitre response with a numerical model such as the one under discussion. Adequate discretization is vital for two reasons:

1. The ability of a model to represent the variation in mitre parameters and to simulate the complex stress patterns depends on the fineness of discretization.

2. The accuracy and stability of the numerical method used to represent the spatial mitre geometry. in particular, large mitre angle, depends on the spatial discretization.

A *sufficiently good* discretization allows for accurate simulation of stresses and displacement variations at the scale of interest, but the goodness of a discretization is a relative rather than absolute factor, and thus the inconclusiveness. But as a rule of thumb, enough elements must be present to capture the anticipated sharp stress gradients around the hot-spot areas of the mitre edge. However, too fine a mesh would be too costly for an effective analysis.

In general, a good mitre mesh is found to be a model for smooth elbow but with finer mesh near the helicoidal mitre edge. Such a model has proved to be adequate in accounting for the mitre edge influence, notably within twice the characteristic length [40]. Therefore, the size of the elements in the vicinity of the mitre edge and, for in-plane bending, the area near the point of application of the load should relatively be smaller when compared to element sizes in other regions. The fineness required is that which makes the nodewise or elementwise discretization of the mitre domain or parameter values a good representation of the actual domain distributions. Nevertheless, judgement must be exercised in discretization, and such results may be tested by *experiment* with various discretization in a parametric sense.

7.2.3 Basic-Mesh Models

Proper consideration of the points raised in the preceeding discussion has resulted in the design of two basic-mesh models. A and B. Two-dimensional views of the meshes are shown as Fig. 7.1a and b for models A and B respectively. Screening investigations that were carried out have shown that both the basic-mesh models A and B possess a satisfactory mesh density distribution throughout the modelled mitre domain. The first basic-mesh, model A (Fig. 7.1a) consists of 108 basic-elements (12 x 9) and was obtained based on mesh synthesis carried out for single mitred bends subjected to internal pressure loading. On the other hand, the special nature of in-plane bending moment loads has imposed the necessity of increasing the size of this mesh to a total of 168 elements. Fig. 7.1b.

7.2.4 Loading System

As has been highlighted, two types of loads comprising internal pressure and in-plane bending moment are of interest in this study. For internal pressure

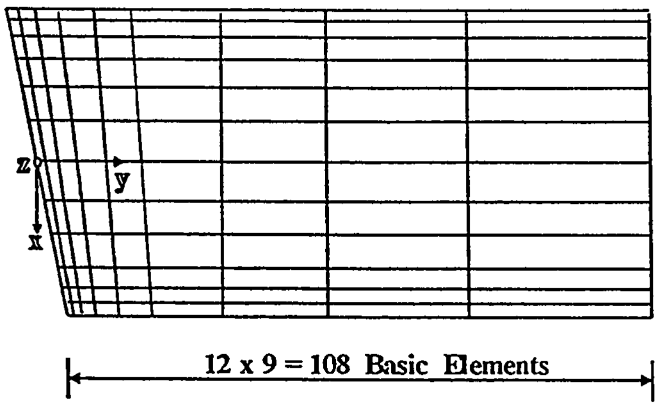

(a) MESHA

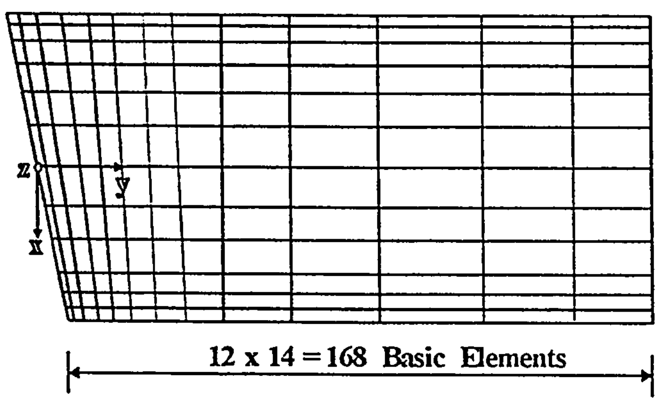

(b) MESHB

Figure 7.1: Basic-mesh models (a) **model A**: 108 basic-elements (utilized for internal-pressure) (b) **model B**: 168 basic-elements (utilized for in-plane bending).

it is essential to the analysis that the *free* end of the single mitred bend be *closed*, perhaps with an end-cap or flexible membrane . This would enable the pressure to be contained thereby permitting the simulated mitre assembly to be in static global equilibrium which in this case is a necessary condition for the entire mitre problem to be solved.

In **PLAMBS7** it is possible to specify the existence of pressure loads directly once the surface element(s), over which the pressure is acting, is appropriately registered. However since the basic mitre mesh models just presented were not designed to simulate the entailed *closure or end-cap*, this aspect of loading could not be wholly modelled. In this regard, the end-cap part of the pressure is indirectly specified through the use of equivalent longitudinal nodal forces that must be computed to be statically equivalent to the distributed pressure incident on the end-cap. When such computation is done, the consistent nodal force vector, corresponding to one side of a typical element along the free-edge, can be explicitly written in vector form as

$$p_i^e = \left\{ \begin{array}{c} p_1 \\ p_2 \\ p_3 \end{array} \right\} = \frac{\pi a^2 p_0}{12 N_H} \left\{ \begin{array}{c} 1 \\ 4 \\ 1 \end{array} \right\} \tag{7.1}$$

For brevity, the full derivation and terminologies of the terms involved are given in section C.2 of appendix C.

When an in-plane bending moment (M) is applied at the free-edge of the mitred bend, an axial load (N_y) distribution of the form $N_y = q_o \cos\theta$ would result at the free-edge. Converting this to equivalent nodal load vector the following expression is obtained:

$$\left\{ \begin{array}{c} p_1 \\ \\ p_2 \\ \\ p_3 \end{array} \right\} = a q_0 \left\{ \begin{array}{ccc} -\sin\theta_1 & \frac{1}{2}(\cos\theta_3 + 3\cos\theta_1) & -(\sin\theta_3 - \sin\theta_1) \\ \\ 0 & -2(\cos\theta_3 + \cos\theta_1) & 2(\sin\theta_3 - \sin\theta_1) \\ \\ \sin\theta_3 & \frac{1}{2}(3\cos\theta_3 + \cos\theta_1) & -(\sin\theta_3 - \sin\theta_1) \end{array} \right\} \left\{ \begin{array}{c} \mu \\ \\ \mu^2 \\ \\ \mu^3 \end{array} \right\} \tag{7.2}$$

Full details regarding derivation and explanation of the necessary terms involved in Eq. 7.2 are given in section C.3 of appendix C. Thus for a typical element whose three nodes 1, 2, 3 (taking in the positive direction of θ in radians) correspond to the element side that is reposed to the free-edge, the latter consistent nodal load vector is then statically equivalent to the applied in-plane bending moment (M) at that free-edge.

7.2.5 Boundary Conditions

Displacement boundary conditions are generally dependent on the loading conditions and the physical constraints on the mitre structure [126]. However, since only geometrically symmetric single mitred bend with equal leg-lengths are hereby analyzed, the internal pressure and in-plane bending load types under consideration do not impose the stated load dependency. Taking advantage of this geometric and loading symmetry, for all the single mitred bends analyzed, only a quarter of the mitre has been modelled, thus creating planes of symmetry–in the x-y plane for the intrado and extrado lines and in the oblique sense across the helicoidal mitre edge intersection–as could be discerned from coordinate convention used in Fig. 7.1. Consequently, boundary conditions which in this case are essentially continuity conditions, have to be applied to the nodes which lie on these planes of symmetry to ensure that the mitre model behaves as it would do if a complete single mitred bend was analyzed. Referring to Fig. 7.2, the following continuity conditions are therefore considered:

- nodal displacements perpendicular to the oblique plane of symmetry are restrained: $v_{k'} = 0$;
- nodal rotations that are tangential to the mitre-edge and parallel to the oblique plane are restrained: $\alpha_{k'} = 0$;

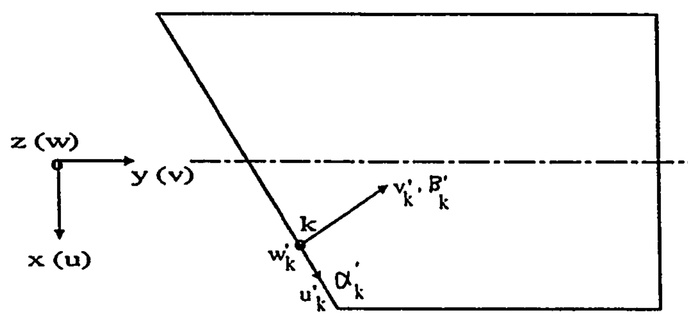

(a)

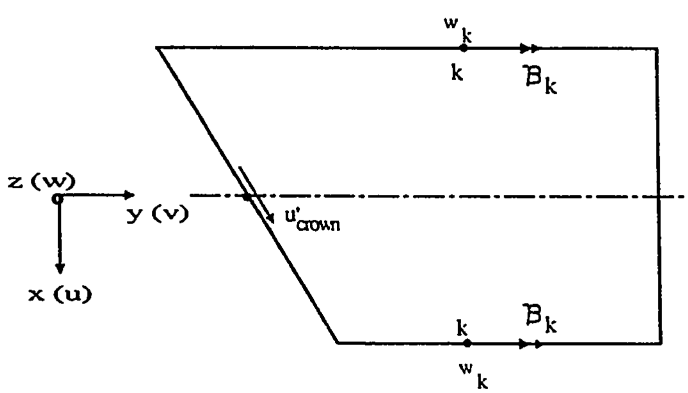

(b)

Figure 7.2: Continuity boundary conditions. (a) mitre-edge (b) vertical ($x-y$) plane of symmetry.

- nodal displacements perpendicular to the vertical plane of symmetry are restrained: $w_k = 0$;

- nodal rotations with direction parallel to the intrado/extrado lines of the vertical plane of symmetry are restrained: $\beta_k = 0$;

- to isolate rigid body translation the crown of the mitre-edge is constrained: $u|_{crown} = 0$.

7.3 Application Assessment

To assess the applicability of the finite element implementation of the computer code **PLAMBS7** , a careful selection of numerical problems must be made. The problems selected include nonlinear effects due either to elasto-plastic material behavior. geometric nonlinearity or combination of both. In assessing the accuracy, categorization of the problems is made into two parts. The first part presents results of the analysis based on problems reported in the literature and are therefore for comparison. The second part comprised a set of problems that were specifically chosen to illustrate other aspects of the study not necessarily available in the literature.

7.3.1 Comparison Problems

7.3.2 Elastic Mitres

7.3.2.1 Internal Pressure

The first assessement problem involves the elastic behavior of unreinforced single mitred bend under internal pressure. Experimental and theoretical results for this problem were reported in graph form by Owen and Emmerson [6]. The graphs were therefore discretized to allow later comparison with results generated for the same problem using **PLAMBS7** . The dimen-

sions and material parameters of the mitre model are as follows (a) Geometry; $\alpha = 15^o$, $t = 2.5mm$, $a = 50.8mm$, $L = 216.8mm$ (b) Material: $\bar{E} = 14480.0MPa$ and $\nu = 0.5$.

The finite element discretization employed for the mitre model is the 108 element basic-mesh model A shown in Fig. 7.1a. Integration was done based on reduced (in-plane) integration rule (2x2) and extended-layered approach in which one layer and three gauss points were used for across the thickness integration (1Lx3). Altogether the integration scheme can be symbolically presented as 2x2x1Lx3. The results of the analysis are shown in Fig. 7.3 for comparison. The stress plots are shown in a nondimensional form by normalization with respect to the nominal stress pa/t, where p is the internal pressure, a is the mean pipe radius and t is the pipe wall thickness

Examination of Figs. 7.3a and b, giving the variations of hoop and axial stress ratios, respectively, around the section of the mitre edge, shows that the agreement between **PLAMBS7** and experiment is generally good. The outside hoop stress at the intrado ($\theta = 0^o$) side of the mitre edge is the maximum stress occurring in the mitred bend and this value is adequately picked-up by **PLAMBS7** . In Fig. 7.3, the behavioral pattern between the experimental and the **PLAMBS7** hoop stress is more in tune than that between the experimental and the theoretical hoop stress. However a difference in the hoop stress magnitude is noted at the intrado where **PLAMBS7** prediction for the outside hoop stress, although still the maximum stress occuring in the bend, is lower than experimentally measured value. For the inside hoop stress, **PLAMBS7** tend to give higher value at the intrado side of the mitre-edge. Possible explanation for the latter instances is given when overall picture of the stress parttern along the intrado (later in Fig. 7.4a) is presented.

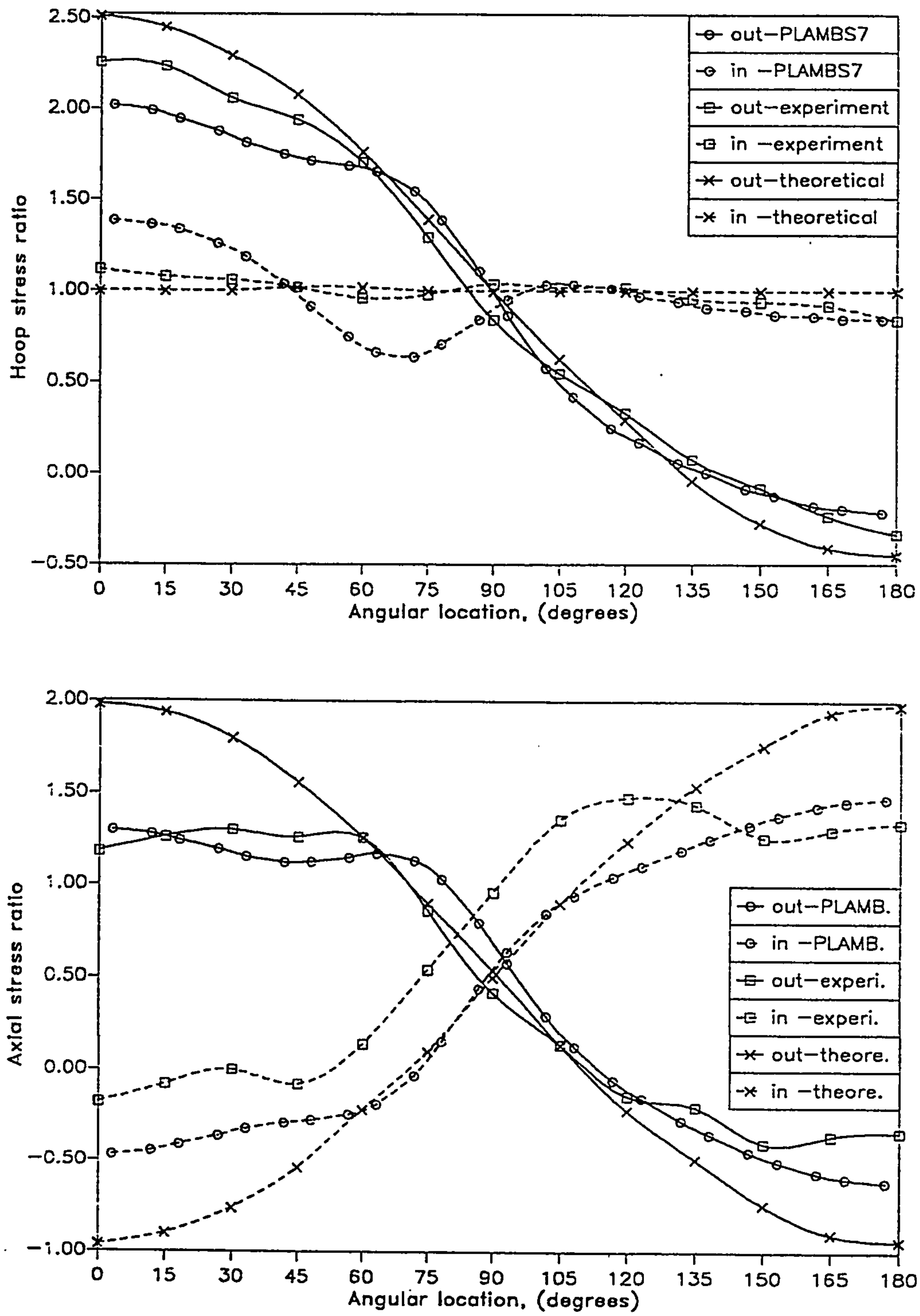

Figure 7.3: Comparison of stress distributions along the mitre-edge (a) hoop stress (b) axial stress.

Referring to Fig. 7.3b, considerable discrepancies in the intrado ($\theta = 0^o$) and extrado ($\theta = 180^o$) sides of the mitre edge are seen to occur between the theoretical and experimental distributions of the axial stress around critical section at the mitre edge. In exhibiting its satisfactory performance, the **PLAMBS7** prediction has closely matched the experimental results. The closeness becomes much more noticeable at the critical points, notably the intrado and extrado ends of the mitre edge. The theoretical maximum values at these critical points for the axial stress is overestimated by an error margin. This error margin is more than can be accounted for by experimental inaccuracies and might be attributed to inherent limitations such as lack of three-dimensional effects in the theoretical analysis. Coupled with the edge criticality, it is therefore expected that the discrepancies between the theoretical and the experimental results would become more pronounced as the mitre angle (α) is increased. Irrespective of the mitre angle, however, such limitations do not lend themselves to **PLAMBS7** results, since three-dimensional effects had been duly considered for **PLAMBS7** implimentation.

The **PLAMBS7** and experimental distributions for the hoop and axial stresses along the axes of the intrado ($\theta = 0^o$) and extrado ($\theta = 180^o$) are successively shown in Fig. 7.4. Except in Fig. 7.4a, excellent agreement exists between the stress ratios both in terms of magnitude, rate of decay in amplitude and wavelength of fluctuation. Moreover, at a distance from the mitre edge of about twice the characteristic length of the bend, both the hoop and axial stress ratios attained a constant value equal to the value occurring in a long closed thin-walled circular cylindrical pipe subjected to internal pressure. The constant value was therefore not unexpected but served to further indicate the level of confidence in **PLAMBS7** predictions.

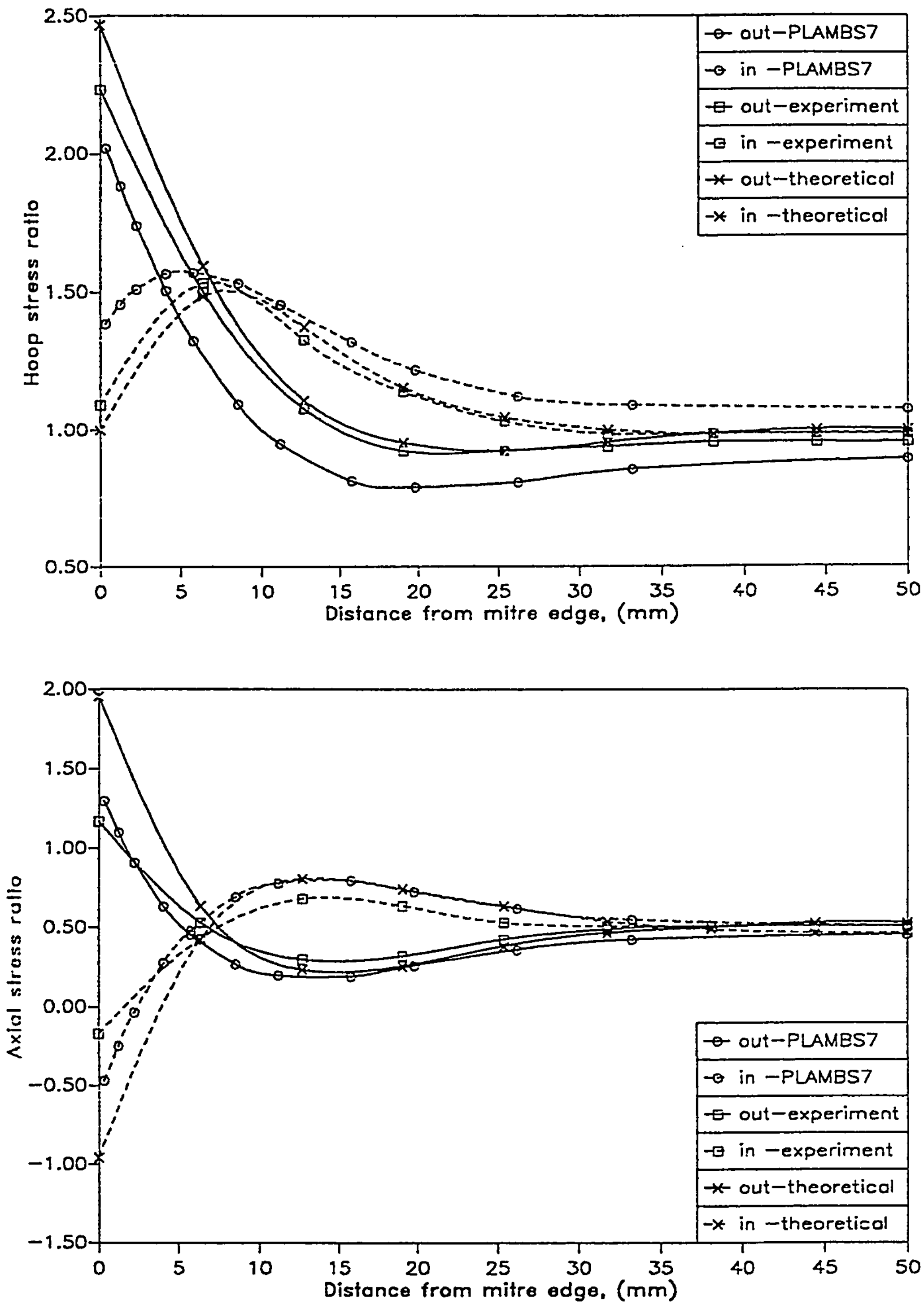

Figure 7.4: Comparison of stress distributions along the intrado axis (a) hoop stress (b) axial stress.

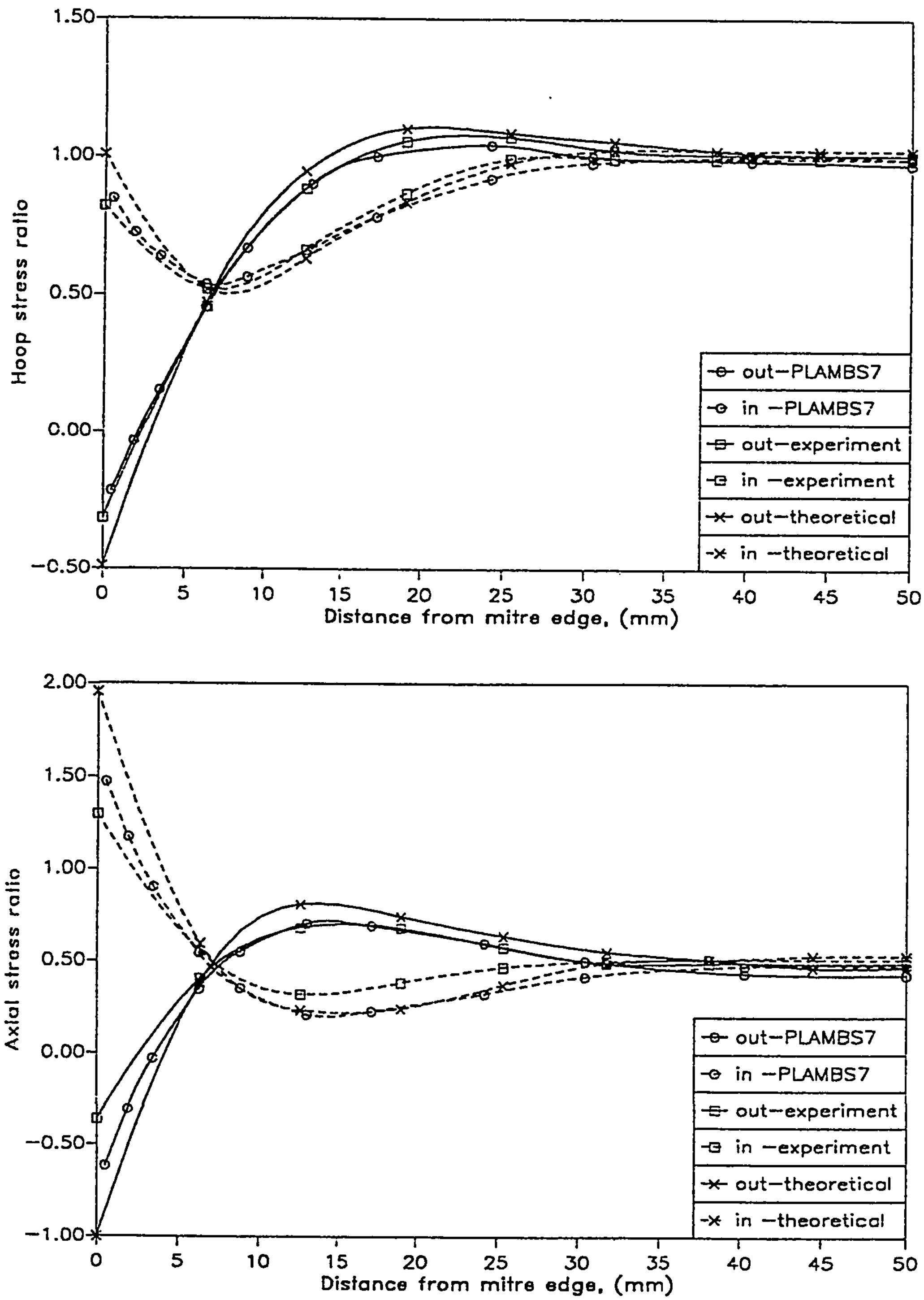

Figure 7.5: Comparison of stress distributions along the extrado axis (a) hoop stress (b) axial stress.

In the case of Fig. 7.4a, for hoop stress along the intrado axis, the **PLAMBS7** and experimental stress variation patterns are qualitatively in close agreement. Quantitative wise, however, the outside hoop stress appears to be generally below experimental estimate while the inside hoop stress seems over predicted. This trend is nonetheless consistent with the magnitude of hoop stress amplitudes occurring at the mitre edge in Fig. 7.3a. Being the maximum stress occurring in the bend, coupled with short leg length at the intrado in comparison to the extrado, the hoop stress at the mitre edge (distance = 0) is predominantly bending stress. Most likely therefore the hoop stress appeared not accurately picked up by linearly extrapolated experimental measurements based on outside surface strains. The persistence of the predominantly hoop stress from the mitre-edge upto the free-end of the mitre, where stress components are known to be membrane, is indicative of the strong edge influence due to the short leg length at the intrado.

7.3.2.2 In-Plane Bending

To assess the accuracy of the finite element computer code **PLAMBS7** to in-plane bending of unreinforced single mitred bend, the second problem was sought based on the theoretical and experimental works of Jone and Kitching [21, 15]. The following geometric and material characteristics, as obtained from Ref. [21], are therefore used for the **PLAMBS7** solution (a) Geometry : $\alpha = 45^o$, $t = 5.6mm$, $a = 107mm$, $L = 1144.6mm$ (b) Material : $E = 202713MPa$, $\nu = 0.27$.

One quarter of the single mitred bend was analyzed by **PLAMBS7** under loading conditions which replicated the experiments [21, 15]. The finite element mesh used is the basic-mesh model B shown in Fig. 7.1b. The integration scheme used is the same as for the pressure situation. To provide

the basis for comparison, results of the analysis have been normalized with respect to the maximum longitudinal (axial) membrane stress $\sigma_n = M/\pi a^2 t$ arising in a straight pipe of the same dimensions.

Figures 7.6a and b show, respectively, the hoop and axial stress ratios around the mitre-edge obtained from **PLAMBS7** when compared with experimental and theoretical stress ratios reported in Ref. [15]. The **PLAMBS7** outside and inside hoop stress distributions follow closely the experimental and theoretical curves, except in the regions around $\theta = 0^o$ where the experiment underestimates the larger inner hoop stresses.In close proximity to the mitre-edge, strains undoubtly vary rapidly.This, and coupled with the limited space over which strain gages had to be mounted, is a possible explanation to some of the observed discrepancies.The **PLAMBS7** values, for instance, were reported for gauss points which are only 4mm away from the mitre-edge and are therefore much closer to the mitre-junction when compared with the experimental values which are for points 13mm remote from the mitre-edge.The theoretical values are, however, for points right on the mitre-edge. The distribution of the axial stress ratios between the three set of curves, based on **PLAMBS7** , experiment and the theory, are seen to follow each other closely in Fig. 7.6a. In the region $90^o < \theta < 180^o$, **PLAMBS7** and experimental axial outside stress distributions are similar whereas the theoretical values are considerably diverging.

Figures 7.7a and b compare **PLAMBS7** values with corresponding experimental curves of Ref. [21] along the axes $\theta = 90^o$ (the crown) for the hoop and axial stress ratios, respectively. No theoretical results are shown in the latter plots, since theoretical values are only obtainable at the mitre-edge [15], as shown in the earlier plots, Fig. 7.6.

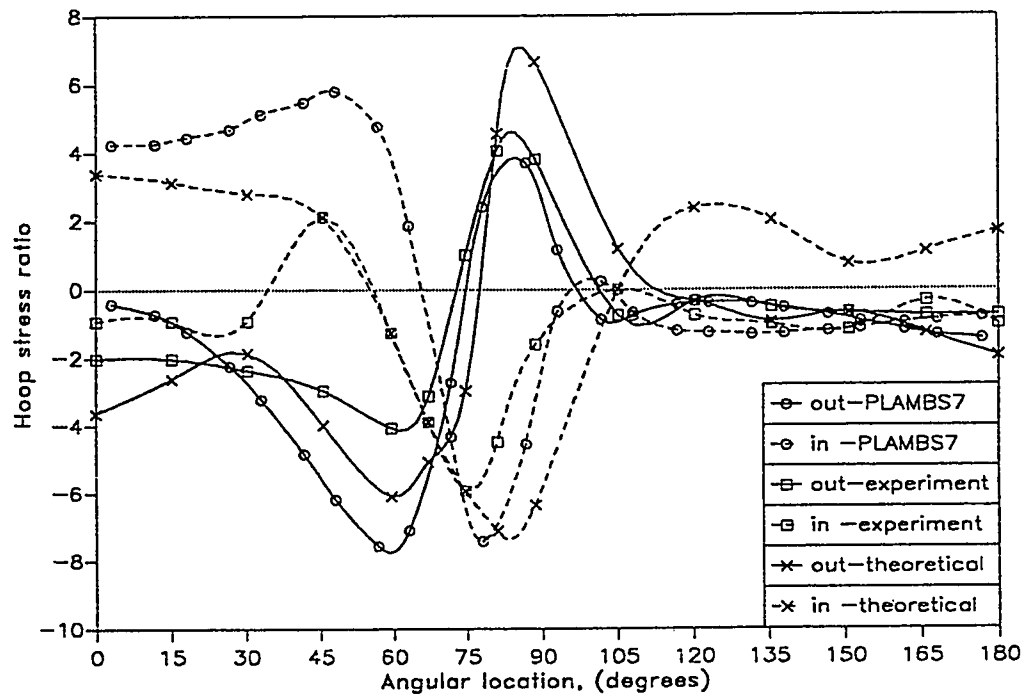

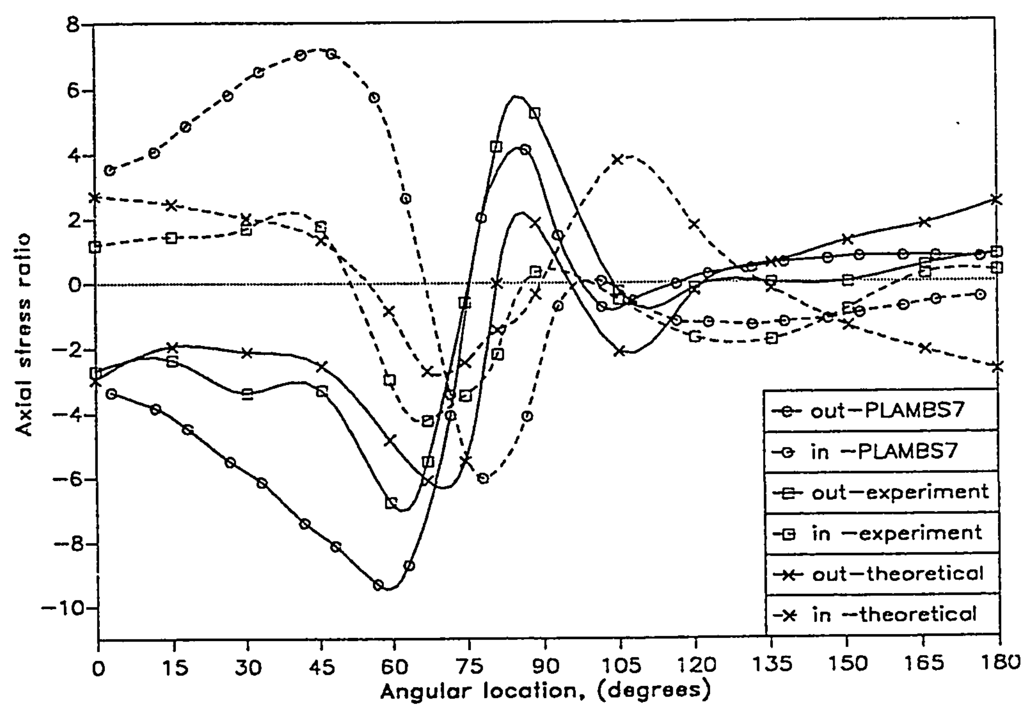

Figure 7.6: Comparison of stress distributions along the mitre-edge (a) hoop stress (b) axial stress.

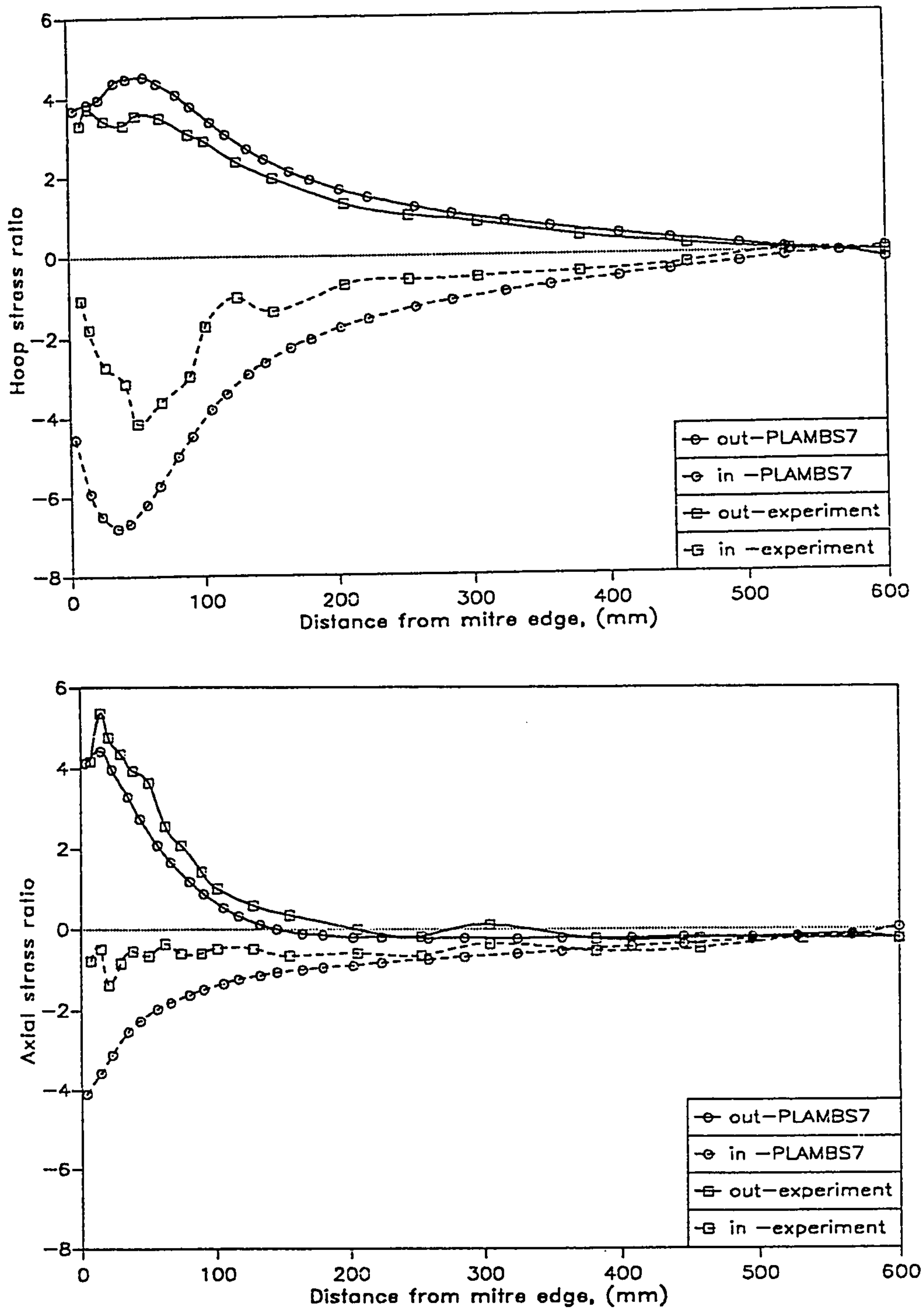

Figure 7.7: Comparison of stress distributions along the crown axis (a) hoop stress (b) axial stress.

7.3.3 Elasto-Plastic Mitres

7.3.3.1 Internal Pressure

For the present treatment, no experimental results were available. However, the main intent of solving the problem is to demonstrate the capability of the extended layered approach prior to its use for elasto-plastic in-plane bending problem, the latter being the third comparison problem with corresponding results in the literature [54].

Following the linear elastic analysis of the single mitred bend under internal pressure, the present elasto-plastic analysis uses the mesh and geometry as in the preceding comparison problem. section 7.3.2.1, in addition to the following elasto-plastically tuned material characteristics: $E = 30000MPa$, $\nu = 0.5$, $\sigma_0 = 30MPa$, $\tau_0 = 17.32MPa$, and $H\prime = 300MPa$.

In investigating for an appropriate extended layered model that adequately represents the elasto-plastic responses of such a mitre, numerical experiments have been conducted using selective (in-plane) integration (3 x 2) and accros-the-thickhness integration based on the following thickness discretization schemes:

1) simple layered model in which nine (9) separate but fictitious layers were used with one-point integration rule (3x2 x 9Lx1 scheme).

2) extended layered model in which three (3) separate but fictitious layers were used with three-point integration rule (3x2 x 3Lx3 scheme).

3) extended layered model in which two (1) separate but fictitious layers were used with three-point integration rule (3x2 x 2Lx3 scheme).

During the course of incrementing the pressure loading, the elasto-plastic response in terms of a nodal (radial) displacement and a nodal rotation at

key locations corresponding to nodes at the intrado of the mitre-edge and intrado of the free-edge respectively were monitored. Therefore, Fig. 7.8 indicates how the radial displacement and end-rotation, based on the three highlighted schemes, were compared for condition of load increments upto complete collapse in each.

With only one-third to one-fifth the number of layers in scheme 1 (simple layered model), the agreement showed by the remaining schemes 2 and 3 (extended layered models) is immediately apparent throughout the elasto-plastic history. Nonetheless, in approaching collapse, scheme 1 (3x2x9Lx1) was noted to show sudden numerical instability beyond which further loading was inhibited even at smaller load increments. Similar behavior was noted in the case of scheme 3 (3x2x2Lx3). An exception is that just beyond the initial instability further loading was possible and as such much larger deformation was observed prior to a subsequent instability which culminated to complete collapse for the scheme 3.

Referring to Fig. 7.8, the plot for scheme 2, was noticed not to exhibit any initial instability, but instead continued much more smoothly until, at last, it became unstable at relatively the same complete collapse-load as in scheme 3. Occurring at such a threshold level of response, the smoothness behavior is an apparent desirability that distinguishes scheme 2 (3x2x3Lx3), rather than scheme 3 (3x2x2Lx3), to be more favorable for subsequent elasto-plastic mitre analysis, irrespective of the type of loading.

7.3.3.2 In-Plane Bending

Having established the versatility of the extended layered approach towards elasto-plastic mitre analysis, the present section identifies one of the crucial tests so far for **PLAMBS7** —that of elasto-plastic in-plane bending analysis

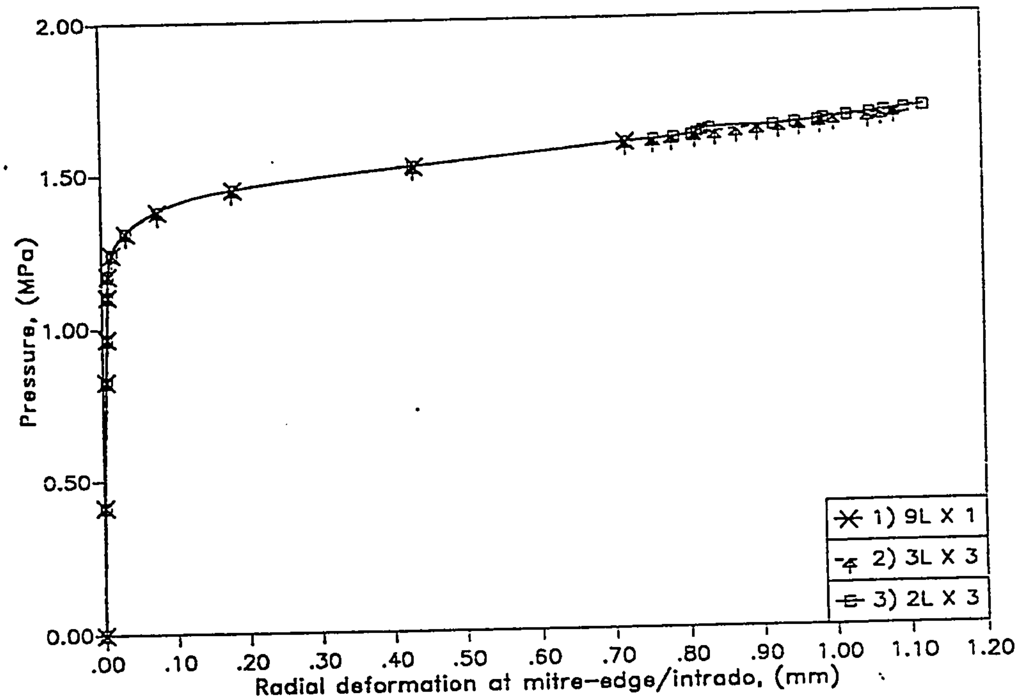

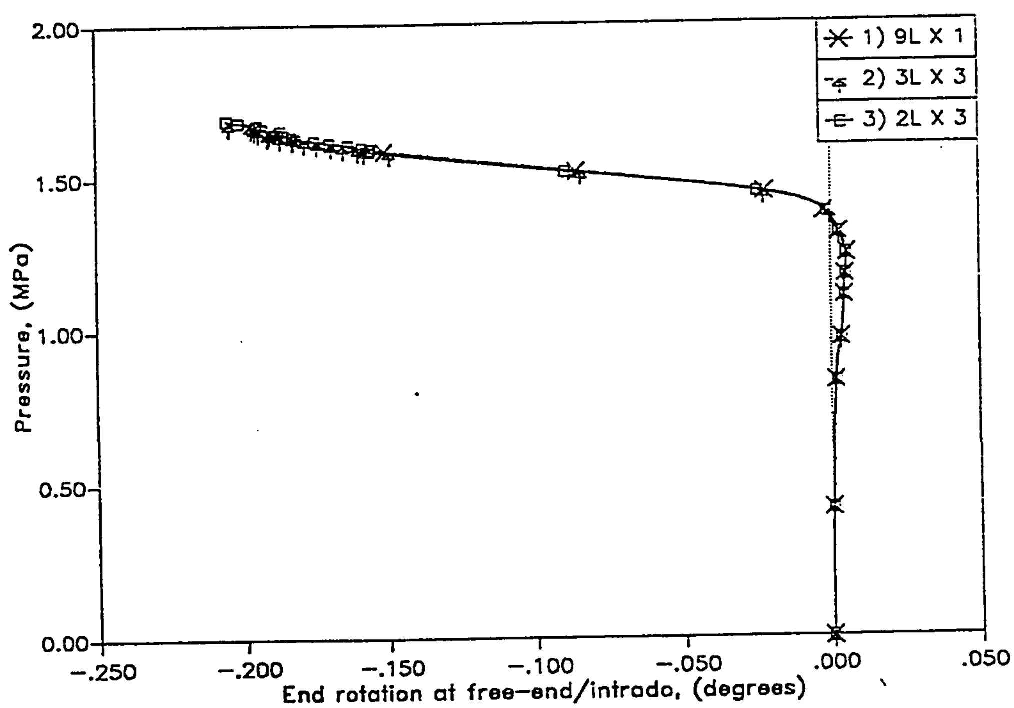

Figure 7.8: Comparison of Load-Displacement curves for three layered-model schemes.

of single mitred bends, of large mitre angle α.

7.3.3.2.1 Geometry and Material Specification In the experimental study in Ref. [54], two mitre models ($\alpha = 30^o,\ 45^o$) of unequal leg-lengths were used. To effect the in-plane bending moment, a single vertical load (P) was applied at the free-end of the shorter leg (length L_1) which was oriented horizontally while the other leg (length L_2) was held vertical and fixed at its end. However, for the purpose of numerical verification using the general purpose finite element program ABACUS, the authors in Ref. [54] assumed that the behavior near the mitre-edge in a single mitred bend with unequal legs ($L_1 < L_2$) and a single vertical load (P) would be very similar to the behavior at the mitre-edge in a single mitred bend with equal legs ($L = L_1$) and subjected to a pure in-plane bending moment (M_z) of magnitude equal to a couple PL. Therefore in order to provide a basis for complete comparison, the nonlinear material and geometric analysis by **PLAMBS7** was done on the 45^o single mitred model under conditions which replicated the numerical work in Ref. [54]. The 30^o model was undertested in [54], and as such was not considered suitable for comparison.

For the 45^o, aluminum was used.Deduction of the material properties from Ref. [54] would therefore give (a) Geometry : $\alpha = 45^o$, $t = 3.45mm$, $a = 81.25mm$, $L = 637.5mm$ (b) Material : $E = 71010MPa$, $\nu = 0.33$, $\sigma_0 = 89.60MPa$, $\tau_0 = 51.76MPa$.

Similar to the numerical treatment using ABACUS in the cited reference, Ref. [54], the strain hardening parameter $H\prime$ is also taken to be zero in the **PLAMBS7** analysis.

7.3.3.2.2 Load-Deformation Curves The plot of the in-plane bending moment versus rotation of the intrado point of the free-edge are shown in

Fig. 7.9 as obtained from **PLAMBS7** analysis. In the plot, results based on the ABACUS analysis [54] for the geometrically linear closing-moment, nonlinear closing-moment, and nonlinear opening-moment are also given. The agreement between the two models (**PLAMBS7** and *ABACUS*) in the elastic range is good. However, beyond the elastic range the influnce of geometric nonlinearity is immediately apparent, and therefore the two models show different tendencies in values but not in form.

Outside the elastic range, the corresponding curves for opening-moment continued to match each other which, nonetheless, is not the case for the remaining two pairs of curves— representing the linear closing-moment and nonlinear-closing-moment in Fig. 7.9. In closing modes, the moments for each of the two compared models, attained a certain critical value and thereafter proceeded asymptotically towards collapse. For the opening mode, the bending moment carrying capacity is higher and seemed to increased monotonously without weakly collapse instabilities for both the **PLAMBS7** and the ABACUS models. For both the (geometrically linear and nonlinear) closing moments the **PLAMBS7** estimates for the bending at complete collapse is about 35% higher than the corresponding values based on the ABACUS prediction. However, before commenting on this seemingly large out-of-fit between the two models, it is necessary to slightly digress into some remote but relevant details of Kitching et. al. results [54].

Based on separate estimate (using Fig. 9 of Ref. [54]), the ABACUS prediction for the limit load is about 23% lower than would be obtained from experimental plot of an end-load versus end-deflection for the 45^o mitre model under consideration. However, instead of this separately estimated value, 23% (less), the authors in Ref. [54] had reported 7% (less). Eventhough experimental results showed significant strain hardening before material col-

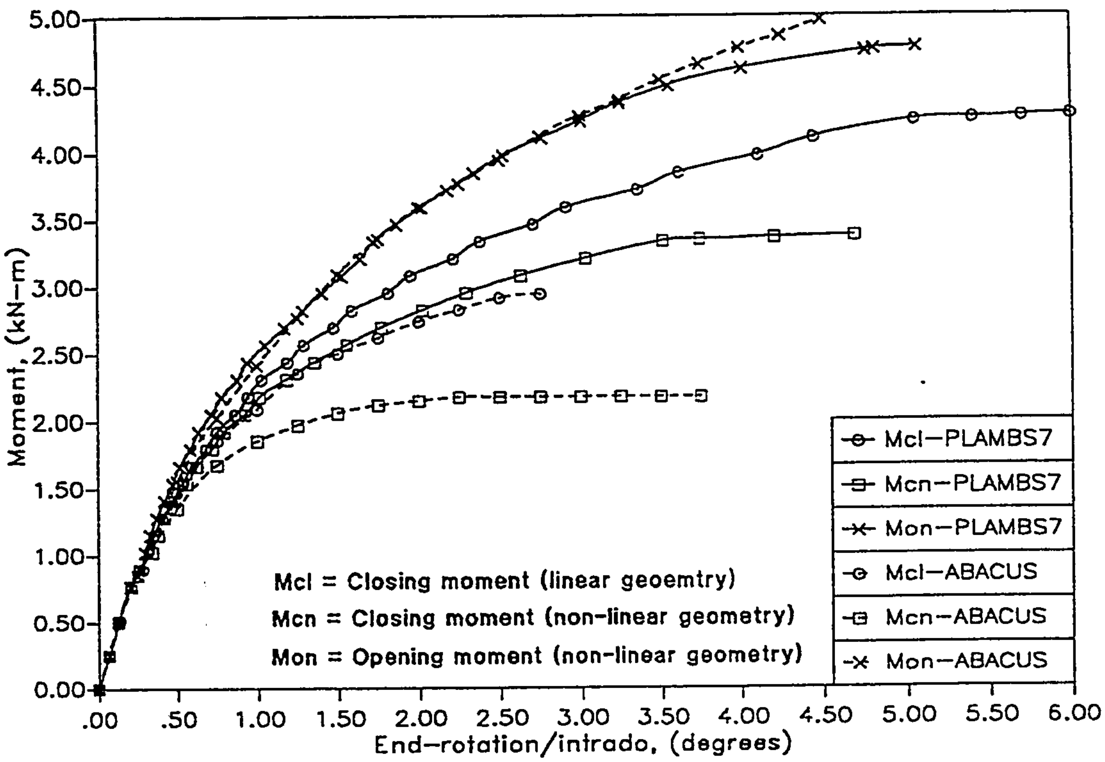

Figure 7.9: Comparison of Moment End-rotation curves of PLAMBS7 and ABACUS analysis.

lapse [54], the 23% difference between the ABACUS and the experimental limit load estimates is more than can be accounted for by consideration of zero strain hardening in the ABACUS analysis, or experimental inaccuracies for that matter. This ends the digression.

On the other hand, the **PLAMBS7** results would be 12% over the experiment and hence is an upper bound—consistent with a recognized tendency for all displacement based finite element models. In view of the above and other considerations, such as inaccuracies in experimental measurements and in load applications, it is expected that the overall elasto-plastic behavior based on **PLAMBS7** predictions will be qualitatively reliable and numerically accurate.

Figure 7.10a indicates how the end-rotation at the intrado of the free-edge compare with those at the crown and extrado points of the free-edge of the single mitred bend under (geometrically) linear closing-moment. The corresponding curves for nonlinear closing-moment and nonlinear opening-moment are respectively represented in Fig. 7.10a and b. In contrast to a beam-type bending it is seen from the plots in Fig. 7.10 that depending on the axial fiber location at the free-edge of a single bend under in-plane bending, different deformation or end-rotations could be anticipated.

In the case of both the closing moments (intrado compressed), the compressed portion of the free-edge showed tendency for increased end-rotation which is diverging when compared to the stretched (extrado) portion of the free-edge. The behavior at the crown (supposedly neutral) is seen to be somewhere in between that for the extrado and the intrado, Fig. 7.10a and b. Consideration of the fact that under under bending, compression 'prevents' flattening of the mitre-edge cross-section while tension 'accelerates' it [60], it appeared as though the 'restricted' flattening (which is largely at the ex-

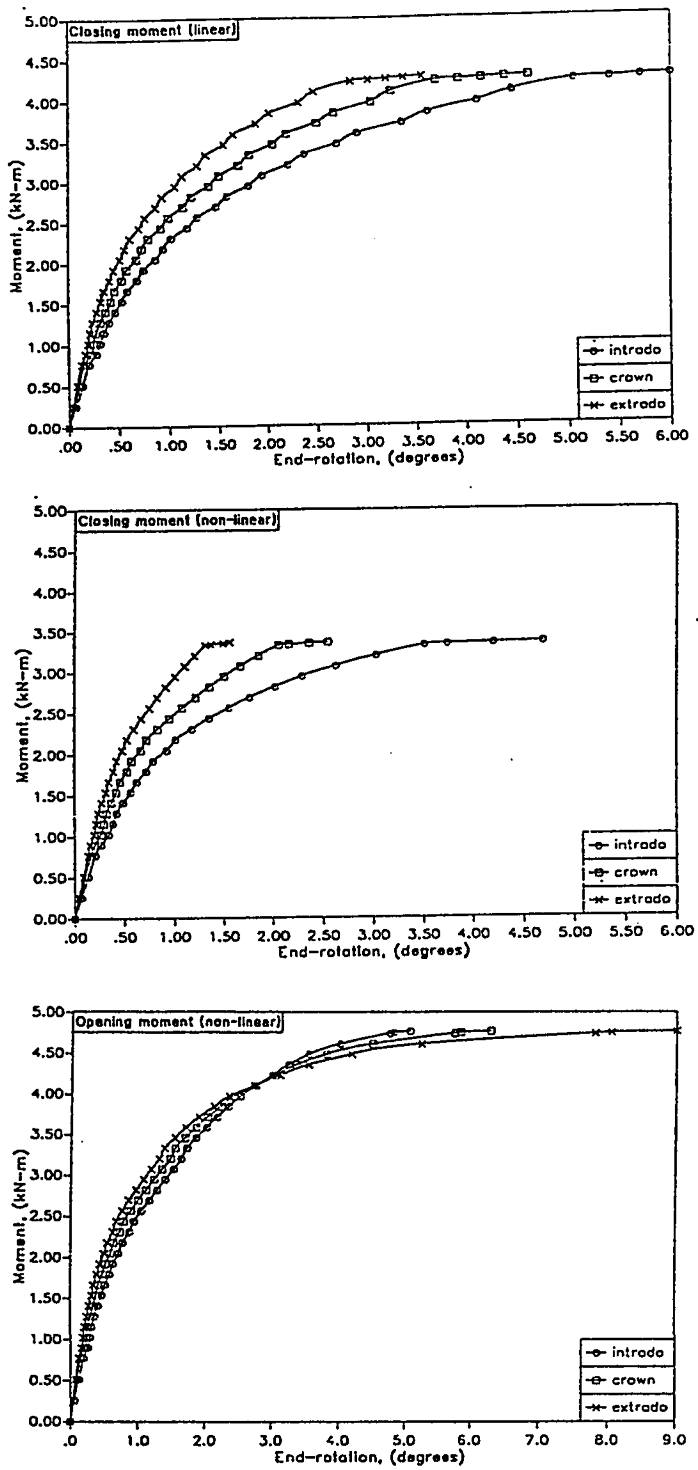

Figure 7.10: Effect of location and geometric nonlinearity on Moment End-rotation curves (a) geometrically linear closing-moment (b) geometrically nonlinear closing-moment (c) geometrically nonlinear opening-moment.

trado) of the mitre-edge has weakly influenced a decreased end-rotation (or geometrically nonlinear behavior) at the free-edge. The latter is also the case at the extrado of the free-edge and vice-versa for the intrado as exhibited in Fig. 7.10a and b. However in Fig. 7.10c the effect of the said influence is not that noticeable except towards collapse the extrado (now the compressed portion of the free-edge under opening-moment) accordingly showed an increased end-rotation (or more sensitivity to geometrically nonlinear behavior). The apparent similarity between the three-curves in Fig. 7.10c suggests that under opening moment, the mitre was somehow 'pulling' its stiffness together and therefore acted more like an integrated structure in a manner similar to that of the monolithic beam-type bending.

7.3.3.2.3 Deformation profiles The plots in Fig. 7.11 show the progress of displacement profiles along tha axes of the intrado ($\theta = 0^o$), the crown ($\theta = 90^o$), and the extrado ($\theta = 180^o$) for the indicated elasto-plastic geometrically nonlinear closing-moment histories. The curves for geometrically linear closing-moment are essentially of the same form. Also, except for the difference in sign, the case for the geometrically nonlinear opening-moment qualitatively showed similar line deformation profile and such the corresponding figures, although available, did not need to be shown.

When the mitre was subjected to in-plane closing-moment, the cross-section at the mitre-edge deforms elliptically and the major axis of the ellipse is perpendicular to the (vertical) plane of bending. i.e. the cross-section showed positive flattening. On the other hand, under opening-moment, it was observed that the cross section experienced negative flattening. In the latter case the major axis of the deformed cross-section would coincide with the (vertical) plane of bending. The growth of these deformation patterns, the so-called cross-section ovalizations, is illustrated in Fig. 7.12 for the closing-

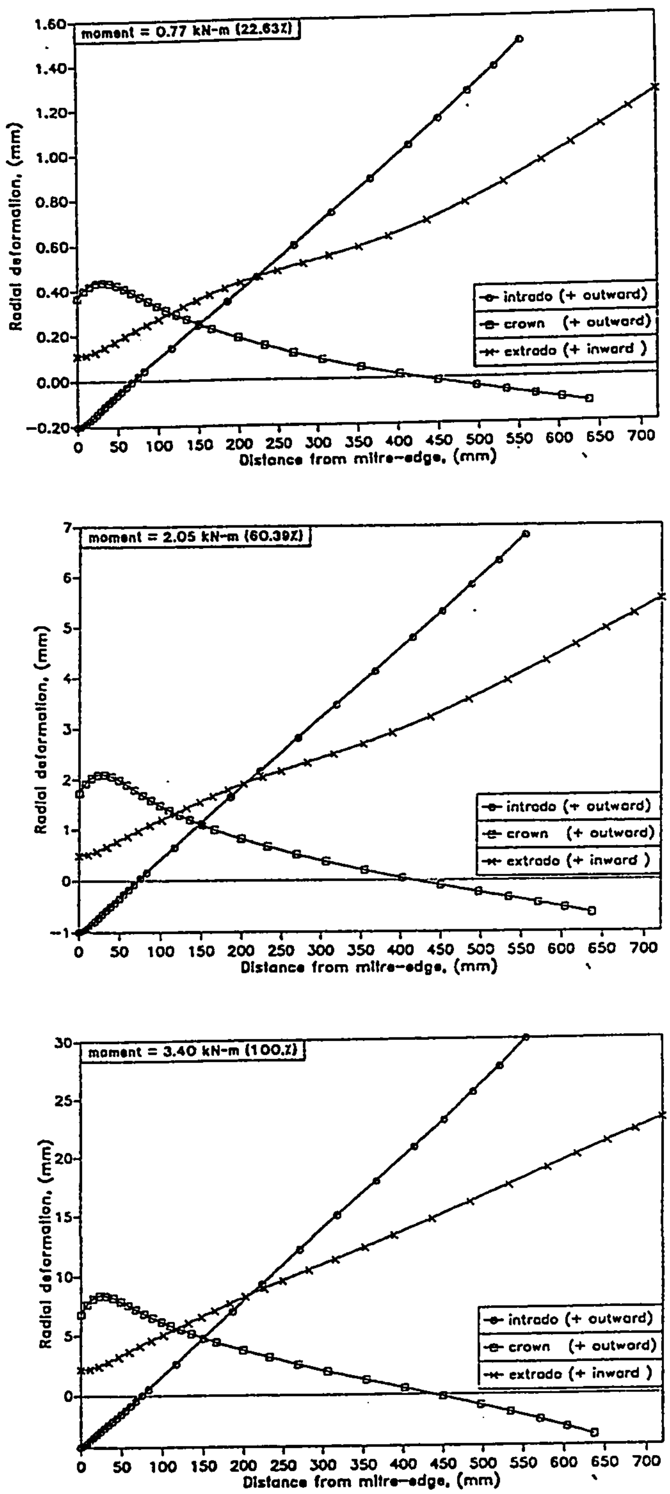

Figure 7.11: Displacement profiles along three mitre axes (elasto-plastic mitre analysis under bending). (a) at post yield (b) at gross yield (c) at collapse.

moment and Fig. 7.13 for the opening-moment.

Shown in Figs. 7.14 and 7.15 are the corresponding plots representing ovalization of the free-edge cross-section as it occurred for the indicated loading histories. In the case of closing-moment, Fig. 7.14, the free-edge cross-sectional ovalization behavior remained almost circular and only differed from the original circular cross-section by a vertical displacement which was offset downward. For the opening-moment, Fig. 7.15, the behavior is as for the closing-moments, except that the vertical offset was observed to be directed upward with respect to original undeformed circular cross-section at the free-edge. The ovalizations are not shown to scale but exaggerated in such a way that the maximum (radial) displacement is normalized to 40% of the plotted radius. The value of this maximum displacement is indicated in each of the ovalization plot by the small arrow which also illustrates the corresponding location. The value together with the load values would, in essence, serve to indicate the level of disparity between the various plots.

7.3.3.2.4 Plastification patterns The progress of plastic yielding of the entire mitre segment was assessed by examining the plastic strain values as given by **PLAMBS7** and was hence monitored at each gauss-point. For the closing-moment (nonlinear), Figs. 7.16 and 7.17 are therefore representative illustrations which respectively show perspective views of the inside and outside (gauss points or) surfaces of the single mitred bend according to the spread of plastic zones at the indicated load levels. Thus for the closing-moment, plasticity manifested at the mitre-edge and more specifically first in the inner and outer surfaces of the crown, then developed towards the middle of the thickness and the intrados and later the extrados. This sequence of plastification was seen to progress from the mitre-edge to the free-edge as the magnitude of the applied bending was increased to collapse.

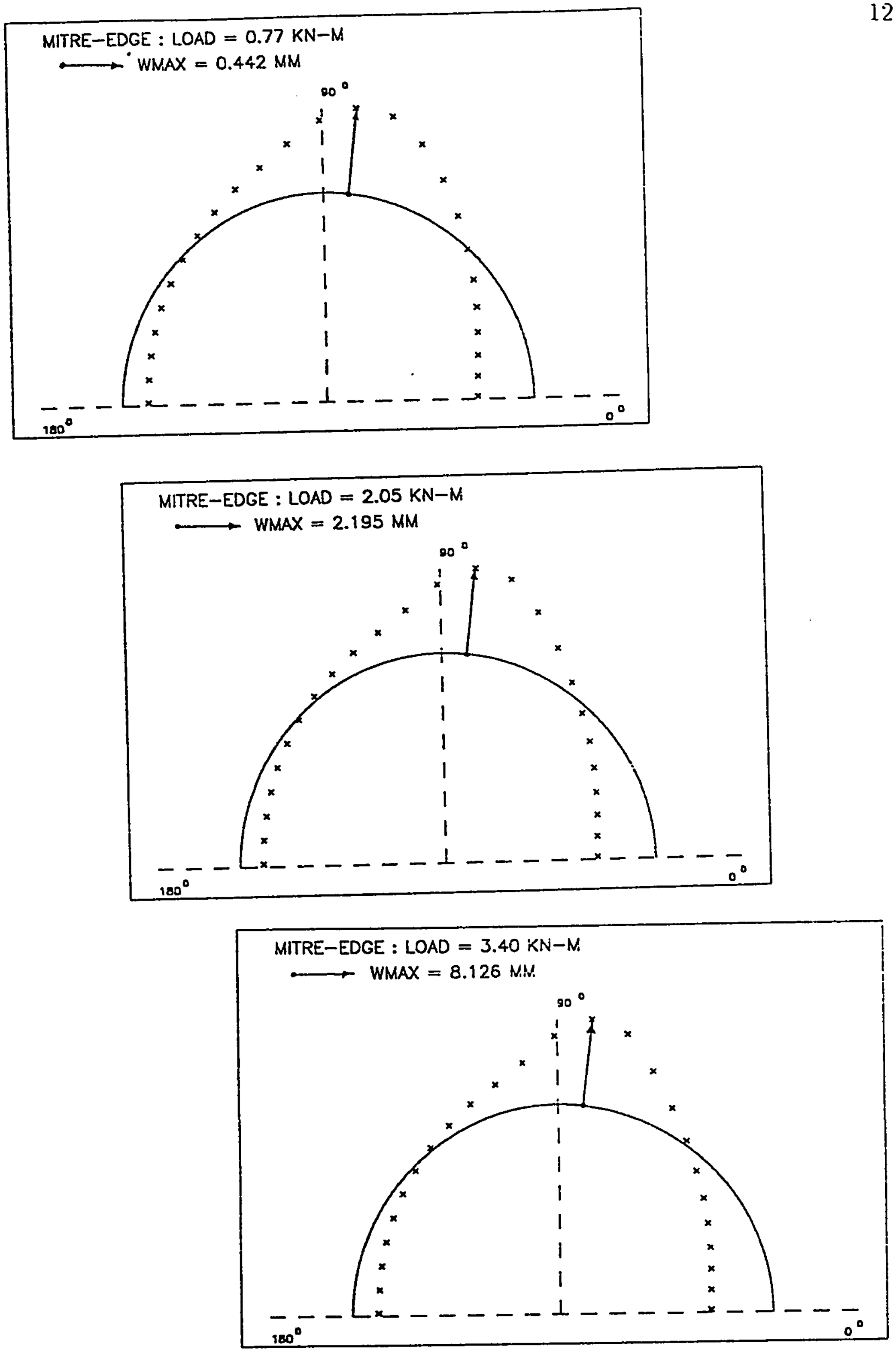

Figure 7.12: Cross-sectional ovalizations at mitre-edge: closing-moment (a) at first yield (b) at gross yield (c) at collapse.

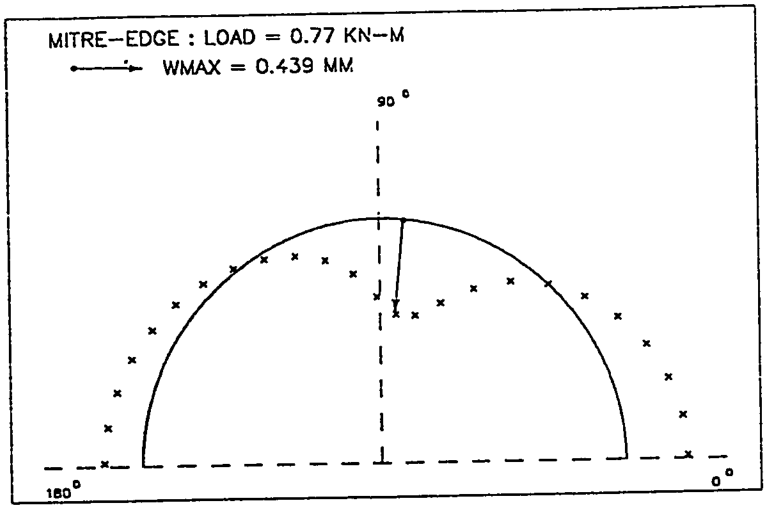

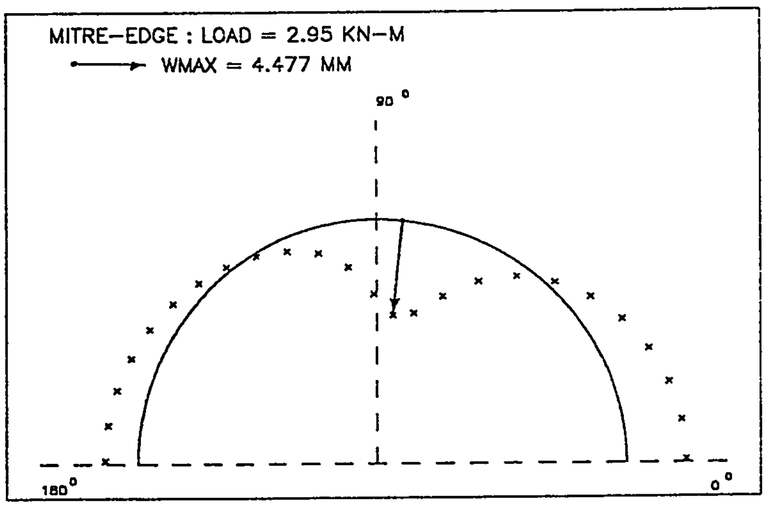

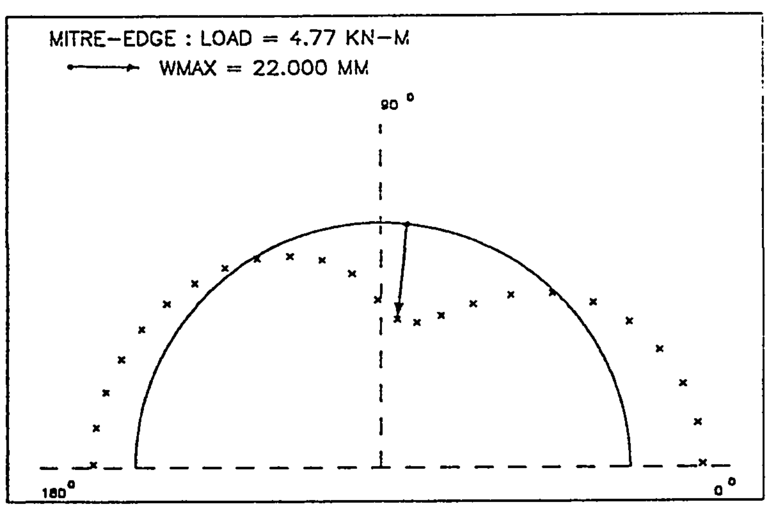

Figure 7.13: Cross-sectional ovalizations at mitre-edge: opening-moment (a) at post yield (b) at gross yield (c) at collapse.

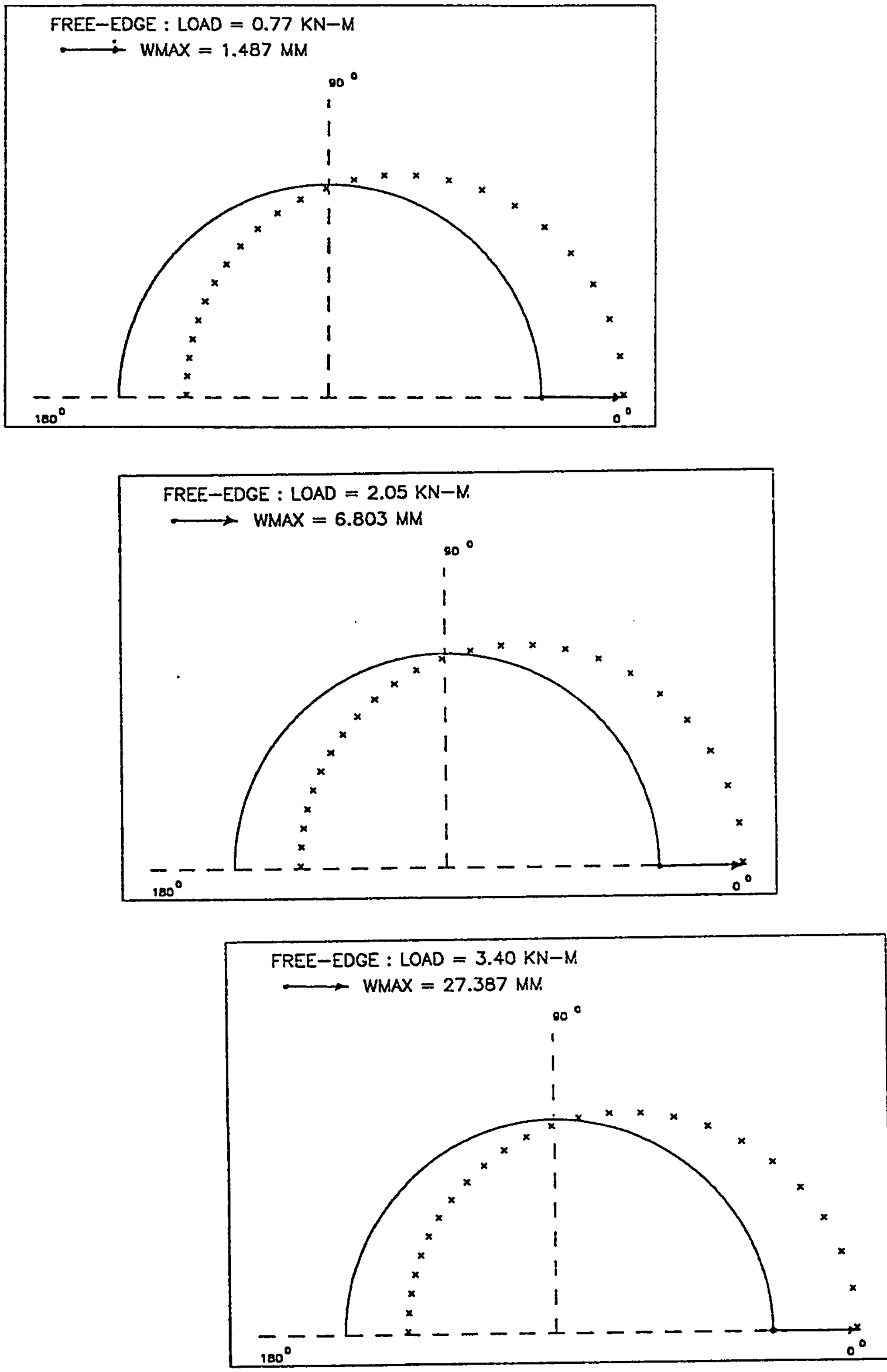

Figure 7.14: Cross-sectional ovalizations at free-edge: closing-moment (a) at first yield (b) at gross yield (c) at collapse.

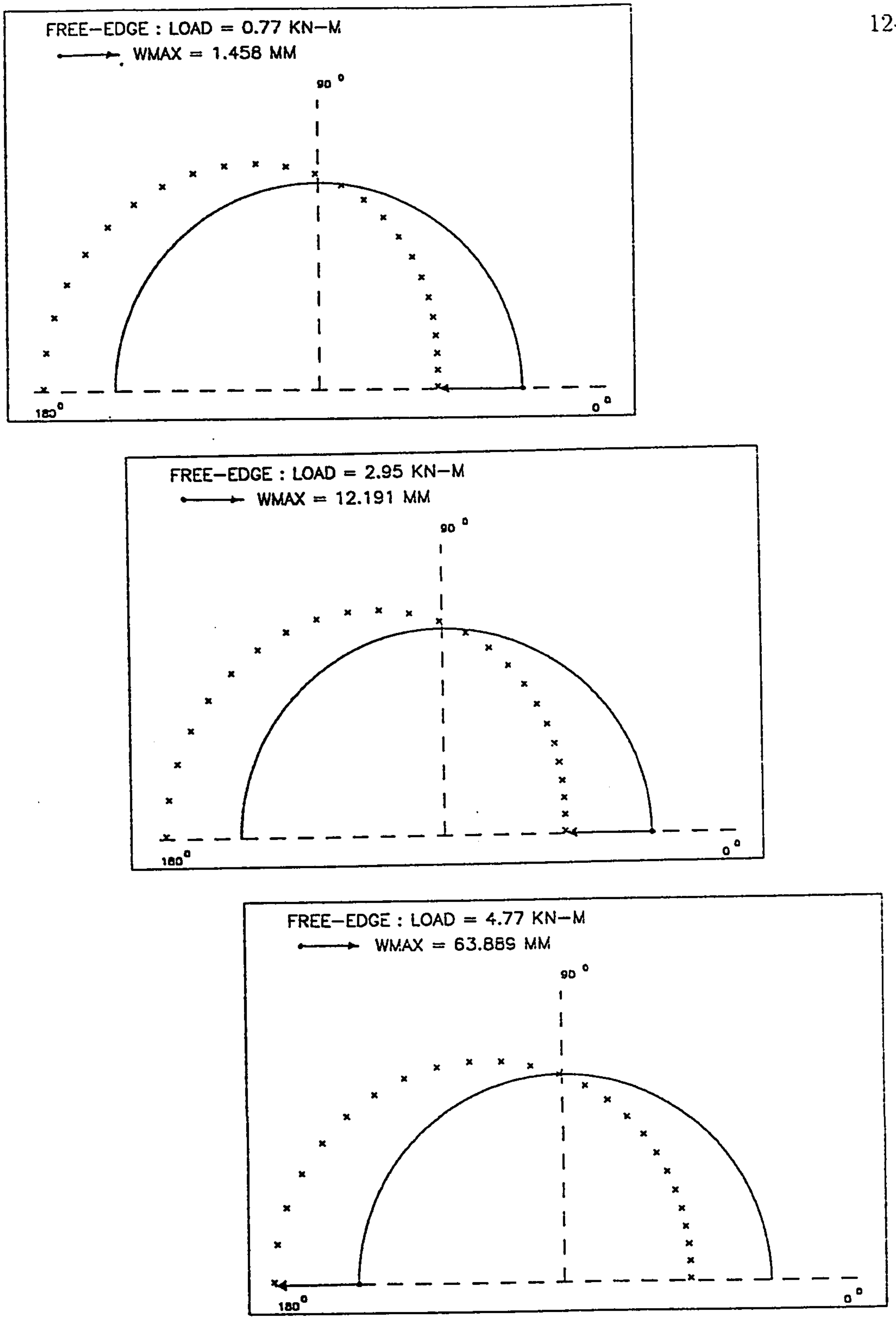

Figure 7.15: Cross-sectional ovalizations at free-edge: opening-moment (a) at post yield (b) at gross yield (c) at collapse.

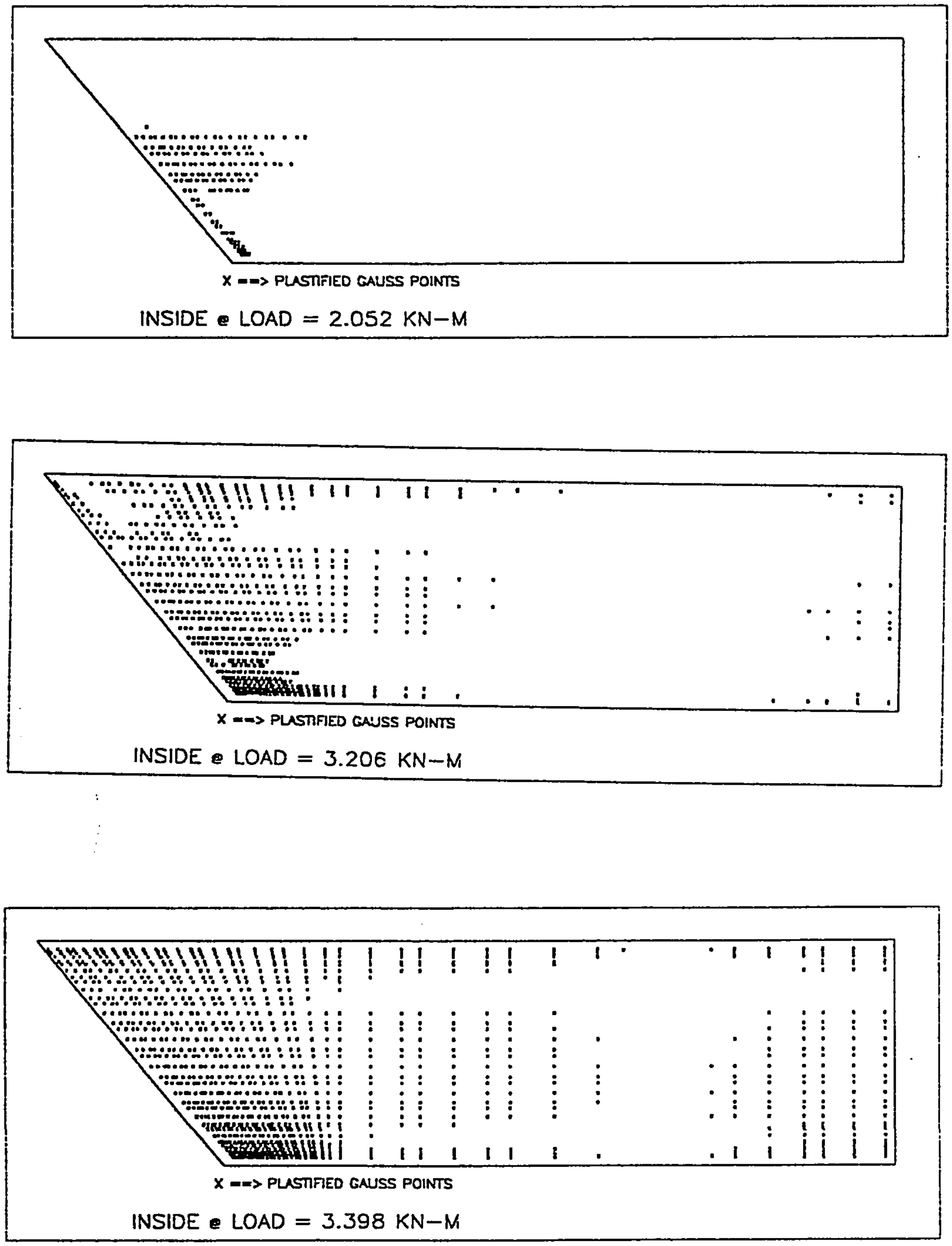

Figure 7.16: Spread of plastic zones at inside-surface under geometrically nonlinear closing-moment (a) at post yield (b) at gross yield (c) at collapse.

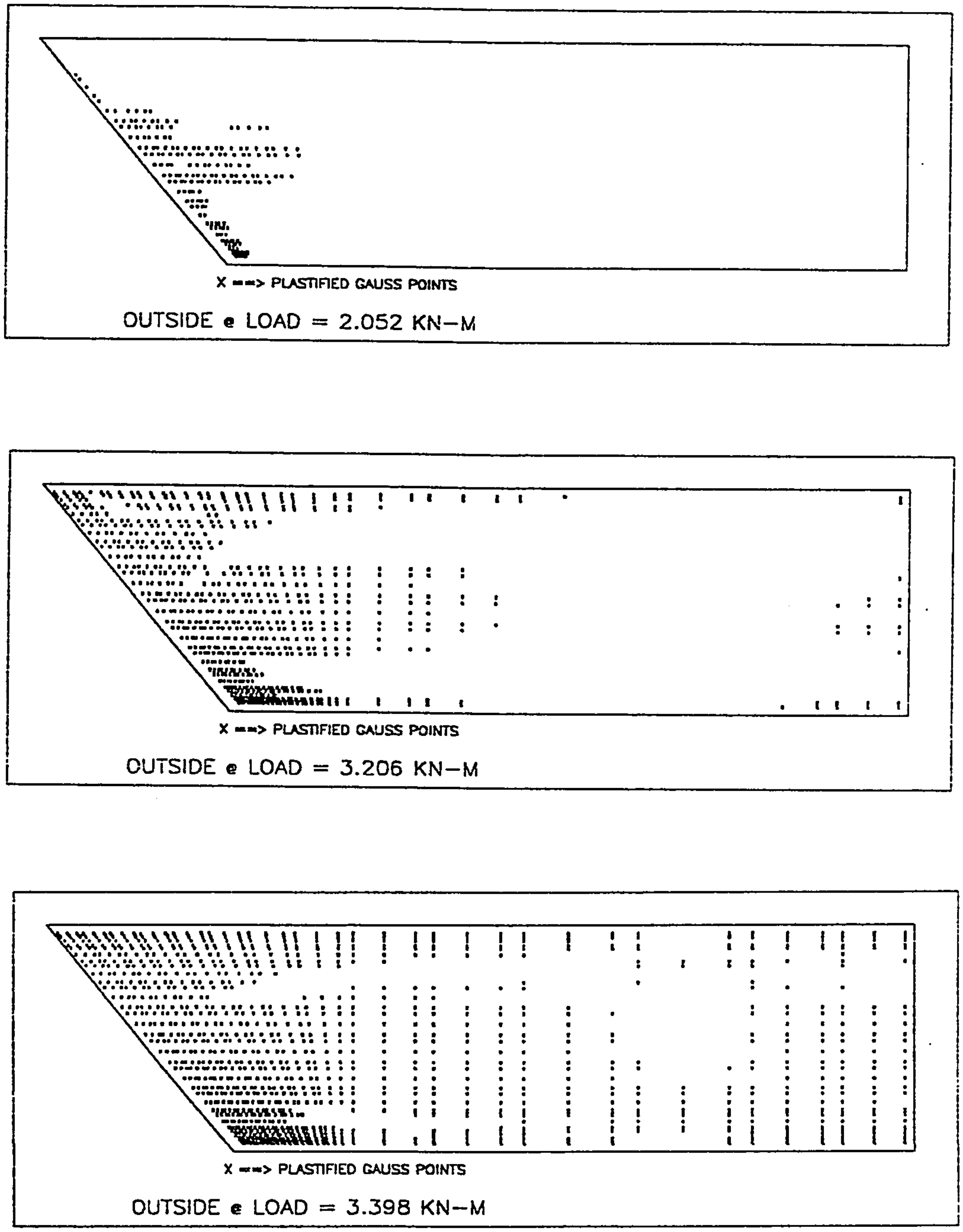

Figure 7.17: Spread of plastic zones at outside-surface under geometrically nonlinear closing-moment (a) at post yield (b) at gross yield (c) at collapse.

When compared to a straight pipe ($\alpha = 0$), or for that matter small mitre angle bend ($\alpha \leq 15^o$), the plastification behavior of this relatively large mitre angle bend ($\alpha = 45^o$) is seen to be quite contrary to what would be expected in the pipe situation. For straight pipes, the author in Ref. [57] has shown that the plastification sequence started at the intrados and extrados and then progressed towards the crown through the pipe thickness. However, by consideration of the simpler situation of elastic in-plane bending of the single mitred bend, the observed plastification trend for the elasto-plastic in-plane bending is consistent with the higher stress concentrations accrued to the crown of the mitre-edge in relation to that at the intrado and in turn the extrado as succinctly described by Fig. 7.6, (a and b). Accordingly, the growth of plastic zone from the crown towards the intrados is more rapid than that from the crown towards the extrados where the affinity to high stress ratios is in fact absent.

7.3.4 Study Problems

Having established the credibility of **PLAMBS7** based on comparative elastic and elasto-plastic problems for which there are comparative results, the present section employs **PLAMBS7** towards elastic and elasto-plastic problems for which corresponding results were not available from the surveyed literature. To allow extensive treatment, the analyses presented herein has been restricted to single mitred bends subjected to internal pressure only.

7.3.5 Study Survey I : Elasto-Plastic Mitres

In order to gain insight into practical situation concerning this category of mitres within the realm of the high pressure pipework industry, a study survey involving combinations of small/large mitre angles and thick/thin mitre thicknesses was conducted. Four different single mitred bend models

differing in their values of mitre angle α and radius to thickness ratio a/t (the so-called thinness ratio) were used for the study. The following dimensions and material properties are therefore common to the studied mitre models (a) Geometry: $a = 500mm$, $L = 2000mm$ (b) Material: $E = 30000MPa$, $\nu = 0.30$, $\sigma_y = 30MPa$, $\tau_y = 17.32MPa$, $H\prime = 303.3MPa$.

7.3.5.1 Geometric Categorization

As stated before, the specific details of the four models being studied were chosen to permit investigation of α and a/t effects on mitre response and hence the following categorization:

- **Category I** : Effect of increasing the thinness ratio (a/t)

  model 1 : $\alpha = 15^o$, $a/t = 20$

  model 2 : $\alpha = 15^o$, $a/t = 50$

- **Category II** : Effect of increasing the mitre angle (α)

  model 3 : $\alpha = 45^o$, $a/t = 20$

  model 4 : $\alpha = 45^o$, $a/t = 50$

Thus, mitre models 1 and 3 are, respectively. small and large mitre-angle bends of thick-walled ($t = 25mm$) construction. and so are mitre models 2 and 4 except that they are of thin-walled ($t = 10mm$) construction.

In the results to be presented, selective integration (3x2) was used with the extended layered model (3Lx3, i.e. three separate but fictitious layers each with three gauss-points) and the Lagrange elements. The mesh layout utilized was the basic mesh model A (with 108 elements). The tangential stifness method in which reformulation of the stiffness is made in the second

iteration of each load increment (option **NALGO** = 4 in **PLAMBS7**) was used for the current analysis.

7.3.5.2 Load-Deformation Curves

Figure 7.18 compares results of the analysis for load versus displacements corresponding to the four mitre models. The plotted displacements are radial ones monitored at a key location of the mitre models. The location is the intrado of the mitre-edge since it is precisely the hot-spot location for single mitred bend subjected to internal pressure.

Judging from Fig. 7.18, the most significant difference in terms of early departure from linear material behavior can be seen to separate along mitre models of similar thinness-ratio (a/t) rather than along mitre models of similar mitre angle α—the latter being the expectation when, hitherto, the mitre models were categorized as categories I and II before. Hence in line with this recent trend as well as for convenience of further discussion, the mitre models would be referred in accordance with the following re-groupings:

- **Group I** : Thick mitres ($a/t = 20,\ t = 25mm$)

  model 1 : $\alpha = 15^o$

  model 3 : $\alpha = 45^o$

- **Group II** : Thin mitres ($a/t = 50,\ t = 10mm$)

  model 2 : $\alpha = 15^o$

  model 4 : $\alpha = 45^o$

Starting with the group I models (thick mitre models 1 and 3), the behavior for model 1 (large mitre angle: $\alpha = 45^o$) showed early tendency to plastic response in comparison to model 3 (small mitre angle; $\alpha = 15^o$). However,

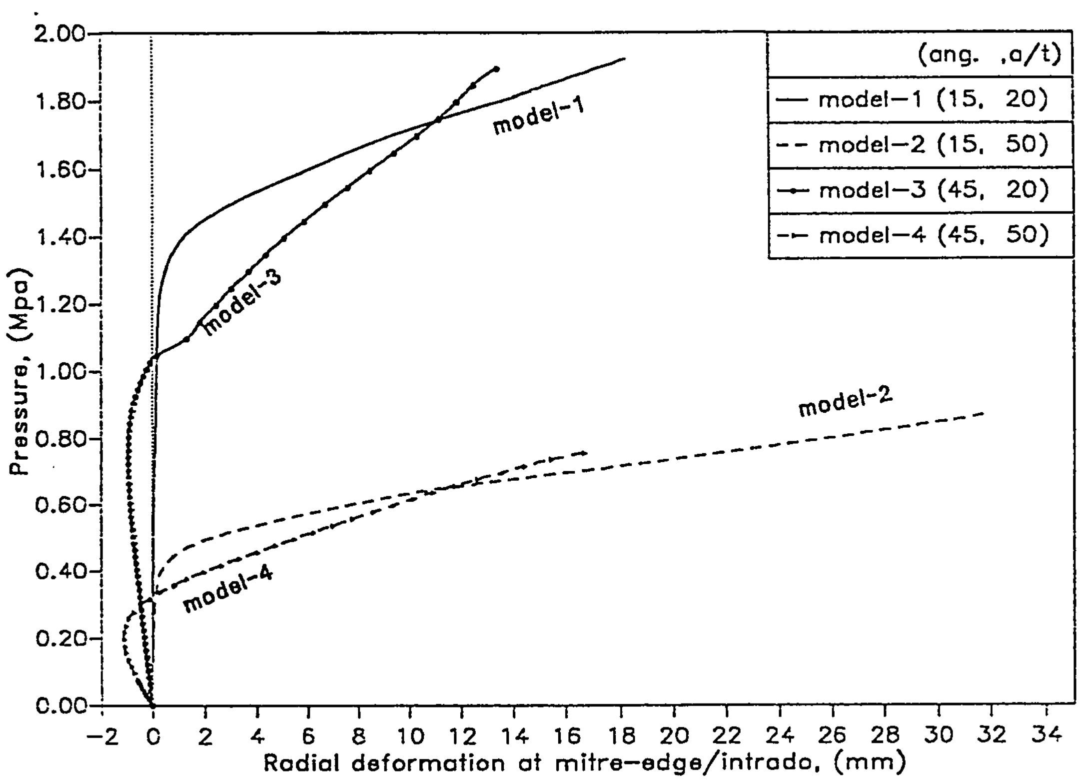

Figure 7.18: Load displacement curves of four mitre models.

both models 1 and 3 exhibit response that can be described as rigid-linearly plastic behavior except that model 3 ($\alpha = 45^o$) tend to show negative (radially inward) displacement response in the elastic range. Relative to model 1 ($\alpha = 15^o$), the strain hardening characteristics for model3 ($\alpha = 45^o$) occurred at a higher (tangent) slope and, accordingly, complete collapse of the model 3 was at a reduced deformation level although the complete collapse load is very much the same for both models. An obvious deduction out of this trend is that as far as the mitre-edge cross-section is concerned model 3 ($\alpha = 45^o$) is somewhat stiffer (i.e. less flexible) than model 1 ($\alpha = 15^o$). This deduction is opposite to that would occur if the respective mitre models were to be subjected to in-plane bending. Since the suggested increased in stiffness in model 3 ($\alpha = 45^o$) is akin to saying that further increase in deflections are smaller and hence stresses would, in fact, be larger than could be obtained in model 1 ($\alpha = 15^o$), the deduction is not irrelevant, however. The foregoing patterns are also quite consistent and conform to observations based on stress results obtained by consideration of the effect of increasing the mitre angle (α) during an elastic experimental study in Ref. [6]. Hence, not surprisingly, the negative displacement showed by model 3 ($\alpha = 45^o$) in the elastic range is also of corresponding behavior to that observed in Ref. [6] which reports that a change in sign for hoop bending stress at $\theta = 0^o$ (intrado) has resulted in experimentally tested mitre-models whose value of α is greater than about 37.5^o. Also from Ref. [6], it is interesting to note that contrary to the case of small mitre angle ($\alpha = 15^o$) bends, theoretical predictions were reported to fall below experimental values, with increasing mitre angle (α). In particular, the change in sign for the hoop stress, which is akin to the change in sign for the (radial) displacement and unfailingly picked up by **PLAMBS7** for the mitre model 3 as shown in Fig. 7.18, was faillingly not picked up by the

theory.

Thus far for group I models, but a closer look at Fig. 7.18 would indicate that the response behavior for group II models (models 2 and 4) is a precise replica to that for group I models (models 1 and 3 respectively). As was noticed earlier, the only difference is that of a sharp reduction of peak loads (first-yield, gross-yield, complete-collapse, etc.) in group II (thin mitres) in comparison to group I (thick mitres). As such, under pressure loading, the profound effect of increased thinness ratio (a/t) in reducing the load carrying capacity of the studied mitre models is more than can be attributed to the effect of increased mitre angle (α). Also for the pressure loading, increasing the mitre angle (α) has the effect akin to reduced mitre-edge flexibility and hence increased stresses for a given thinness ratio (a/t).

7.3.5.3 Plastic Collapse Loads

Since collapse loads are of interest in this study, the present investigation based on the four mitre models was considered most relevant in providing a perspective insight for the determination of limit loads which in the case of the pressure loading are termed burst pressures.

7.3.5.3.1 Theoretical idealizations Burst pressure particularly provides an important basis for the design of high pressure components such as single mitred bends within the framework of limit analysis [49, 3, 56]. Theoretical idealization for the analysis is simply made since it is strictly based on elastic-perfectly plastic or rigid-perfectly plastic material models. A sudden discontinuity, not quite in agreement with tested materials, in the load-displacement curve is also normally assumed [54]. Owing to this the simple limit analysis only gives loads which are deemed to be complete collapse load without accounting for the effect of strain hardening.

However, with the load-displacement response of Fig. 7.18 that traced the true material behavior of the studied mitre models, the present analysis would permit a more complete solution for their burst pressures that will be more in agreement with experimentally observed behavior. Also consistent with experimental behavior, the strain hardening nature coupled with geometrical nonlinearities characterized by the load-displacement curves in Fig. 7.18 will nonetheless not permit a single estimate to the collapse load corresponding to each of the four models under investigation. That is to asy, unlike the limit analysis, the actual limit load or burst pressure is not a unique quantity.

7.3.5.3.2 Collapse load definitions Various experimental investigations [56, 54, 49] have resulted in a number of limit load definitions that could provide a reasonable estimate to the perceived burst pressures for the analyzed mitred bends. Such definitions rely on the basic appearance of the load-displacement curve which essentially comprise a straight linear part (elastic regime), a transition region (at the gross yield where the behavior changes from elastic to mainly plastic) and a higher elasto-plastic region (which is approximately straight but of a much lower gradient than the elastic part). This description is in line with Ref. [56], but the following alternative techniques for estimating collapse load follows similar definitions cited in the said reference and Ref. [54]:

1) Gross yield : Load (P_g) at departure from linear elastic behavior.

2) Tangent method : Load(P_t) corresponding to the intersection between the extended elastic and plastic line.

3) Complete collapse : Load(P_f) at complete collapse, i.e. at the end of the plastic part.

4) Offset method : Load(P_δ) corresponding to a permanent displacement equal to twice the displacement at the end of the elastic part.

5) Angle method : Load(P_γ) at the intersection of the load-displacement curve and a line whose angle γ is twice the initial elastic slope.

Apparently the five methods stated above provide definition for the burst pressure that would cover a wide range of values. Hence the definitions are only approximate. Therefore, in addition to load corresponding to the first yield (P_y) which, of course, is not discernible from the load-displacement curve, the present study would consider estimating the burst pressure based solely on the first three methods namely: the gross yield (P_g), the tangent method (P_t), and the complete collapse (P_f). Without loss of generality, the imposed restriction was intended to permit smoother flow of ideas in relation to a development of the so-called failure-load or burst-pressure diagrams in the following subparagraph.

7.3.5.3.3 Burst-pressure diagrams An attempt was made to provide a convenient but comparative representation of the variation in burst-pressures or limit-loads for the four studied mitre models under consideration. Moreover, the four ear-marked limit-load definitions corresponding to P_y, P_g, P_t, and P_f in relation to Fig. 7.18 have been studied for each of the four mitre models. In line with the mitre models groupings (not categorization), the various burst-pressure estimates considering the four selected definitions (P_y, P_g, P_t, and P_f) and obtained from the corresponding curves in Fig. 7.18 are reported in Table 7.1a. To form a basis of comparison, the obtained burst pressures were sought to be normalized with respect to burst pressure that would occur in a straight pipe ($\alpha = 0°$) but having the same basic dimensions and yield parameters as that of the respective groupings. For this instance, it

Burst Pressure(MPa)	Group I			Group II		
	0^o	15^o	45^o	0^o	15^o	45^o
P_y	1.50	0.90	0.245	0.60	0.24	0.070
P_g	1.50	1.11	0.700	0.60	0.39	0.160
P_t	1.50	1.42	0.950	0.60	0.47	0.260
P_f	1.50	1.92	1.895	0.60	0.87	0.757

Normalized Burst Pressure	Group I			Group II		
	0^o	15^o	45^o	0^o	15^o	45^o
P_y	1.000	0.600	0.163	1.000	0.400	0.117
P_g	1.000	0.737	0.467	1.000	0.650	0.267
P_t	1.000	0.947	0.633	1.000	0.783	0.433
P_f	1.000	1.280	1.263	1.000	1.450	1.262

Table 7.1: Burst pressures for group I and II mitre models (a) estimated values (b) normalized values.

was assumed that the pipe material would obey theoretical limit analysis concept based on the simple rigid-perfectly plastic material model. Hence by assuming further that the relation $\sigma_{max} = pa/t$ still holds for such a pipe, the pipe burst-pressure is then simply:

$$P_p = \sigma_y(a/t) \tag{7.3}$$

and accordingly $P_y = P_g = P_t = P_f = P_p$ for the idealized pipe.

Normalization of group I and II mitre burst-pressures in Table 7.1a with respect to cylinder respectively will give Table 7.1b. It should be noted that in Table 7.1b, the pipe burst pressures were included in order to allow acceptable extrapolation to small mitre angles, with $\alpha < 15^o$.

Remarkably, the curves in Fig. 7.19a and b provide at a glance the effect of the increased mitre angle. In relation to the a/t ratio effect, the effect of increased mitred angle had not been that noticeable. The relevance of the burst-pressure diagrams in therefore exposing this and similar salient features between the four studied models can not be overemphasized.

To allow direct comparison for the effect of increased thinness ratio a/t (Fig. 7.19a to Fig. 7.19b), the plots in Fig. 7.19b have been further factored by 2.5. The latter factor essentially represents the departure of group II mitre burst-pressures if they were to be normalized by pipe-I burst-pressure, instead of pipe-II burst-pressure.

7.3.5.4 Deformation Profiles

Figure 7.20 shows the displacement profiles along the axis of the intrado ($\theta = 0^o$), the crown ($\theta = 90^o$). and the extrado ($\theta = 180^o$) for the mitre model 1 ($\alpha = 15^o, a/t = 20$). It should be noted that the indicated load level in Fig. 7.20a, b, and c are respectively for load estimates corresponding to P_y (first-yield), P_t (tangent-method), and P_f (complete-collapse). Also,

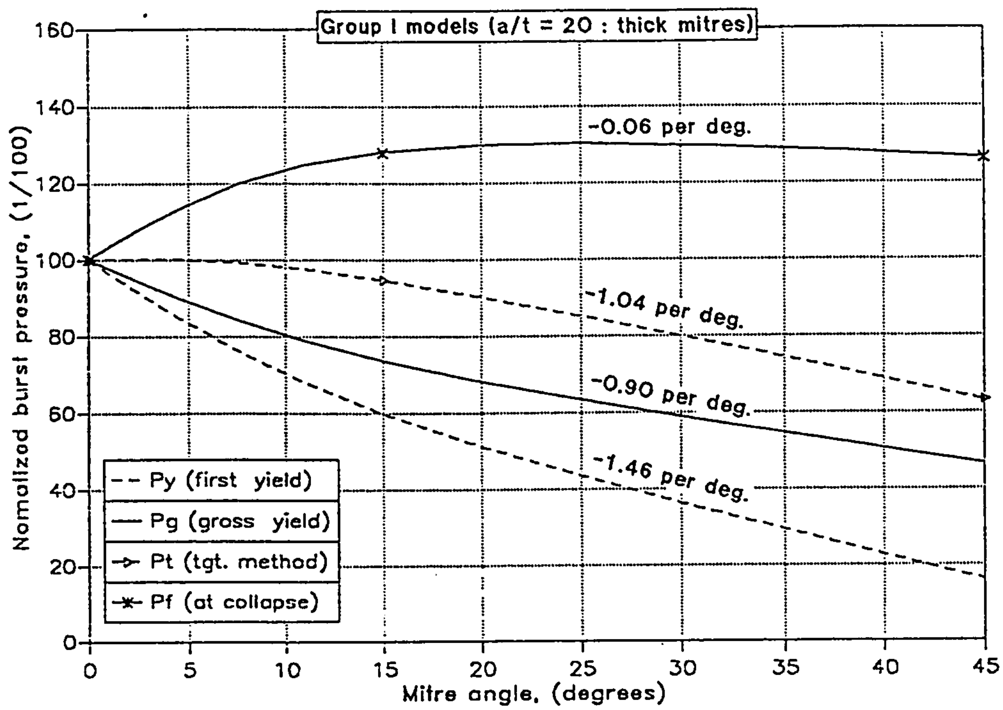

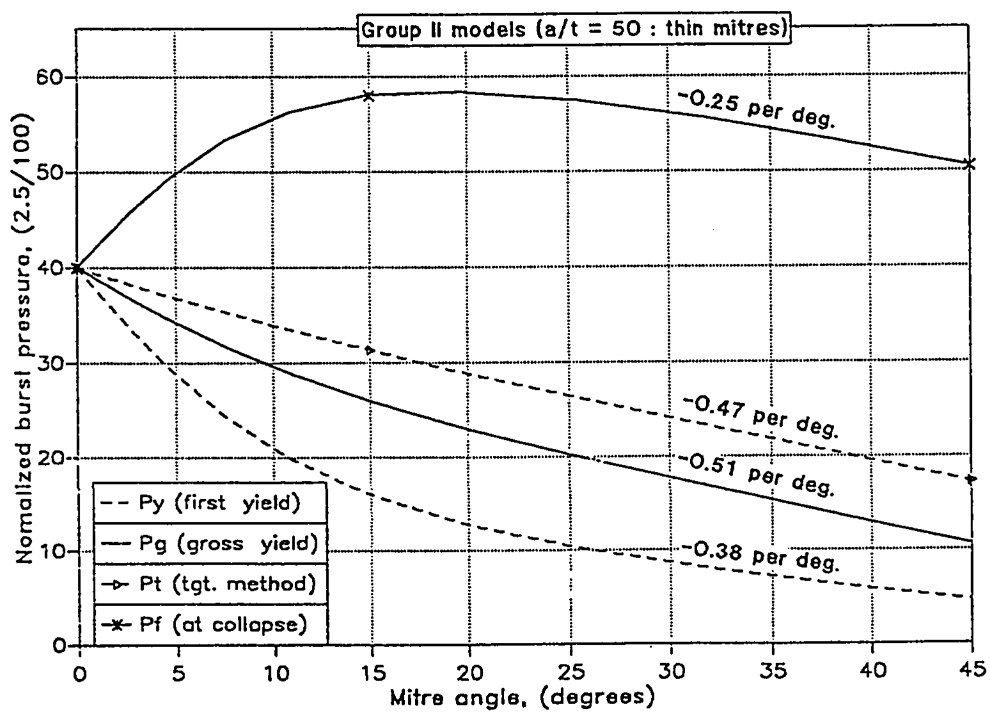

Figure 7.19: Burst pressure diagrams (a) group I (thick) mitre models (b) group II (thin) mitre models.

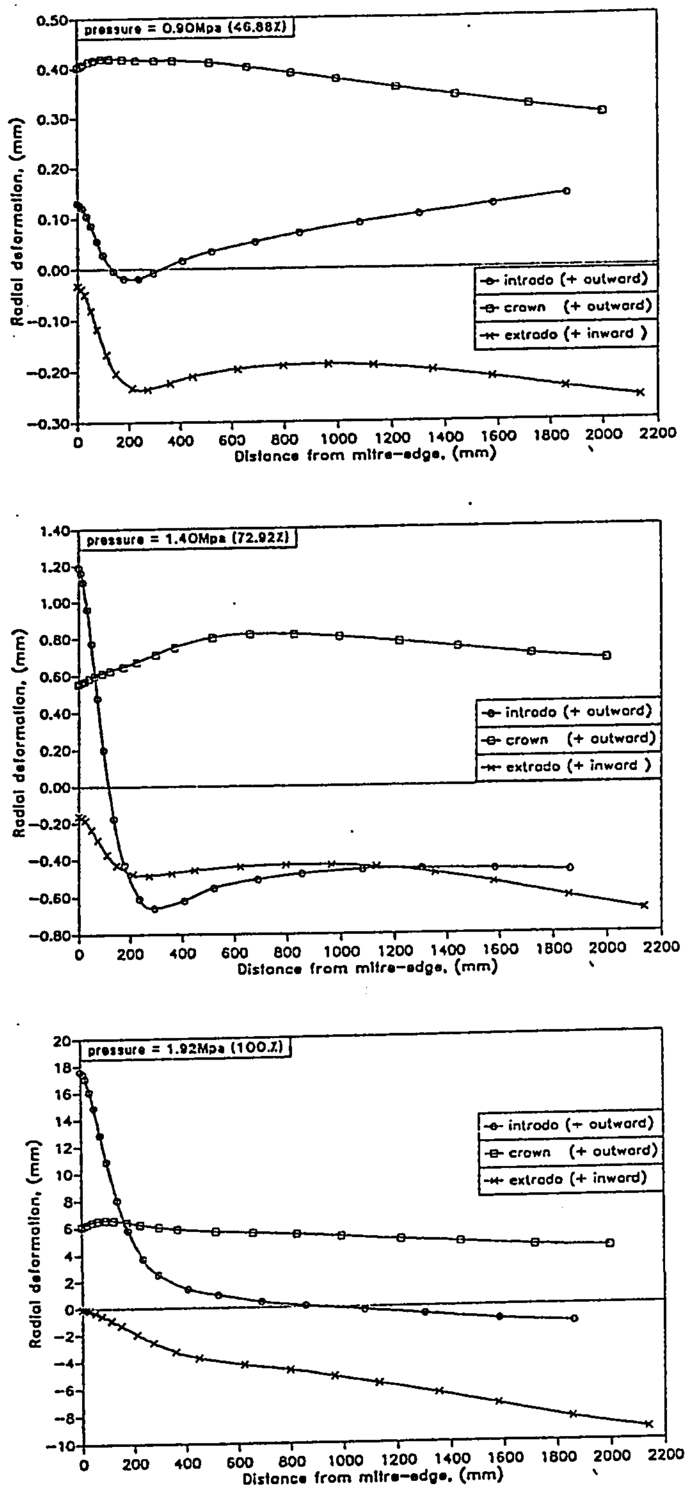

Figure 7.20: Displacement profiles along three mitre axes (a) at post yield pressure (b) at gross yield pressure (c) at collapse pressure.

the curve for the crown is a direct indicator to the change in radius (rather than diameter) along the axis $\theta = 90^o$ of the mitred bend. The deformed profile at the crown is seen to show outward (radial) change and this occured consistently across the three internal pressure load levels. It is also somewhat uniformly occurring from the mitre-edge to the free-edge of the single mitred bend.

The cross-sectional changes in diameter (or ovalization) at sections around the mitre-edge and the free-edge of the single mitred bend are respectively demonstrated in Figs. 7.21 and 7.22. They correspond to the same load histories as those shown in Fig. 7.20. Recalling earlier statement, the arrow illustration in each of the ovalization plots is an indication of the location of the maximum radial displacement whose value is also indicated in the corresponding plots. For ovalization around the mitre-edge cross-section, Fig. 7.21, an observed tendency is that as the load level was increased, the location of the maximum (radial) displacement was shifting from a point around the crown ($\theta = 90^o$) to a point around the intrado ($\theta = 0^o$). The increased displacement with load at the intrado is an apparent indication of considerable relief in hoop bending stress at the intrado compared to the extrado which is consistent with observed stress redistribution or plastification sequence that will be presented next.

7.3.5.5 Plastification Patterns

The spread of plastic zones for the mitre model 1 ($\alpha = 15^o$, $a/t = 20$) was also monitored at gauss-points cloosest to the inside and outside surfaces of this internally pressurized small mitre-angle, moderately thick-walled single mitred bend. Results for the plastification growth are illustrated in Figs. 7.23 and 7.24. The figures show the perspective view of the studied model in

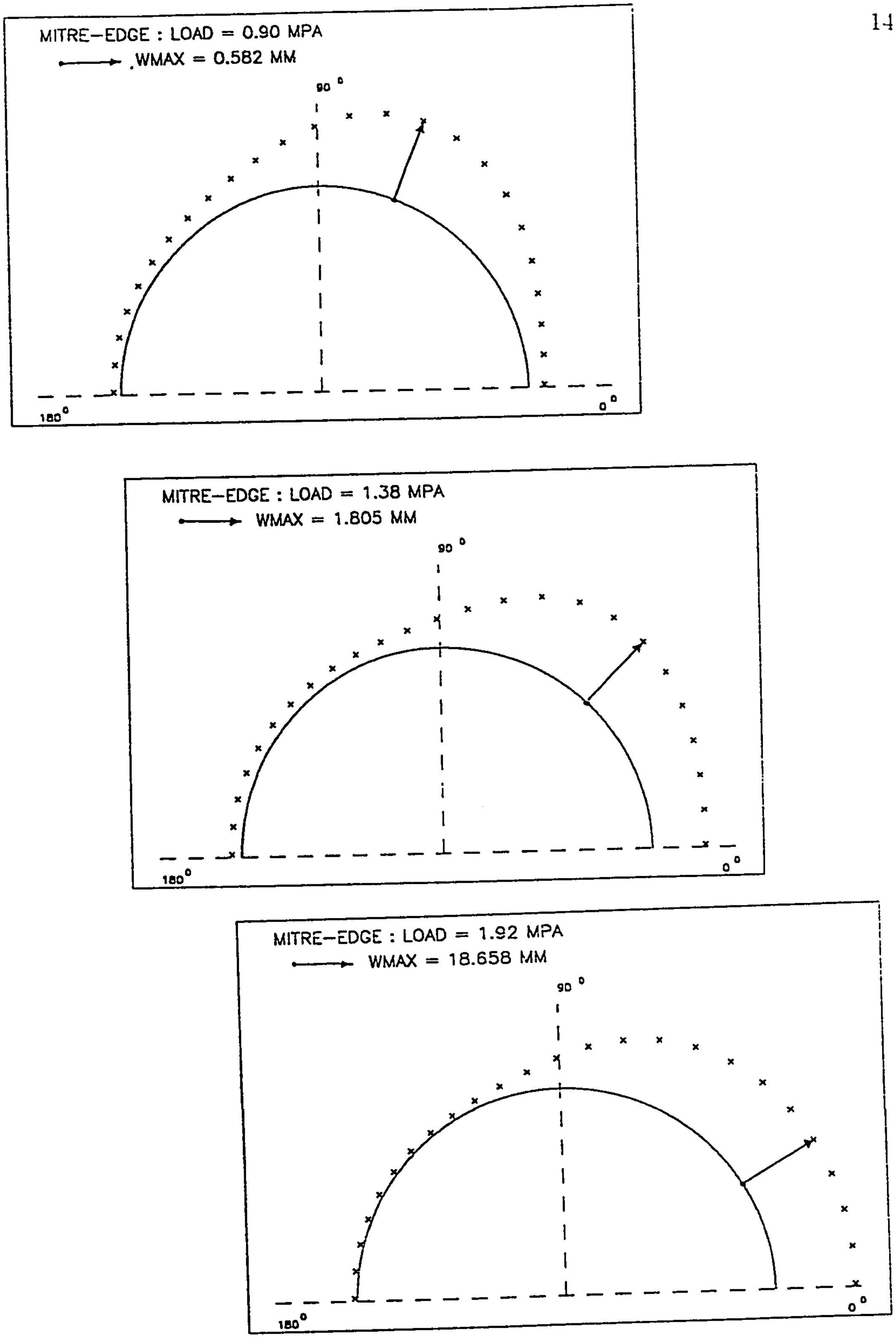

Figure 7.21: Cross-sectional ovalizations at mitre-edge (a) at first yield pressure (b) at gross yield pressure (c) at collapse pressure.

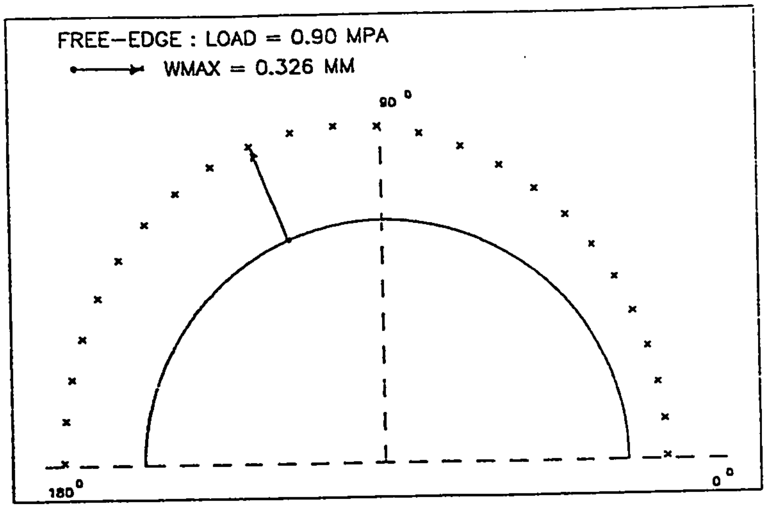

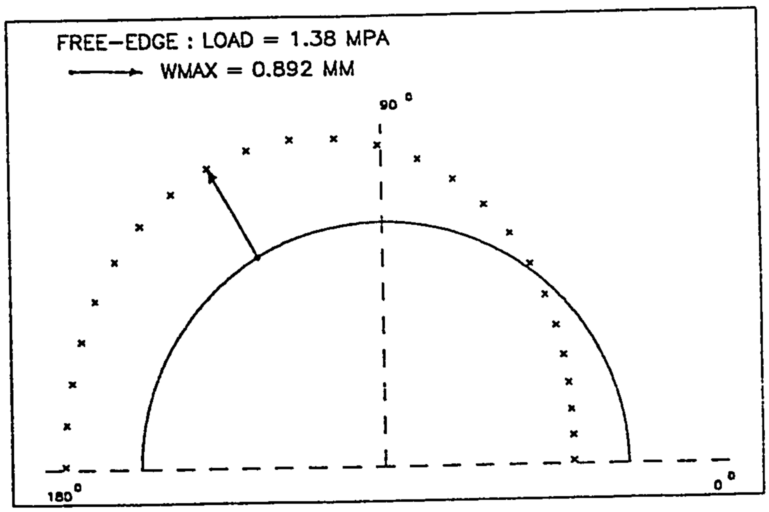

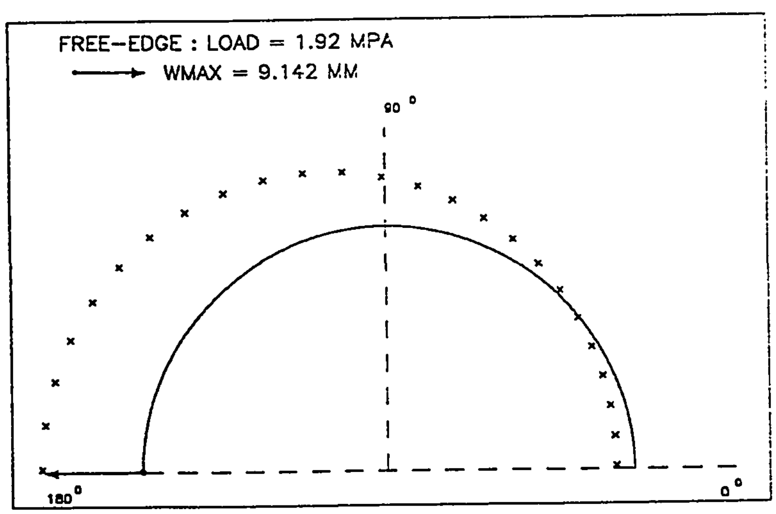

Figure 7.22: Cross-sectional ovalizations at free-edge (a) at first yield pressure (b) at gross yield pressure (c) at collapse pressure.

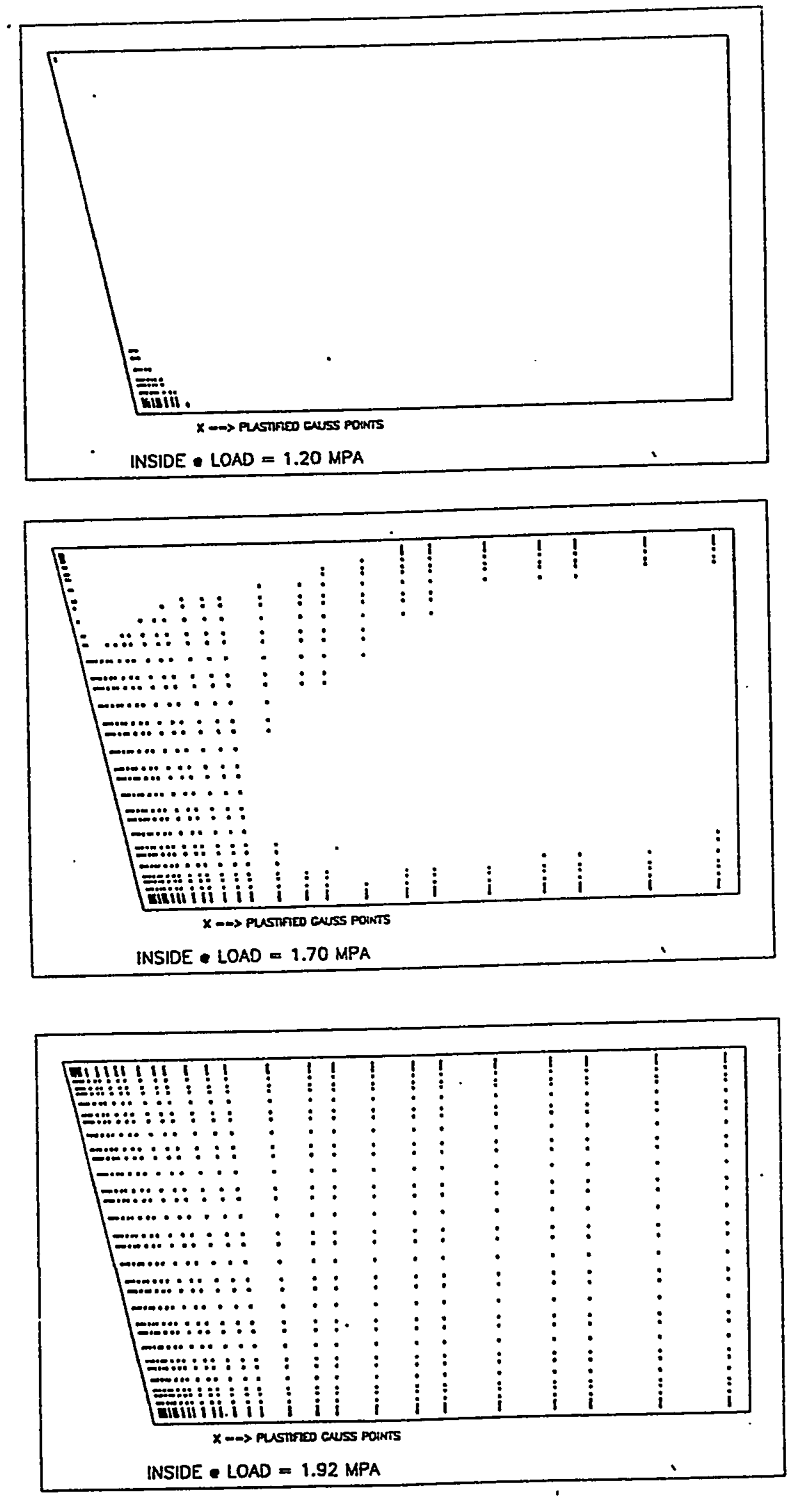

Figure 7.23: Spread of plastic zones at inside-surface (a) at post yield pressure (b) at gross yield pressure (c) at collapse pressure.

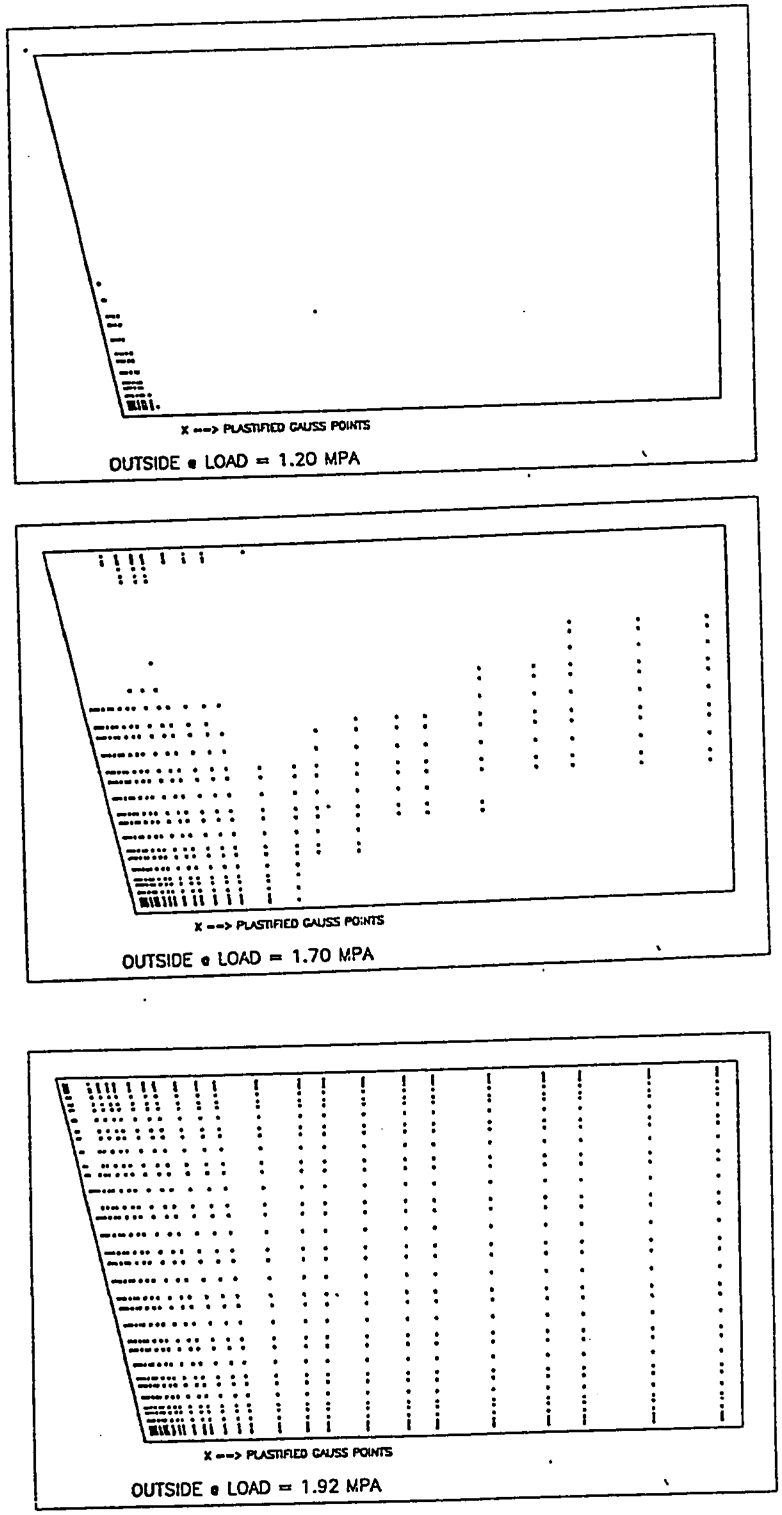

Figure 7.24: Spread of plastic zones at outside-surface (a) at post yield pressure (b) at gross yield pressure (c) at collapse pressure.

which each gauss-point is identified as either plastified or not for both the inside and outside mitre surfaces corresponding to three load levels, including one load level at collapse.

Cross examination of the plots in Fig. 7.23 shows that for the inside surface of the mitre plasticity appeared first at the intrado and then at the extrado with the crown later picking up some plasticity for location around the mitred-edge. As the load level was increased, the plastification has progressed from the mitred-edge to the free-edge but apparently along the extrado axis and the intrado axis before the crown was yet able to pick up for load levels near collapse. This behavior is contrary to the in-plane bending situation in which the crown was dominantly the hot-spot region for plastification spread, both hoop direction-wise and axial direction-wise. On the other hand, except for the occurrence of first yield at the intrado, and the complete plastification at collapse, the behavior for the outside surface in Fig. 7.24 is somewhat opposite to that for the inside surface in Fig. 7.23. This is more so in terms of the plastification growth from the mitred-edge to the free-edge. At collapse both the inside and outside surfaces (Figs. 7.23 and 7.24) showed persistent spots of elastic core at a location close to the extrado side of the mitre-edge.

7.3.6 Study Survey II : Elastic-Anisotropic Mitres

The finite element computer program **PLAMBS7** has also been employed in the elastic analysis of single mitred bends with anisotropic construction. The type of anisotropy assumed is that composing of anistropic material typical of metal matrix.

7.3.6.1 Geometry and Material Specification

In line with earlier assertion, the numerical examples for the present anisotropic problems are also confined to internal pressure only. The geometric dimensions utilized here are the same as those used for the first comparison problem in section 7.3.2 ($\alpha = 15^o$, $t = 2.5mm$, $a = 50.8mm$, and $L = 216.8mm$)

For the anisotropic analysis, two material types typical of advanced fibre-reinforced composites [127, 128] were used. The relevant mechanical properties as sourced from Ref. [129] are given as follows:

	E Glass-epoxy **(material I)**	T300/5208 Graphite-epoxy **(material II)**
E_1	$60700MPa$	$153000MPa$
E_1/E_2	2.44	14.05
G_{12}/E_2	0.48	0.51
G_{13}/E_2	0.20	0.40
ν_{12}	0.23	0.30

The materials are assumed to be transversely isotropic such that $G_{23} = G_{13}$ and $\nu_{21} = \nu_{12}$.

As for all internal pressure situations, computations were carried out using mesh model A (108 elements). Selective integration (3x2) and the simple layered model (1-point rule) were respectively used for the in-plane and across-the-thickness integrations. To allow adequate flexibility for material stacking architecture, Fig. 7.25, the mitre wall-thickness was divided into eight separate layers. The layers are assumed to be perfectly bonded at interfaces.

The nomenclature for the employed stacking sequence is shown in Fig. 7.25. It should be noted that for anisotropic situations, the layer interfaces are real

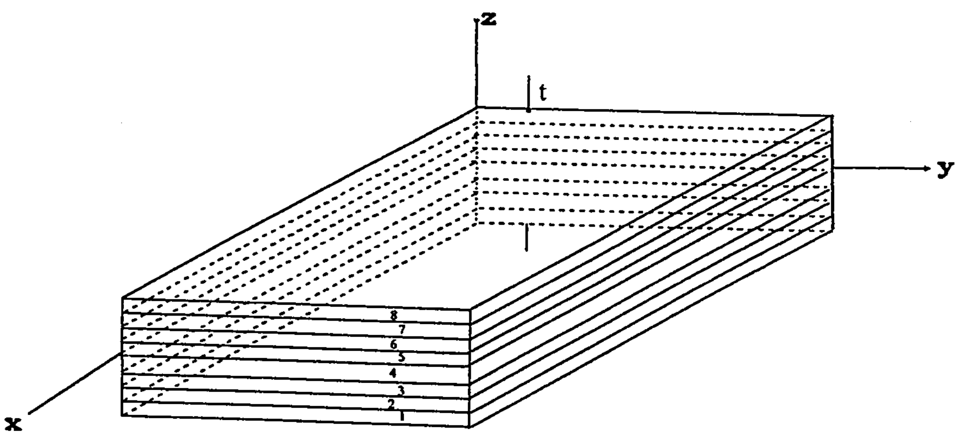

Figure 7.25: Stacking sequence nomenclature.

and distinctly separate but bonded layers are implied for the divided thickness. The distinct layers may compose of orthotropic or different isotropic material. For an isotropic situation, the layers would be composed of same isotropic material and hence it is understood that the layer interfaces are merely fictitious.

7.3.6.2 Problem Formulation

In order to show the effect of anisotropy and associated variation in lamina stacking arrangement, five models have been conceived as follows:

Models	Stacking Architectures	Materials
model-0	---	I (isotropic)
model-1	$[(90^o)_8]$	I
model-2	$[(90^o/0^o)_2]_s$	I
model-3	$[(90^o)_8]$	II
model-4	$[(90^o/0^o)_2]_s$	II

The first problem is essentially isotropic, but its relevance is in providing a test-case against which salient features of the remaining four (anisotropic) problems could be conveniently discriminated. Based on material I (E glass-epoxy) mechanical properties, the so-called bench-mark problem was however characterized to have $E = E_1$ and $\nu = \nu_{12}$. The second and third problems (models 1 and 2) strictly possess material I mechanical properties. They were closely analyzed to permit study for the effect of stacking architecture on the anisotropic mitre elastic stress responses. On a similar note the fourth and the fifth problems (models 3 and 4) have been considered, but more specifically in order to examine the effect of change in stacking material—especially that of high strength composite hence the use of material II mechanical properties.

In what follows, all stress quantities were normalized with respect to the maximum stress ($\sigma = pa/t$) that can be attained by thin-cylinder having the same a and t dimensions as those of the five outlined models. Although previous studies on isotropic mitres have consistently identified the intrado as the hot-spot location on the mitre-edge, lack of similar understanding on the part of the present anisotropic mitre study has made it imperative to sample stress quantities at two other locations which are next to intrado on the stress concentration ladder. Thus in addition to the intrado ($\theta = 0^o$), both the extrado ($\theta = 180^o$) and the crown ($\theta = 90^o$) of the mitre-edge have been ear-marked for closer scrutiny. Furthermore, at each of these three key locations, three key stress quantities in terms of the hoop stress ratio, the axial stress ratio, and the in-plane shear stress ratios were studied. The in-plane shear stress ratio (from now onwards referred to simply as shear stress ratio) has been considered for its perceived delamination effect in the mitre laminates.

7.3.6.3 Maximum In-Plane Stresses

To allow comparison with the anisotropic mitres, an isotropic single mitred bend subjected to internal pressure was said to be considered. Nonetheless by showing the across-the-thickness variation, the present isotropic study is expected to also provide a further insight into refined behavior of the mitre especially at such critical locations of mitred-edge intrado, crown and extrado.

Based on the three key-locations, the plots of the three in-plane stress quantities corresponding to the hoop stress ratio, the axial stress ratio and the shear stress ratio are illustrated in terms of their across-the-thickness variations in Fig. 7.26 through Fig. 7.30 for the five respective models.

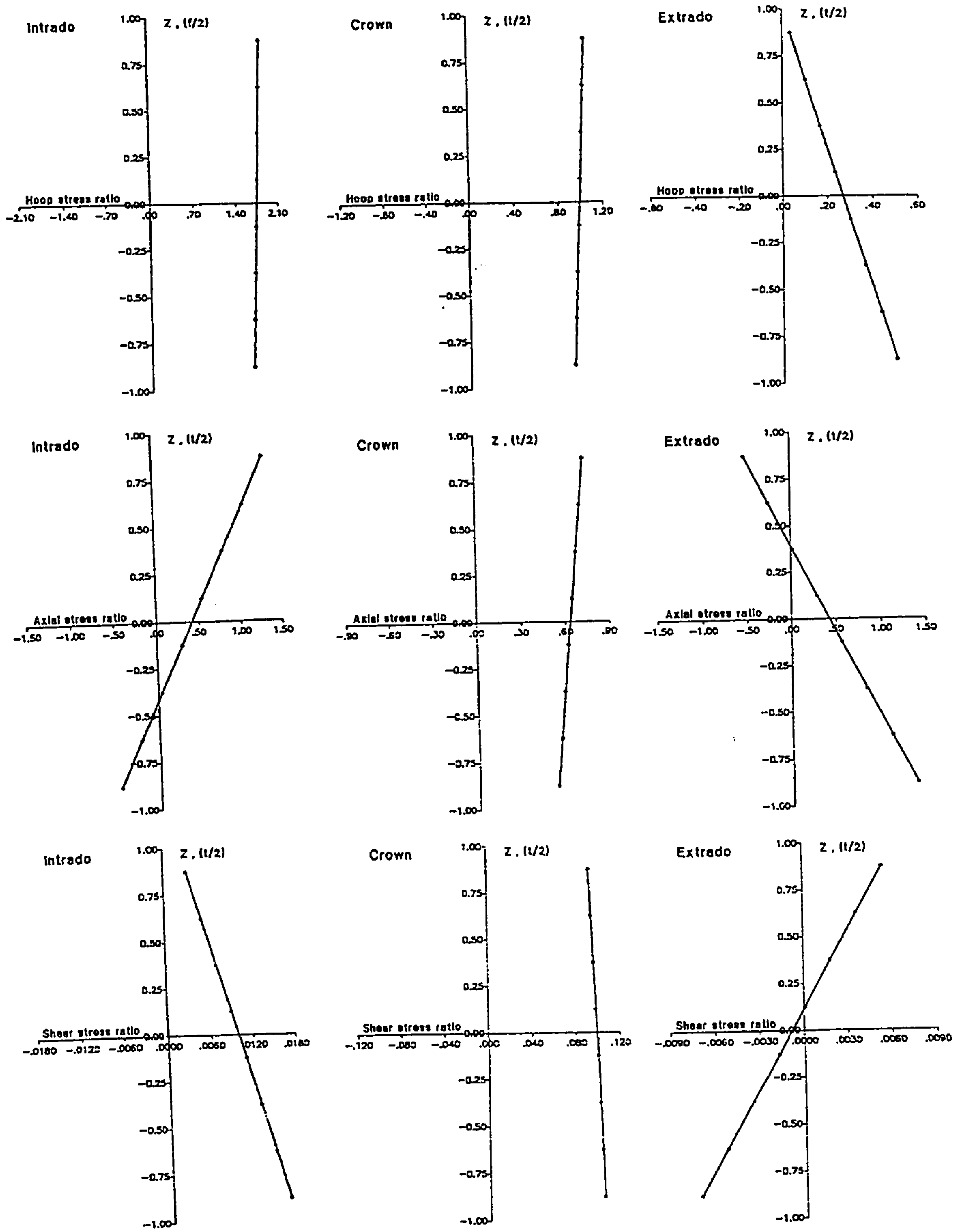

Figure 7.26: Normalized hoop, axial, and shear stress distributions at three mitre-edge locations of isotropic bench-mark model-0 (a) intrado (b) crown (c) extrado.

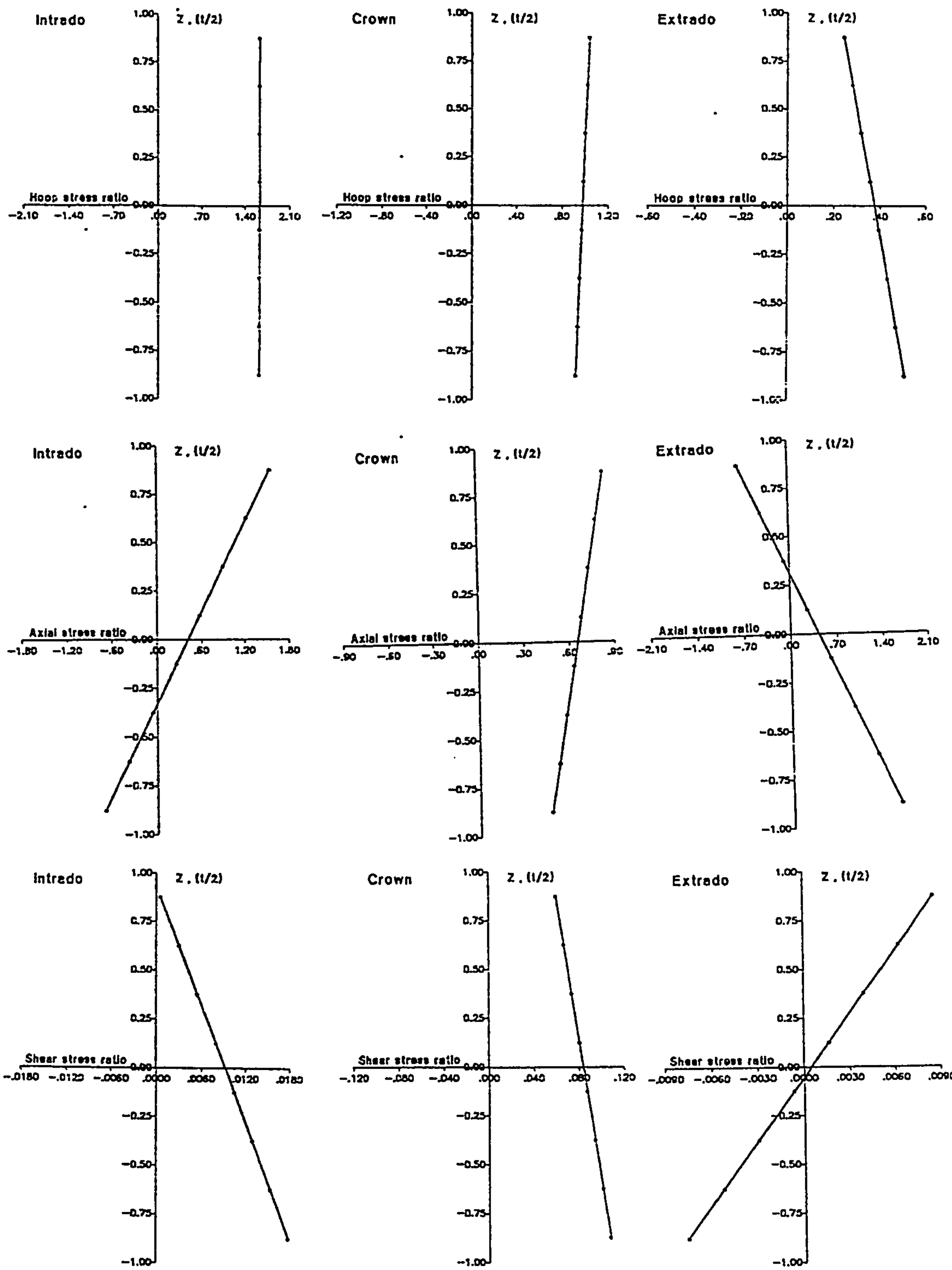

Figure 7.27: Normalized hoop, axial, and shear stress distributions at three mitre-edge locations of anisotropic E/Glass-epoxy, uni-ply mitre model-1 (a) intrado (b) crown (c) extrado.

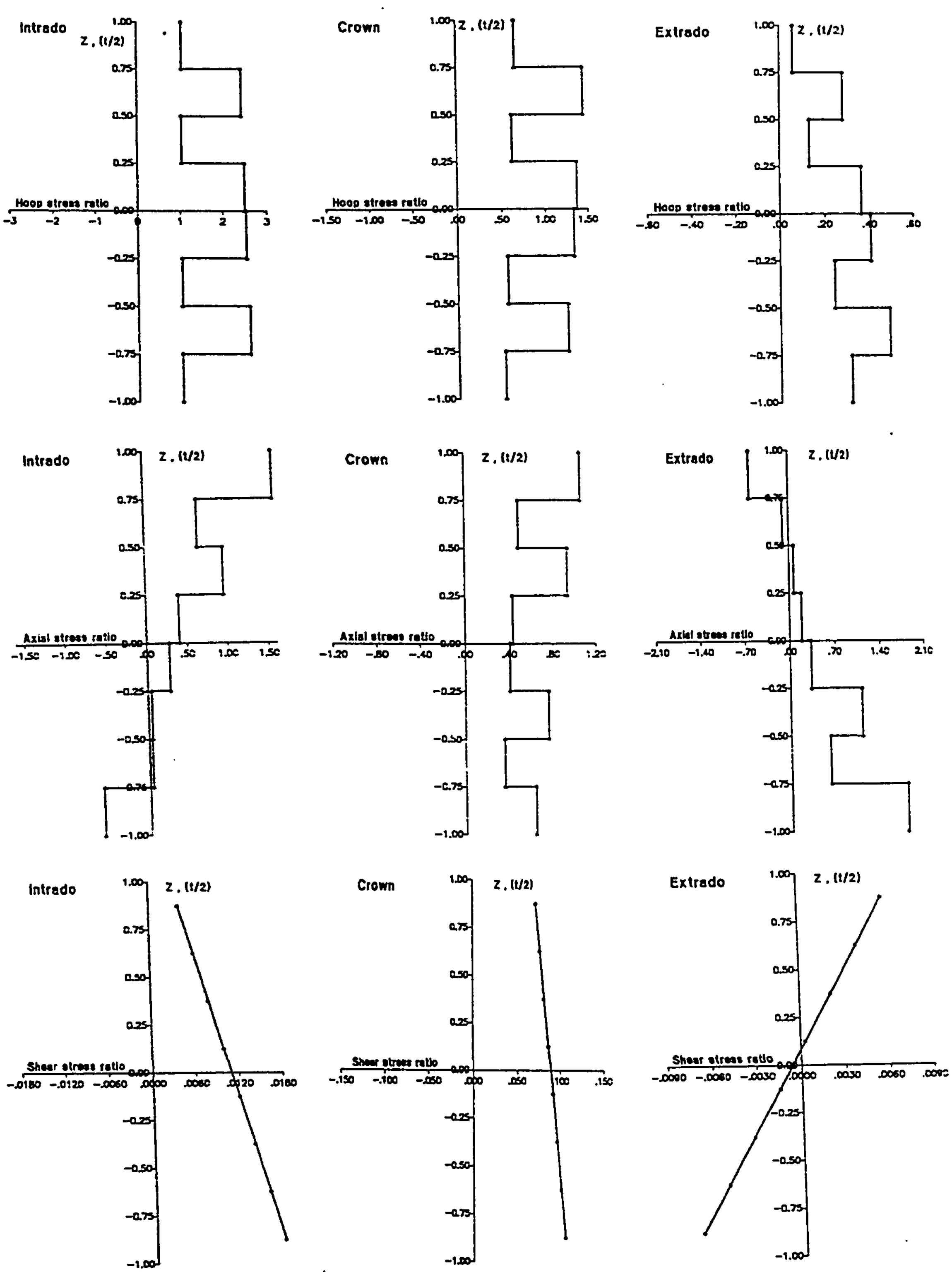

Figure 7.28: Normalized hoop, axial, and shear stress distributions at three mitre-edge locations of anisotropic E/Glass-epoxy, cross-ply mitre model-2 (a) intrado (b) crown (c) extrado.

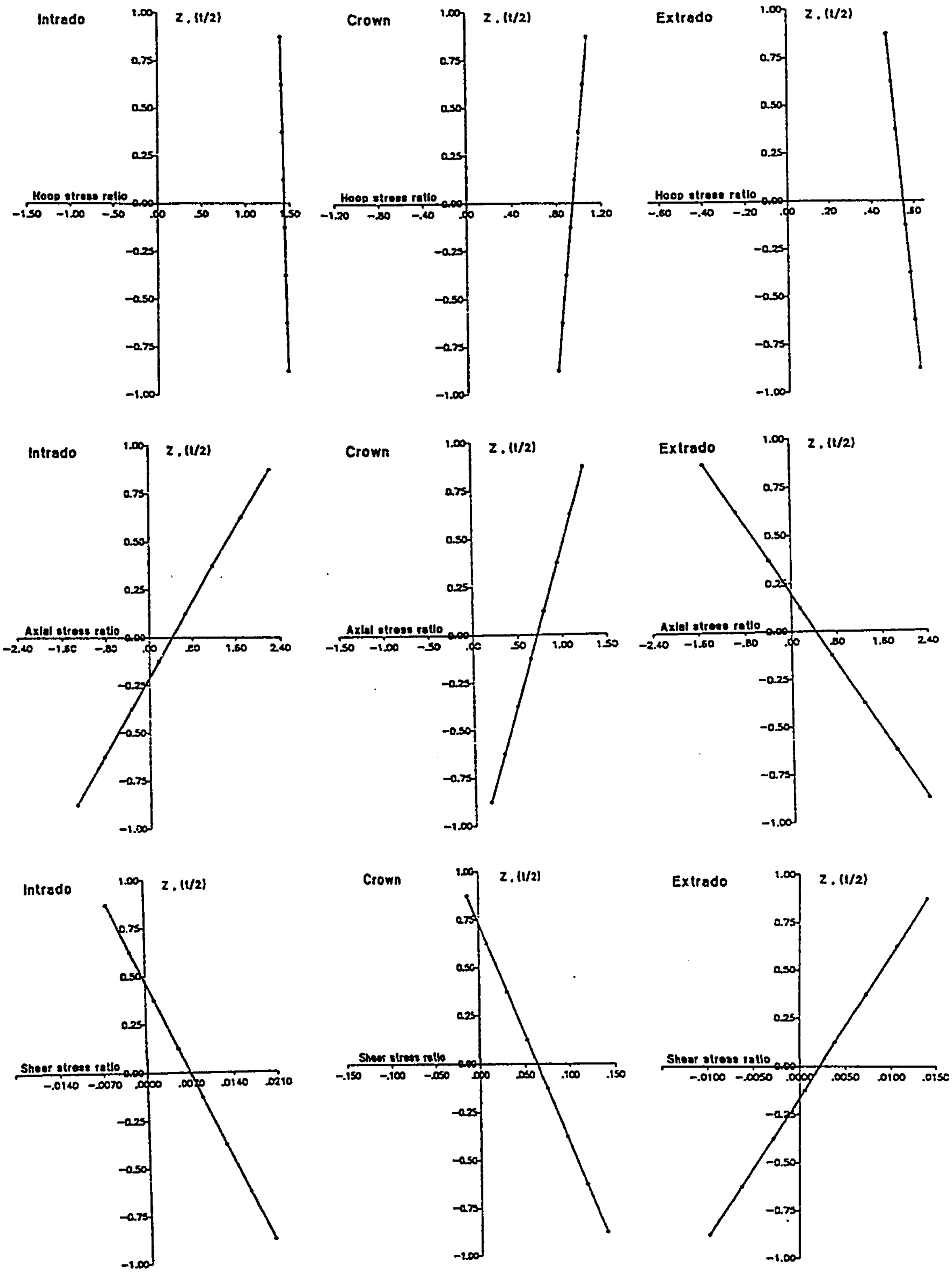

Figure 7.29: Normalized hoop, axial, and shear stress distributions at three mitre-edge locations of anisotropic Graphite-epoxy, uni-ply mitre model-3 (a) intrado (b) crown (c) extrado.

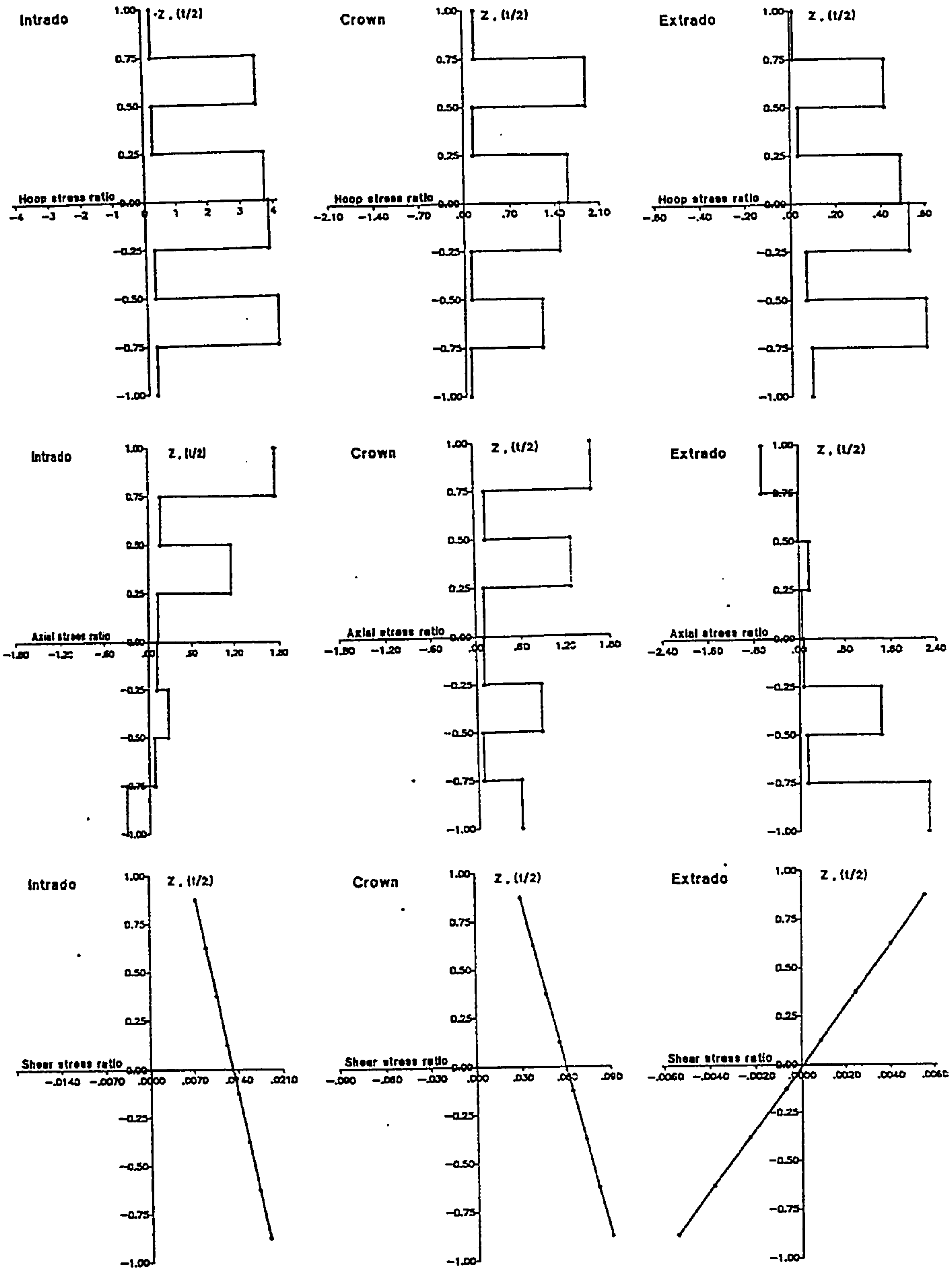

Figure 7.30: Normalized hoop, axial, and shear stress distributions at three mitre-edge locations of anisotropic Graphite-epoxy, cross-ply mitre model-4 (a) intrado (b) crown (c) extrado.

Referring to the results of the studied anisotropic and the bench-mark isotropic mitre models, Figs. 7.26 to 7.30, a couple of observations can be made to summarize the salient features concerning response of single mitred bend composed of composite materials. To start with, all (significant) stresses are generally confined to one (positive) side of the stress axis, except for the in-plane shear stress at the extrado where the shear assumed an asymmetric distribution with reversed (negative) tendencies in the bottom-half layers.

Although showing a slight variation at the extrados, the hoop stress variation is almost constant in similar layers of all the models. As suspected, the hoop stress for the $[(90^o/0^o)_2]_s$ cross-ply symmetric lay-up is not significant in the 90^o (outer) layers and this is more so for the ultra high stiffness material II mitres (models 3 and 4). Analogous observation to the latter instances applies to the axial stress as well—it is less significant in 0^o (inner) layers.

In the case of the crown, the variation of axial stress considering similarly oriented layers is not constant. Nonetheless, the crown consistently showed 'membrane' dominated behavior and can be regarded as the least destabilized region of the mitre-edge. A tendency to 'bending' behavior at the crown is seen to be exhibited only slightly by the anisotropic mitres, Figs. 7.27 to 7.30.

For all the stress plots in Figs. 7.26 to 7.30, the features of the in-plane shear stress variation are unaltered since they maintained similar tendency at corresponding locations, independent of the stacking architecture and material. An exception to the above assertion is seen for the case of the $[(90^o)_8]_s$ transversely isotropic mitres (models 1 and 3) in which a negative behavior was noticed in the outer (top) fibers at the intrado and the crown. This resulted in a distribution that is quite similar to that at extrado but in a reversed manner, Figs. 7.27 and 7.29.

Although the mitre-edge is a defacto hot-spot region in a single mitred bend, the magnitude and location at which the stress concentrations do take place are significantly influenced by the consideration of anisotropy, both in terms of the stacking architecture and the type of stacking material. Corresponding to Figs. 7.26 to 7.30, Table 7.2 gives a summarized comparison of the maximum stress ratios obatined for the five mitre models. The specific hot-spot locations corresponding to the indicated maximum stress ratio values are given in brackets. The maximum value may occur in a bottom (inner) or top (outer) layer of the isotropic, the transversely isotropic, or the cross-ply stacking arrangement, and therefore a minus sign (-) for bottom and a plus sign (+) for top have followed the corresponding hot-spot location in addition to the layer orientation as appropriate. Moreover, since the in-plane shear stress have been noticed to be actually maximum at locations on the mitre-edge different from the precise position at the intrado, the crown or the extrado, the actual maximum values are given below the corresponding local maximum shear stress values as shown in the table.

While Table 7.2 speaks for itself, it may be worth mentioning that whereas for model 1 both the hoop stress and the axial stress are maximum to the same degree, the same is not true in the case of the remaining models, including the bench-mark isotropic problem (model 0). Therefore for all intent, the use of E glass-epoxy and $[(90^o)_8]_s$ transversely isotropic lay-up has turned out to give the 'best' single mitred bend (model 1) which effectively utilized its hoop- and axially-directed stiffnesses.

This conclusion may however be subjective and may therefore be confined to the particular mitre geometry ($\alpha = 15^o$, $a/t = 20$) under consideration. Nonetheless, the set of discussion and illustrative plots presented herein could undoubtedly serve as a guide for possible interpolation or extrapolation to

Models	Maximum Stress Ratios		
	Hoop	Axial	Shear
model-0	1.830(I+)	1.390(E-)	0.105(C-) 0.271(CI-)
model-1	1.640(I+90°)	1.641(E-90°)	0.108(C-90°) 0.291(CI-90°)
model-2	2.600(I-0°)	1.810(E-90°)	0.105(C-90°) 0.274(CI-90°)
model-3	1.478(I-90°)	2.376(E-90°)	0.140(C-90°) 0.316(CI-90°)
model-4	4.070(I-0°)	2.250(E-90°)	0.090(C-90°) 0.244(IC-90°)

I=Intrado; C=Crown;E=Extrado; CI=between Crown and Intrado, but more towards theCrown, etc.

Table 7.2: Comparison of Maximum Stress Ratios: model-0, isotropic; model-1, E/Glass-epoxy uni-ply; model-2, E/Glass-epoxy cross-ply; model-3, Graphite-epoxy uni-ply; model-4, Graphite-epoxy cross-ply.

other mitre geometries. Moreover, since the particular situation involving the bench-mark isotropic mitre plots in Fig. 7.26 has more of a general bearing, it can indeed serve as a bench-mark towards other stacking materials or architectures. Some stacking arrangement, for instance, could permit better acceptability of material II in a way much more than predicted by the above two selected unidirectional and cross-ply stacking arrangements.

7.4 Applications of Transition Elements

In order to make the scope of the present study complete, the performance of the transition elements in enabling a desired change in degree of freedom (DOF) density in the mitre mesh system was explicitly checked in this section. Moreover, by carrying out the performance check above, the adequacy of the hitherto adopted basic-mesh models (that were assumed to be adequate) could be explicitly checked as well.

7.4.1 Transition-Mesh Model

The stress behavior of single mitred bend is often characterized by a 'front' at which the stress changes from high or rapidly varying values on one side (the edge-zone) to low or constant values on the other side (the smooth-zone). Therefore in developing an appropriate mitre mesh system that takes advantage of the reduced number of elements offered by change in DOF density when using transition elements, it has become important to recognize the existence of such a 'front'. According to a report by Pan et.al. [40] the edge-zone which is internal to the 'front' is very much within twice the characteristic length ($L_x = 2.544\sqrt{(at)}$) of the mitre. This is consistent with observed tendency of the axial distribution of stress quatities as illustrated in Figs. 7.4b and 7.5b.

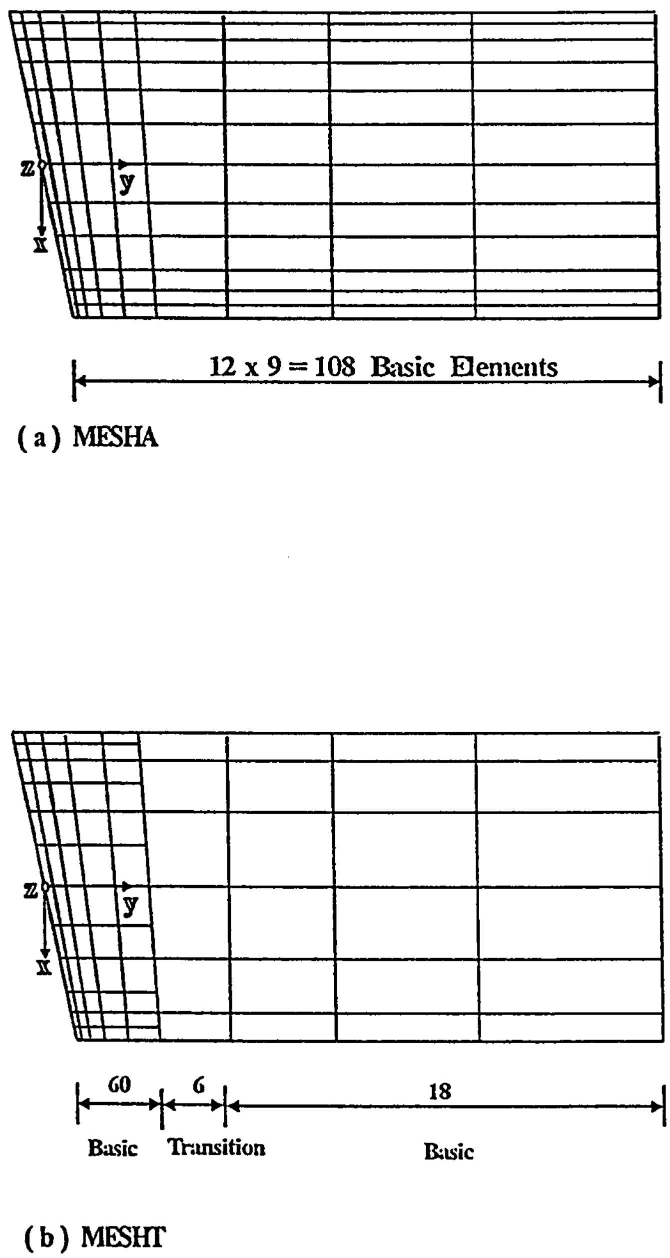

Figure 7.31: Transition/Basic mesh models (a) MESHA: basic-mesh (b) MESHT: transition mesh

7.4.2 Elasto-Plastic Case Study

In the present treatment only internal pressure is considered. Hence a case study with respect to results obtained for the mitre model-1 ($\alpha = 15^o$, $a/t = 20$) of section 7.3.3.1 has been chosen for comparison. As such the parallelism between the finer and the coarser meshes will be drawn based on, respectively, the basic-mesh model (MESHA: 108 elements which are purely basic-elements) and the transition-mesh model (MESHT: 84 elements comprising 78 basic elements and 6 transition-elements) which are shown in Fig. 7.31.

In passing it should be noted that the edge-zone discretization and its extent in the hoop and axial directions as used in the basic-mesh model A has been duly preserved in the transition-mesh model. However, in addition to the presence of the transition elements, the smooth-zone of the transition-mesh is different from that in the basic-mesh model since the hoop direction has been only divided into six (6) in the former against twelve (12) in the latter. It is this difference that entailed more than 22% saving in the number of elements used in the transition-mesh model. The relative performance of the two mesh models is still to be accounted for. however.

In Fig. 7.32, the transition-mesh (MESHT) and the basic-mesh (MESHA) are compared for (radial) displacements. The plots in parts a,b, and c of the figure respectively correspond to (radial) displacement at the intrado and the extrado of the mitre-edge and at the crown of the free-edge.

The plots for the (radial) displacement at the intrado of the mitre-edge, Fig. 7.32a, is the key deformation response of a mitre under internal pressure load. Nonetheless, and despite the fewer number of elements in the transition-mesh the results of both meshes agree closely. Similar agreement is also being exhibited between the two mesh models for the other responses in parts b and c of Fig. 7.32.

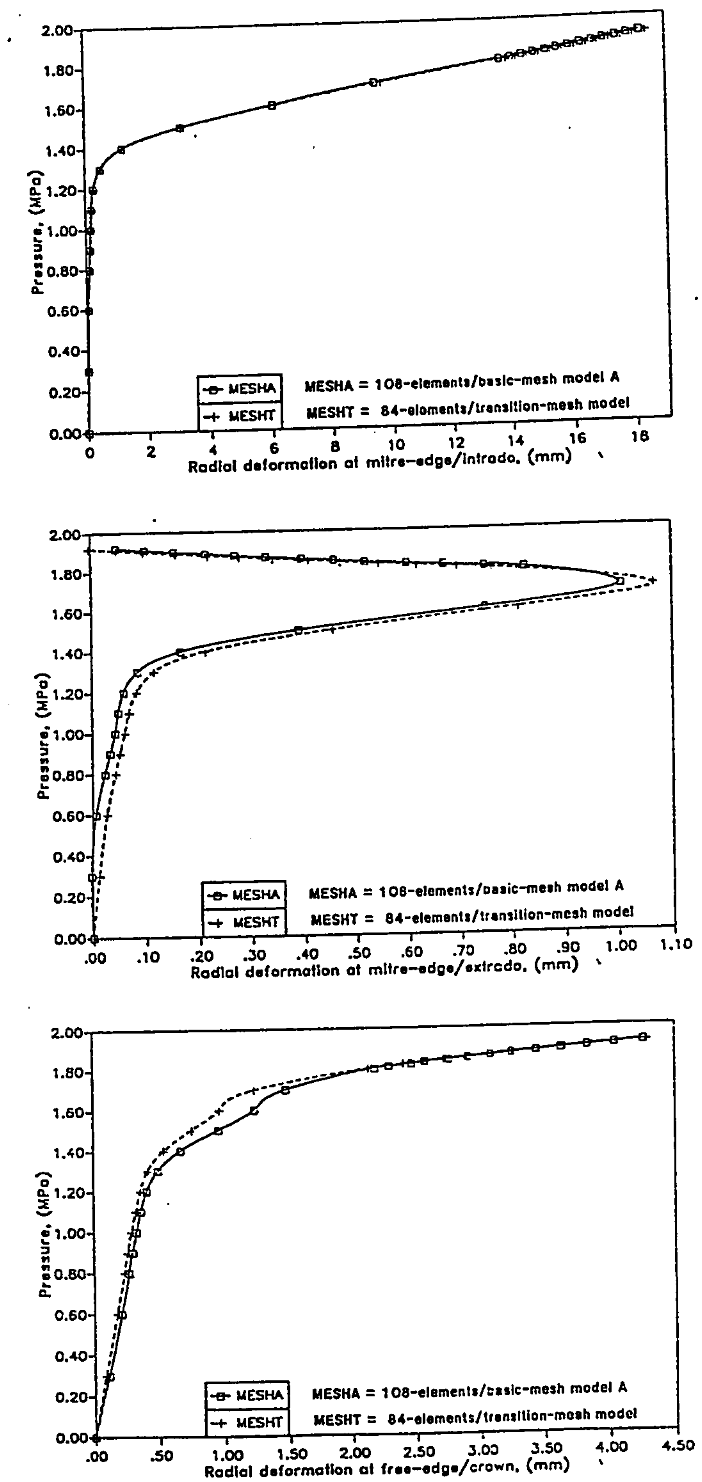

Figure 7.32: Comparison of Load-Displacement curves for two mesh models corresponding to location at (a) mitre-edge/intrado (b) mitre-edge/extrado (c) free-edge/intrado.

Chapter 8

CONCLUSIONS AND RECOMMENDATIONS

8.1 Conclusions

This study included the development and use of a nonlinear Finite Element program, **PLAMBS7**, to investigate the nonlinear response of single mitred bends subjected to either pressure or in-plane bending. Based on the investigation and the obtained results, the following general conclusions can be made:

1. Nonlinear finite element method is a very useful technique for the investigation of the complex behavior of single mitred bends. The results indicate the success of the developed software, **PLAMBS7** , in accurately modelling the reponse of single mitred bends.

2. As the literature indicated, very limited results were published in the field of nonlinear response of single mitred bends. Therefore, it is believed that the current study and its main output, **PLAMBS7** , will fill a void in the knowledge within the field of pressure vessels and piping systems.

3. The incorporation of 3 different shell elements was instrumental in verifying the numerical results, given the numerical sensitivity and com-

plexity of the attempted problem. Furthermore, it was concluded that the Lagrangian element is the most suitable element for the analysis, and was chosen to be the main element in the study.

4. The study presented an extended-layer scheme, which allows for the use of layers that have two or three gauss points each, instead of the classical single gauss point. This integration scheme was found to be very useful for obtaining the most accurate answers, with the least possible number of numerical operations.

5. Analysis of single mitred bends was found to be very sensitive to the finite element mesh, and can be erroneous if the selected mesh is not suitable. Results showed that meshes comprising 108 and 168 elements are useful for the analysis of the studied mitred bends when subjected to pressure or bending, respectively.

6. Verification of **PLAMBS7** elastic results showed excellent agreement with experimental results obtained by other investigators for both loading types. Hoop and axial stress levels and distributions were verified at the mitre joint and along the pipe axis.

7. Elasto-plastic results for a single mitred bend ($\alpha = 45^o$) subjected to in-plane bending showed excellent agreement with experimental results, and acceptable agreement with published results obtained using another finite element code, ABACUS.

8. The importance of geometric nonlinearity in the analysis of single mitred bends can not be underestimated, as was evident in the completely different nonlinear responses obtained for opening and closing bending moments.

9. Collapse load tests for single mitred bends subjected to internal pressure showed that the mitre angle α has significant effects on the load levels at which plastification is initiated and gross collapse is observed. On the other hand, the radius-thickness ratio was confirmed as the key factor influencing the total collapse pressure.

10. Because of its layered approach capabilities, the developed software, **PLAMBS7** , was found to be useful for the elastic analysis of composite single mitred bends. The results showed that the high stress concentrations, which are common in such structres, can be reduced through the use of the proper composite material.

8.2 Recommendations

Based on this study and previous conclusions, the following recommendations, pertaining to future modifications of **PLAMBS7** , can be made:

1. An integration of **PLAMBS7** with an automatic mesh-generation and similar pre- and post-processing routines is essential, to reduce the amount of effort in problem input and output.

2. To facilitate the elasto-plastic analyses, an adaptive load incremental algorithm is advised. This will eliminate the need to use the **RESTART** facility in cases involving premature collapse.

3. To allow for uniform displacement at the mitre end, a displacement 'load-increment' should be included.

4. To allow for bimodular elastic behavior of composite materials, separate sets of elastic properties in tension and compression need to be considered.

5. For nonlinear anisotropic elasto-plastic analysis, a sound idealization based on bimodular strength and moduli of such materials is desirable.

6. Investigation of other load types, such as out-of-plane bending, and/or combinations of different load types need to be addressed in fututre versions of **PLAMBS7** .

Bibliography

[1] S.S. Gill. *The stress Analysis of Pressure Vessels and Pressure Vessel Components.* Pergamon Press, Oxford, 1970.

[2] Battle, K.; Carmichael, G.D.T.; Cresswell, E.; Morse, D.; Porter, H.; Poppwell, P. L.; and Riley. K. The design of mitred bends - a background to BS 806 : 1975 ammendement no. 3. *Proc. Inst. Mech. Eng.*, 200(1A):pp51–58, 1986.

[3] A. Loghman and M.A. Wahab. Loading and unloading of thick-walled cylindrical pressure vessels of strain hardening material. *J. Pres. Ves. Tech*, 116:105–109, 1994.

[4] V.V. Novozhilov. *Thin Shell Theory.* Noordhoff Ltd., Gröingen, Netherlands, 2d ed. edition. 1964.

[5] V.Z. Vlasov. General theory of shells and its applications in engineering. Ttf-99, NASA, April 1964.

[6] B.S. Owen and W.C. Emmerson. Elastic stresses in single mitred bends. *J. Mech. Eng. Sci.*, 5:pp303–324, 1963.

[7] M.V.V. Murthy. Stresses in a mitred pipe joint under uniform internal pressure. *Int. J. mech. Sci.*. 6:pp361–370, 1964.

[8] J.M. Corum. A theoretical and experimental investigation of the stress in a circular cylindrical shell with an oblique edge. *Nuclear Eng. and Design*, 3:pp256–280, 1966.

[9] M.V.V. Murthy. Stresses at the intersection of two cylindrical shells of equal diameter. *Int. J. Solids Str.*, 5:pp879–892, 1969.

[10] M.P. Bond and R. Kitching. Multi-mitred and single-mitred bends subjected to internal pressure. *Int. J. Mech. Sci.*, 13:pp471–488, 1971.

[11] A.E. Green and W.C. Emmerson. Stresses in a pipe with a discontinuous bend. *J. Mech. Phys. Solids*, 9:pp91–104, 1961.

[12] A. Kornecki. State of stress in a thin-walled tube rigidly fixed to an oblique cross-section (in polish). *Rozpr. Inzynierski*, 5:pp119–134, 1957.

[13] A. Van der Neut. Bending at the oblique end section of cylindrical shells. In *Proc. Symp. Theory of Thin Elastic Shells,Delft*, pages pp247–269. North Holland Pub. Co., Amsterdam, 1960, August 1957.

[14] M.W. Johnson and E. Reissner. On the foundation of the theory of thin elastic shells. *J. Math. Phys.*, 31:pp371, 1959.

[15] Jones, R. and Kitching, R. A theoretical study of in-plane bending of single unreinforced mitred-bend. *J. Strain Analysis*, 1(3):pp264–276, 1966.

[16] R. Kitching. Mitred bends subjected to in-plane bending moments. *Int. J. Mech. Sci.*, 7:pp551–575, 1965.

[17] R. Kitching and M.P. Bond. Flexibility and stress factors for mitred bends under in-plane bending. *Int. J. Mech. Sci.*, 12:pp267–285, 1970.

[18] M.P. Bond and R. Kitching. Stress and flexibility factors for multi-mitred bends subjected to out-of-Plane bending. *J. Strain Analysis*, 6(4):213–225, 1971.

[19] W. Flügge. *Stresses in Shells.* Springer-Verlag. Berlin, Heidelberg, 2nd ed. edition, 1973.

[20] A.W. Chan and J.L. Sanders. Analysis of mitred joint in a cylindrical shell in bending. *Int. J. Mech. Sci.*, 22:pp621–636, 1980.

[21] N. Jones and R. Kitching. An experimental investigation of a right-angled single unreinforced mitred-bend subjected to various bending moments. *J. Strain Analysis*, 1(3):pp248–263, 1966.

[22] Yoshiaki Sawa. Photoelastic stress analysis in mitred bend under internal pressure. *Nippon Kikkai Gakkai Ronbunshu. A Hen. (in Japanese)*, 53(496):2416–2421, 1987.

[23] R. Kitching. In-plane bending of a 180° mitred pipe bend. *Int. J. Mech. Sci.*, 7:pp721–736, 1965.

[24] R. Kitching and W.J. Thompson. In-plane bending of single, unreinforced mitred pipe bends. *J. Strain Analysis*, 5, No.1:pp14–24, 1970.

[25] Yoshiaki Sawa. Photoelastic investigation of the stresses in mitred Bent-Cylinders under bending. *Bulletin of the JSME*, 25(209):1662–1667, 1982.

[26] K. Fullard. The calculation of thermal stresses in a Cylinder-Cylinder intersection by means of finite elements. *Int. J. Pres. Ves. & Piping*, 1:177–198, 1973.

[27] V.N. Skopinsky. Numerical stress analysis of intersecting cylindrical shells. *J. Pres. Ves. Tech.*, 115:pp275–281, 1993.

[28] T. Fujimoto and T. Soh. Flexibility factors and stress indices for piping components with $d/t \geq 100$ subjected to in-plane or out-of-plane moment. *J. Pres. Ves. Tech.*, 110:pp374–386, 1988.

[29] Kormi, K., Webb, D.C., and Montague, P. Crash behavior of circular tubes with large side opening. *Int. J. Mech. Sci.*, 35(314):193–208, 1993.

[30] D.H. Bonde and K.P. Rao. Circular elastic inclusions in cylindrical shells. *Comput. Struct.*, 8:349–355, 1978.

[31] Nwosu, D.I., Swamidas, A.S.J., and Munaswamy, K. Numerical stress analysis for fatigue evaluation of welded tubular T-Joints. *Canadian J. Civ. Eng.*, 20:269–286, 1993.

[32] M.; Sundaravadivelu, R.; Hariharan and C. Ganapathy. Formulas for variation of stress concentration around intersection in tubular joints. *J. Ener. Res. Tech., Trans. ASME*, 110:237–244, 1988.

[33] R.S.; Dijkstra, O.D.; Puthli and H.H. Snijder. Stress concentratio factors in t and K-T tubular joints using finite element analysis. *J. Ener. Res. Tech., Trans. ASME*, 110:246–254, 1988.

[34] D.G. Moffat and J. Mistry. Interaction of external moment loads with internal pressure on an equal diameter branch pipe intersection. *J. Pres. Ves. Tech., Trans. ASME*, 108:443–452, 1986.

[35] S. Scola and R.G. Redwood. Behavior of axially loaded tubular V-Joints. *J. Construct. Steel Res.*, 16:89–109, 1990.

[36] M. Abo-Elkhier. Analysis of pipe bends using pipe elbow element. *Comput. Struct.*, 37(1):pp9–15, 1990.

[37] R.D. Cook. Axisymmetric finite element analysis for pure moment loading of curved beams and pipe bends. *Comput. Struct.*, 33(2):pp483–487, 1989.

[38] H. Ohtsubo and O. Watanabe. Stress analysis of pipe bends by ring elements. *J. Pres. Ves. Tech.*, 100:pp112–122, 1978.

[39] V.N. Skopinskii and G.M. Mellerovic. A Numerical-Experimental study of the stress state of pipeline joints. *Problems of the Strength (Translated)*, -(12):73–76, 1988.

[40] T.L.; Pan, Y.S.; Anderson and G.H. Skopp. Three-dimensional stress analyses of mitred elbows. *Int. J. Pres. Ves. & Piping*, 4:pp285–313, 1976.

[41] O. Watanabe and H. Ohtsubo. Stress analysis of mitred bends by ring elements. *J. Pres Ves. Tech.*, 106:pp54–62, 1984.

[42] A.A. Khathlan. Efficient stress analysis of piping systems : Application to mitred bends. In *Proc. Third Saudi Conf., Vol. 2, No. 24/27*, pages pp926–931, 1991.

[43] Control-Data Corporation. *MARC-CDC User's Manual, Vol. I.*

[44] C.D. Momte(Jr.). Global-Local finite element. *Int. J. Numer. Meth. Engrg.*, 3(4):565–574, 1971.

[45] W. Jiang. The Elastic-Plastic analysis of Tubes-I : General theory. *J. Pres. Ves. Tech.*, 114:213–221, 1992.

[46] W. Jiang. The Elastic-Plastic analysis of Tubes-II : Variable loading. *J. Pres. Ves. Tech.*, 114:222–228, 1992.

[47] W. Jiang. The Elastic-Plastic analysis of Tubes-III : Shakedown analysis. *J. Pres. Ves. Tech.*, 114:229–235, 1992.

[48] W. Jiang. The Elastic-Plastic analysis of Tubes-IV : Thermal ratcheting. *J. Pres. Ves. Tech.*, 114:236–245, 1992.

[49] D. P. Roach and T.G. Priddy. Effect of material properties on the strain to failure of thick-walled cylinders subjected to internal pressure. *J. Pres. Ves. Tech*, 116:95–104, 1994.

[50] A. Mendelson. *Plasticity Theory and Application.* The Macmillan Company, New York, N.Y., 1968.

[51] C. Cinquini. Limit analysis of circular shells under hydrostatic pressure. *J. Struct. Mech.*, 12(3):263–278, 1984.

[52] A. Muc and J. Skrzypek. Limit state of geometrically Non-linear Elastic-Plastic toroidal shells under pressure with bending. *Int. J. Mech. Sci.*, 30(5):347–363, 1988.

[53] J. Bielski and J. Skrzypek. Failure modes of Elastic-Plastic curved tubes under external pressure with In-Plane bending. *Int. J. Mech. Sci.*, 31(6):435–458, 1989.

[54] Kitching, R.; Rahimi, G.H.; and Soh, H.S. Plastic collapse of single mitred pipe bends. *Int. J. Pres. Ves. & Piping*, 38:pp129–145, 1989.

[55] Hibbith, Karlson & Sorenson, Inc., Providence, RI. USA. *ABACUS Example Problem Manual. Vol. 1 and 2*, 1984.

[56] T.K. Hellen. Elastic-Plastic analysis in an In-Plane loaded pipe bend. In *Numerical Methods for Non-linear Problems, Proceedings of the Int. Conf.*, Univ. Coll. Swansea, 1980. Pineridge Press.

[57] David Bunshnell. Elastic-Plastic bending and buckling of pipes and elbows. *Comput. Struct.*, 13:241–248, 1981.

[58] David Bunshnell. Plastic buckling. S.Y. Zamrik and D. Dietrich, editors, *Pres. Ves. and Piping; Design and Tech. -1982–A Decade of Progress*, pages 102–107, New York, 1982. ASME.

[59] N. Suzuki and M. Nasu. Non-linear analysis of welded elbows subjected to in-plane bending. *Comput. Struct.*, 32(3/4):pp871–881, 1989.

[60] K. Kawashima and T. Ito. Elastic-Plastic Behavior of Curved Tubes Under In-Plane Bending with Axial Force. *Design and Analysis of PVP and Components, ASME*, 235:45–52, 1992.

[61] T.K. Hellen and S.J. Protheroe. The BERSAFE finite element system. *Comp. Aided Design*, 6(1):15–24, 1974.

[62] K.J. Bathe. *ADINA*. Report MIT 82448-2, 1977.

[63] T. Kawai. New element models in discrete structural analysis. *J. Soci. Naval Arch. Japan*, -(141):174–180, 1977.

[64] R. Kitching and D.R. Hose. The influence of the variation in wall thickness of glass fibre reinforced plastic pipe bends subjected to in-plane bending. *J. Strain Analysis*, 21(2):pp113–121, 1992.

[65] R. Kitching and D.R. Hose. Laminated pipe bends of mixed wall construction subjected to an in-plane bending moment. *J. Strain Analysis*, 24(3):pp127–138, 1989.

[66] J.N. Reddy. Analysis of layered composite plates accounting for large deflections and transverse shear strains. In *Recent Advances In Non-Linear Computational Mechanics*. Pineridge Press Ltd., Swansea, U.K., 1982.

[67] J. Ye and K.P. Soldatos. Three-Dimensional stress analysis of orthotropic and Cross-Ply laminated hollow cylinders and clinderical panels. *Comput. Methods Appl. Mech. Engrg.*. 117:331–351, 1994.

[68] Y.A. Bahei-El-Din. Finite element analysis of Elastic-Plastic fibrous composite structures. *Comput. Struct.*, 13:321–330, 1981.

[69] A.K. Noor. Survey of computer programs for solution of nonlinear structural and solid mechanics problems. *Comput. Struct.*, 13:425–465, 1981.

[70] D.R.J. Owen and J.A. Figueiras. Anisotropic elasto-plastic finite element analysis of thick and thin plates and shells. *Int. J. Numer. Mth.*. 19:pp541–566, 1983.

[71] R. Hill. *The Mathematical Theory of Plasticity.* Clarendon Press, Oxford, 19950.

[72] E. Hinton and D.R.J. Owen. *Finite Element Software for Plates and Shells.* Pineridge Press, Swansea, U.K., 1984.

[73] D.R.J. Owen and J.A. Figueiras. Elasto-plastic analysis of anisotropic plates and shells by the semiloof element. *Int. J. Numer. Mth. Eng.*, 19:pp521–539, 1983.

[74] I. Cormeau. Elastoplastic thick shell analysis by viscoplastic solid finite elements. *Int. J. Numer. Mth. Eng.*, 12:pp203–227, 1978.

[75] R. Hill. A theory of yielding and plastic flow of anisotropic metals. *Proc. Roy. Soc. London*, 193, 1948.

[76] M.A. Daye and T.G. Torids. Elasto-Plastic algorithms for plates and shells under static and dynamic loads. *Comput. Struct.*, 39(1/2):195–205, 1991.

[77] D.R.J. Owen and E. Hinton. *Finite Element in Plasticity : Theory and Practice.* Pineridge Press, Swansea, U.K., 1980.

[78] Yang, H.T.Y.; Saigal, S.; and Liaw, D.G. Advances of Thin Shell Finite Elements and some Applications–Version I. *Comput. Struct.*, 35(4):pp481–504, 1990.

[79] J. Backlund and H. Wennerstrom. Finite element analysis of elasto-plastic shells. *Int. J. Numer. Meth. Eng.*, 8:pp415–424, 1974.

[80] H.V. Lakshminarayana and S. Viswanath. A high precision triangular laminated anisotropic cylindrical shell finite element. *Comput. Struct.*, 8:633–640, 1978.

[81] D.A. Grant. Elastoplastic analysis of hollow spheres subjected to external pressure loading. *Int. J. Numer. Mth. Engrg.*, 8:803–809, 1974.

[82] S.A. Schimmels and A.N. Palozotto. Nonlinear geometric and material behavior of shell structures with large strains. *J. Eng. Mech., (ASCE)*, 120(2):pp320–345, 1994.

[83] C.K. Choi and S.W. Yoo. Geometrically nonlinear behavior of an improved degenerated shell elements. *Comput. Struct.*, 40(3):pp785–794, 1991.

[84] M.A. Polak and F.J. Vecchio. Nonlinear analysis of reinforced concrete shells. *J. Struct. Engrg. (ASCE)*, 119(12):3439–3462, 1993.

[85] W.A. Cook. A finite element model for nonlinear shells of revolution. *Int. J. Numer. Meth. Engrg.*, 18:163–171, 1982.

[86] S.S. Murthy and R.H. Gallaghar. Anisotropic cylindrical shell element based on discrete kirchhoff theory. *Int. J. Numer. Meth. Eng.*, 19:pp1805–1823, 1983.

[87] K.Y. Sze and C.L. Chow. A mixed fomulation of a four-node mindlin shell/plate with interpolated covariant trasverse shear strains. *Comput. Struct.*, 40(3):pp775–784. 1991.

[88] Zienkiewicz, O.C., Taylor. R.L., Papadopoulos, P. and Onate, E. Plate bending element with discrete constraints : New triangular elements. *Comput. Struct.*, 35(4):pp505–522, 1990.

[89] A.V. Saetta and R.V. Vitaliani. A finite element formulation for shells of arbitrary geometry. *Comput. Struct.*, 37(5):781–793, 1990.

[90] R.D. Mindlin. Influence of rotary inertia and shear on flexural motions of isotropic, elastic plates. *J. Appl. Mech.. Trans, ASME*, 18(1):31–38, 1951.

[91] E. Reissner. The effect of transverse shear deformation on the bending of elastic plates. *J. Appl. Mech., Trans. ASME*, 12(2):69–77, 1945.

[92] L.M.S. Dinis and D.R.J. Owen. Elasto-Viscoplastic and Elasto-Plastic large deformation analysis of thin plates abd shells. *Int. J. Num. Mth. Engrg.*, 18:591–607, 1982.

[93] H. Stolaski and T. Belytscho. Shear and membrane locking in c^o elements. *Comp. Meth. Appl. Mech. Engrg.*, 41:279–296, 1983.

[94] W. Weaver and P.R. Johnston. *Finite Elements for Structural Analysis*. Printice-Hall, Eaglewood Cliffs, New Jersy, 1984.

[95] W.F. Coper and K.M. Will. A Three-Dimensional Shell-Solid transition element for general nonlinear analysis. *Comput. Struct*, 38(4):449–462, 1991.

[96] H. Parisch. A critical survey of the 9-node degenerate shell element with special emphasis on thin shell application and reduced integration. *Comput. Meth. Appl. Mech. Eng.*, 20:pp323–350, 1979.

[97] C. Choi and J. Paik. An efficient four node degenerated shell element based on the assumed covariant strain. *Struct. Eng. Mech.*, 2(1):17–34, 1994.

[98] C.W.S To and M.L. Liu. Hybrid strain based Three-Node flat triangular shell elements. *Finite Element in Analysis and Design*, 17:169–203, 1994.

[99] J. Rakowski. The interpretation of the shear locking in beam elements. *Comput. Struct.*, 37(5):769–776, 1990.

[100] K.Y. Sze. An explicit Hybrid-Stablized 9-Node lagrangian shell element. *Comp. Meth. Appl. Mech. Engrg.*, 117:361–379, 1994.

[101] A.F.; Chang, T.Y.; Saleeb and W. Graf. On the mixed formulation of a 9-Node lagrangian shell element. *Comp. Meth. Appl. Mech. Engrg.*, 73:259–281, 1989.

[102] T.T.R. Hughes and M. Cohen. The heterosis finite element for plate bending. *Comput. Struct.*, 9:445–450, 1978.

[103] H.; Belytschko, T.; Stolaski and W.K. Liu. Stress projection for membrane and shear locking in shell finite elements. *Comp. Meth. Appl. Mech. engrg.*, 15:221–258, 1985.

[104] H.C. Huang and E. Hinton. A new nine node degenerated shell element with enhanced membrane and shear interpolation. *Int. J. Numer. Meth. Engrg.*, 22:73–92. 1986.

[105] J.R. Astley. *Finite Element in Solids and Structures (An Introduction).* Chapman & Hall, London, 1992.

[106] K.S. Surana. Geometrically Non-linear formulation for the Three-Dimensional stress analysis. *Int. J. Numer. Meth. Engrg.*, 15:991–1020, 1980.

[107] D.S. Burnett. *Finite Element Analysis: From Concepts to Applications.* Addison-Wesly Pub. Co., Reading, Massachusetts, 1987.

[108] T.J.R. Hughes and W.K. LIU. Nonlinear finite analysis of shells – Part I : Three-Dimensional shells. *Comp. Meth. Appl. Mech. Engrg.*, 26:331–362, 1981.

[109] W. Weaver and J.M. Gere. *Matrix Analysis of framed Structures.* Van Nostrand Reinhold. New York, 1990.

[110] T.R.J. Hughes. *The Finite Element Methods.* Eaglewood Cliffs, New Jersy, NJ, 1987.

[111] S.H. Lo. Automatic mesh generation and adaptation by using contours. *Int. J. Numer. Mth. Eng.*, 31:pp689–707, 1991.

[112] L.T. Souza and M.A. Gattas. A new scheme for mesh generation and mesh refinement using graph theory. *Comput. Struct.*, 46(6):1073–1084, 1993.

[113] P.; Coorevits, P.; Ladevéze and J.P. Pelle. Mesh optimization for problems with steep gradients. *Eng. Computations*, 11:129–144, 1994.

[114] M.G. Kittur and R.L. Huston. Finite element mesh refinement criteria for stress analysis. *Comput. Struct.*, 34(2):pp251–255, 1990.

[115] N.U. Ahmed and P.K. Basu. Higher order modelling of plates by p-version of finite element method. *J. Eng. Mech.*, 119(6),ASCE:1228–1242, 1993.

[116] J. Fish. The s-version of the finite element method. *Comput. Struct.*, 43(3):539–547, 1992.

[117] D.M. Tracey. Adaptive load incrementation in Elastic-Plastic finite element analysis. *Comput. Struct.*, 13:45–53, 1981.

[118] M.A. Criesfield. A fast incremental/iterative solution procedure that handles "snap through". *Comput. Struct.*, 13:55–62, 1981.

[119] Cesari, F.; Gheduzzi, P.; Vannini, L; and Hellen, T.K. The feasibility of finite element codes for elasto-plastic analysis (Volume I; Edited by Taylor, C.; Hinton, E.; and Owen, D. R. J.). In *Numerical Method for Non-Linear Problems*, pages pp27–35. Pineridge press, Swansea, U.K, 1980.

[120] T.Y. Yang and S. Saigal. A curved quadrilateral element for static analysis of shells with geometric and material nonlinearities. *Int. J. Numer. Meth. Eng.*, 21:pp617–635, 1985.

[121] E. Hinton and D.R.J. Owen. *Introduction to Finite Element Programming.* Academic Press, London, 1977.

[122] B.M. Irons. A frontal solution program for finite element analysis. *Int. J. Numer. Meth. Engrg.*, 2:5–32, 1970.

[123] S.F. Abbas. Some novel applications of the frontal concept. *Int. J. Numer. Meth. Engrg.*, 15:519–536, 1980.

[124] G. Beer. A partitioned frontal solver for finite element analysis. *Int. J. Numer. Meth. Engrg.*, 18:1623–1654, 1982.

[125] A. Romeijn. The fatigue behaviour of multiplanar tubular joints. *Heron*, 39(3):1–86, 1994.

[126] G.J. Van Der Vegte. The static behaviour of axially loaded uniplanar and multiplanar tubular x-joints. *Heron*, 39(4):1–96, 1994.

[127] Air Force Materials Laboratory, Wright-Patterson Air Force Base. *Advanced Composite Design Guide*, third edition. vol. 1:1.21–3 edition, 1977. Cited in [129].

[128] E.A. Humphreys. Development of an engineering analysis of progressive damage in composites during low velocity impact. Technical Report NASA-CR-165778, Material Science Corporation, 1981.

[129] J.R. Vinson and R.L. Sierakowski. *The Behavior of Structures Composed of Composite Materials.* Martinnus Nijhoff Pub., Dordrecht, The Netherlands, 1987.

Appendix A

PLAMBS7 INPUT INSTRUCTIONS

The input data is composed of nine data sets:

I problem title;

II problem description and controls;

III mitre specification;

IV element layer and connectivities;

V nodal coordinates;

VI boundary conditions;

VII material specification;

VIII load generation information;

IX load increment.

The sets must be input in the order shown. All input are received free-formated but the implied integer (or real) classification of the implicit variables need be respected. Each mini table lists the items for one set of the data. Depending on previously input data variables, as many records as neccessary may have to be used for some data sets.

I Problem title

- one record required
- limited to 72 alphanumeric characters

II Problem and control variables

- one record required

NPOIN	total number of nodal points
NELEM	total number of elements in the mesh
LETYP	basic element type: LETYP = 1 : 9-noded Lagrange LETYP = 2 : 8-noded Serendipity LETYP = 3 : 9-noded Heterosis
NVFIX	total number of restrained boundary points : where one or more degrees of freedom are restrained.
NMATS	total number of different materials
NGAUS	order of in-plane integration for bending and membrane terms
NGAUZ	order of in-plane integration for shear terms
NGAUT	order of transverse integration per layer
NALGO	nonlinear solution algorithm: NALGO = 1 : initial method NALGO = 2 : tangential method NALGO = 3 : hybrid method–stiffness reformulation in the first iteration NALGO = 4 : hybrid method–stiffness reformulation in the second iteration
NINCS	total number of load increments
NLAYR	total number of layers across-the-thickness
LARGE	geometrically nonlinear control parameters LARGE = 0 : geometrically linear analysis LARGE = 1 : geometrically nonlinear analysis
NREST	restart facility parameter NREST = 0 : new analysis NREST = 1 : restart from previously converged analysis
NELTR	total number of transition elements in the mesh

III Mitre geometry

- one record required

ALPHA	mitre-angle
ARADI	mean pipe radius

IV Element layer and node numbers

- one record required for each element (total of NELEM records)
- element node numbers are received counterclockwise with respect to a starting corner node

- layers are numbered from bottom upwards

NUMEL	element number: (must be negative if transition element)
MATNO(NUMEL,ILAYR):	material identification number for layer ilayr (total of NLAYR entries)
LNODS(NUMEL,INODE):	element connectivities total of NNODE entries: NNODE = 8 or 10 for basic or transition Serendipity NNODE = 9 or 11 for basic or transition Heterosis NNODE = 9 or 11 for basic or transition Lagrange

V Nodal coordinates

- one record for each node
- midside nodes could be interpolated for straight edges
- central node could also be interpolated
- input must finish with the last node (NPOIN)
- nodal pressure is assumed positive

IPOIN	nodal point number (on midsurface)
COORD(IPOIN,1)	top x coordinate
COORD(IPOIN,2)	top y coordinate
COORD(IPOIN,3)	top z coordinate
COORD(IPOIN,4)	top nodal pressure
COORD(IPOIN,5)	bottom x coordinate
COORD(IPOIN,6)	bottom y coordinate
COORD(IPOIN,7)	bottom z coordinate
COORD(IPOIN,8)	bottom nodal pressure

VI Boundary condition

- one record required for each restrained node

  (total of NVFIX records)

  except for mitre-edge nodes, all displacements are prescribed in 'global' co-ordinate

ICFIX	restrained node number (must be negative for node(s) on the mitre-edge)

IFPRE	degrees of freedom restraint code : a five digit integer with each digit corresponding to u, v, w, β, and α degrees of freedom such that IFPRE = 1 : restrained IFPRE = 0 : free
PRESC(IVFIX,1)	prescribed nodal displacement value for u
PRESC(IVFIX,2)	prescribed nodal displacement value for v
PRESC(IVFIX,3)	prescribed nodal displacement value for w
PRESC(IVFIX,4)	prescribed nodal displacement value for β
PRESC(IVFIX,5)	prescribed nodal displacement value for α

VII Material specification

- as many as NMATS (different material) data sets

  (total of NMATS sets)

- four records required for each material

Record 1:	
NUMAT	material identification number
Record 2:	
PROPS(NUMAT,1)	E_1 Young modulus in 1-direction
PROPS(NUMAT,2)	ν_{12} poisson's ratio $(\nu_{21} = \nu_{12})$
PROPS(NUMAT,3)	ζ_k normalized layer thickness
PROPS(NUMAT,4)	ρ dummy input
PROPS(NUMAT,5)	ω dummy input
PROPS(NUMAT,6)	σ_{01} uniaxial yield stress in 1-direction
PROPS(NUMAT,7)	$H\prime$ strain-hardening parameter
Record 3:	
PROPS(NUMAT,8)	E_2 Young modulus in 2-direction
PROPS(NUMAT,9)	G_{12} shear modulus in $\overline{12}$-plane
PROPS(NUMAT,10)	G_{13} shear modulus in $\overline{13}$-plane
PROPS(NUMAT,11)	G_{23} shear modulus in $\overline{23}$-plane
PROPS(NUMAT,12)	σ_{02} uniaxial yield stress in 2-direction
PROPS(NUMAT,13)	σ_{03} uniaxial yield stress in 3-direction or σ_{012} uniaxial yield stress at 45^o to 1-direction
PROPS(NUMAT,14)	τ_{012} shear yield stress in $\overline{12}$-plane
Record 4:	
PROPS(NUMAT,15)	τ_{013} shear yield stress in $\overline{13}$-plane
PROPS(NUMAT,16)	τ_{023} shear yield stress in $\overline{23}$-plane
PROPS(NUMAT,17)	θ: angle between the reference system and the material system; in the layer plane measured counterclockwise in degrees

VIII Load generation information

- one record required

NDIVH	number of divisions in the hoop direction
ARADI	mean pipe radius
TMVAL	in-plane bending moment (closing is positive)
RPRES	internal (end-cap) pressure
THICK	mitre wall thickness
NELEM	total number of elements in the mesh
ILOAD	load generation code ILOAD = 0 : internal pressure ILOAD = 1 : in-plane bending

IX Applied load increment

- one record required (total of NINCS records)

FACTO	load fraction for current increment
TOLER	convergence tolerance (percent)
MITER	maximum number of iterations allowed
NOUTP(1)	a three digit initial output parameter corresponding to displacement, reaction and stress results at first iteration 1 : print 0 : do not print
NOUTP(2)	same as NOUTP(1) except for final output after a converged iteration

Appendix B

ISOPARAMETRIC FUNCTIONS

B.1 Basic-Elements

Each of these elements has an equal number of nodes on all sides. Thus such elements are 'basic' since they provide the same level of accuracy in all directions (ξ and η). That is to say they are geometrically isotropic. Figure B.1 provide a 'parent' (in $\xi - \eta$ space) and 'real' (in $x - y$ space) illustrations of the three (C^0-quadratic) basic-elements.

B.1.1 Generalized Procedure

As indicated in the figures, the real element may have arbitrary corner angles and side lengths (within allowable distortion limits), but the sides must be quadratic since the *iso*parametric mapping involved is quadratic along each side. The numbering of the nodes in consecutive and counterclock wise manner allows for a consistent automatic scheme when dealing with the transition-elements presented later.

To generate the parent shape functions for the C^0-quadratic isoparametric element, derivations based on indirect interpolatory procedure described in Refs. [94] and [107] are followed. The procedure consists of first generating the midside-node (2,4,6, and 8) from the corner-node (1,3,5, and 7) shape functions by *'subtracting'* suitable multiples of the midside interpolatory functions from a *starting* corner interpolatory function. The subtraction operation allows the starting corner interpolatory function to satisfy the necessary zero nodal value at the midside-node in addition to its interpolatory value of one at its own node. Thus the above method is mainly by inspection and intuition, but can be generalized to other elements.

By inspection, the shape function for midside node can be written as the product of a quadratic in ξ (or η) along one side times a linear in ξ (or η) along adjacent side. The starting interpolatory corner-node function can be written as the bilinear function which has value one (1) at its own node

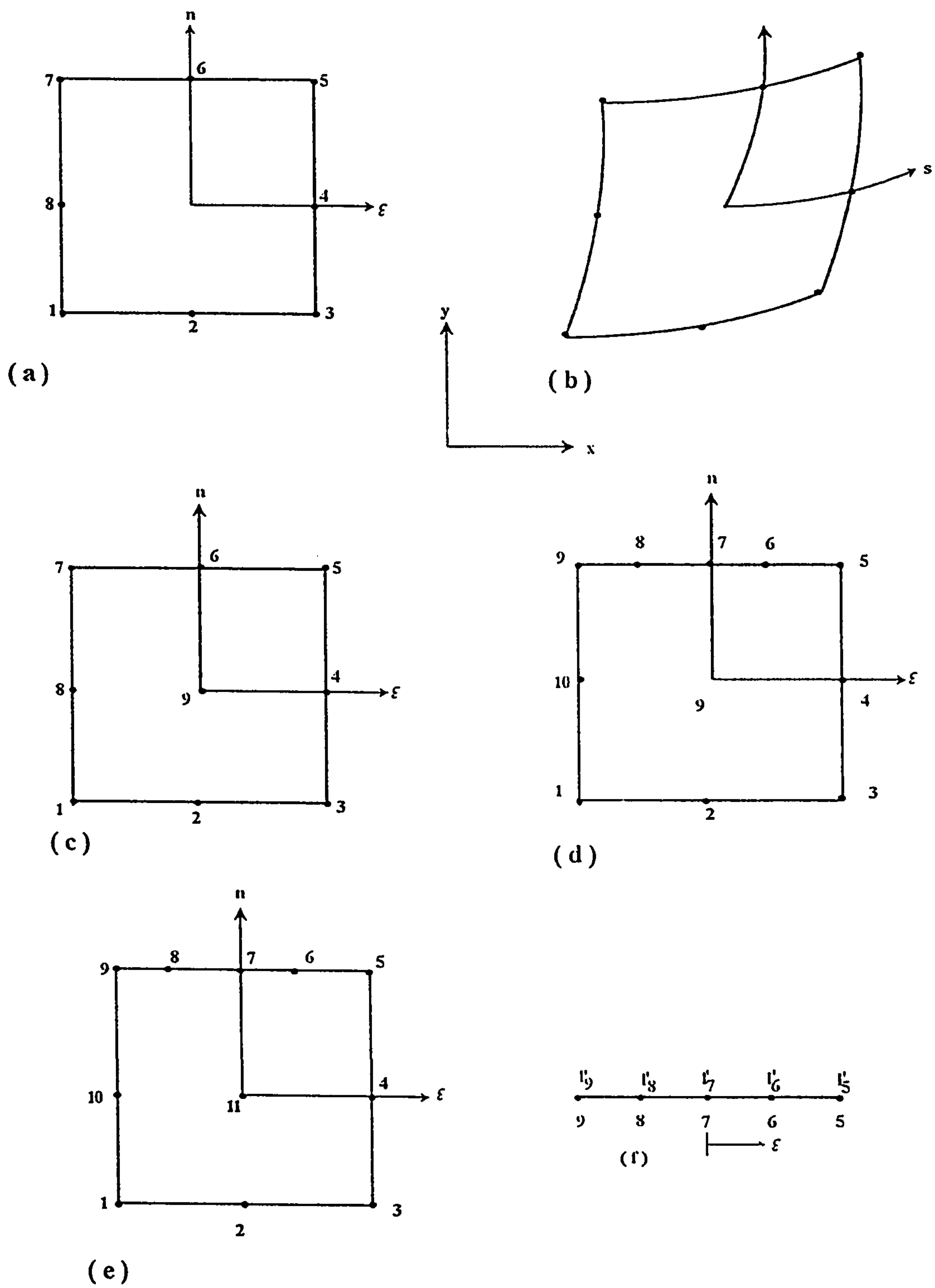

Figure B.1: Isoparametric elements (a) Serendipity parent basic-element (b) real element with parent element mapped onto it (c) Heterosis/Lagrange basic-element (d) Serendipity parent transition-element (e) Heterosis/Lagrange parent transition-element (f) numbering scheme for 1-D Lagrange interpolatory function.

and zero (0) at other corner-nodes. By generalizing the steps though, the shape functions for the midside-nodes are products of m*th*-degree polynomials in one variable (ξ or η) and a linear in the other (η or ξ); shape funtions for corner-nodes are bilinear polynomials minus multiples of the midside-node functions. This procedure makes it particularly easy to generate the corresponding transition-elements as will be shown later.

B.1.2 Serendipity/Heterosis

The 8-noded Serendipity is the second member of the 2-D serendipity family. Figure B.1a shows the parent element in $\xi - \eta$ space and Fig. B.1b shows the parent element mapped onto a real element in $x - y$ space. For the 8-noded Serendipity element in Fig. B.1a, the resulting expressions for the parent shape functions, in the $\xi - \eta$ space, are as follows:

Corner-nodes

$$\begin{aligned}
f_1(\xi,\eta) &= \frac{1}{4}(1-\xi)\,(1-\eta)\,(-\xi-\eta-1) \\
f_3(\xi,\eta) &= \frac{1}{4}(1+\xi)\,(1-\eta)\,(\xi-\eta-1) \\
f_5(\xi,\eta) &= \frac{1}{4}(1+\xi)\,(1+\eta)\,(\xi+\eta-1) \\
f_7(\xi,\eta) &= \frac{1}{4}(1-\xi)\,(1+\eta)\,(-\xi+\eta-1)
\end{aligned} \tag{B.1}$$

Midside-nodes

$$\begin{aligned}
f_2(\xi,\eta) &= \frac{1}{2}(1-\xi^2)\,(1-\eta) \\
f_4(\xi,\eta) &= \frac{1}{2}(1+\xi)\,(1-\eta^2) \\
f_6(\xi,\eta) &= \frac{1}{2}(1-\xi^2)\,(1+\eta) \\
f_8(\xi,\eta) &= \frac{1}{2}(1-\xi)\,(1-\eta^2)
\end{aligned} \tag{B.2}$$

To implement the Heterosis element, Fig. B.1c, use is made of hierarchical formulation [72] based on the 8-noded Serendipity functions. Hence the ninth central shape function, the bubble-function, takes the form:

$$f_9(\xi,\eta) = (1-\xi^2)\,(1-\eta^2) \tag{B.3}$$

B.1.3 Lagrange

Conceptually, the simplest and most direct way to develop the shape functions for the 9-noded Lagragian element is merely to form the product of two 1-D Lagrange interpolation polynomials. Performing the product operation, the 2-D shape functions obtained for the 9-noded Lagrange element are as follows:

Corner-nodes

$$\begin{aligned} f_1(\xi,\eta) &= \frac{1}{4}(1-\xi)\,(1-\eta)\,(\xi\eta) \\ f_3(\xi,\eta) &= \frac{1}{4}(1+\xi)\,(1-\eta)\,(-\xi\eta) \\ f_5(\xi,\eta) &= \frac{1}{4}(1+\xi)\,(1+\eta)\,(\xi\eta) \\ f_7(\xi,\eta) &= \frac{1}{4}(1-\xi)\,(1+\eta)\,(-\xi\eta) \end{aligned} \tag{B.4}$$

midside-nodes

$$\begin{aligned} f_2(\xi,\eta) &= \frac{1}{2}(1-\xi^2)\,(1-\eta)\,(-\eta) \\ f_4(\xi,\eta) &= \frac{1}{2}(1+\xi)\,(1-\eta^2)\,(\xi) \\ f_6(\xi,\eta) &= \frac{1}{2}(1-\xi^2)\,(1+\eta)\,(\eta) \\ f_8(\xi,\eta) &= \frac{1}{2}(1-\xi)\,(1-\eta^2)\,(-\xi) \end{aligned} \tag{B.5}$$

Central-node

$$f_9(\xi,\eta) = (1-\xi^2)\,(1-\eta^2) \tag{B.6}$$

B.2 Transition Elements

As indicated in Fig. B.1d and e, these elements contains two extra nodes on one side that do not have a basis in an adjoining element. The two extra nodes give rise to incomplete terms of degree 4,5 and 6 which makes the transition element an incomplete 2-D quartic (or quintic or sextic, etc.) on the corresponding side and complete quadratic on the remaining three sides. It is noted that in preparing for the formation of the transition-element shape functions, the nodes associated with the latter quadratic sides can directly take their shape functions from the corresponding basic-element shape functions since their behavior is still unaltered by the quartic side.

B.2.1 Supplementary Procedure

Based on the generalized procedure, the shape function for the quartic nodes can be written as quartic in one variable (ξ say) and a linear in the other (say η). Using the numbering scheme indicated in Fig. B.1f for the five quartic nodes, the resulting simplified 1-D quartic Lagrange interpolatory functions (in ξ) are then:

$$
\begin{aligned}
\ell\prime_5(\xi,\eta) &= \frac{1}{6}(4\xi^3 + 4\xi^2 - \xi - 1)\,(\xi) \\
\ell\prime_6(\xi,\eta) &= \frac{8}{6}(2\xi^3 + \xi^2 - 2\xi - 1)\,(-\xi) \\
\ell\prime_7(\xi,\eta) &= (4\xi^4 - 5\xi^2 + 1) \\
\ell\prime_8(\xi,\eta) &= \frac{8}{6}(2\xi^3 - \xi^2 - 2\xi + 1)\,(-\xi) \\
\ell\prime_9(\xi,\eta) &= \frac{1}{6}(4\xi^3 - 4\xi^2 - \xi + 1)\,(\xi) \qquad \text{(B.7)}
\end{aligned}
$$

With the quartic side at $\eta = +1$, the linear function (in η) would take the form $(1 + \eta)/2$ and is applicable to the Serendipity, the Heterosis and the Lagrange transition-elements.

The choice of what remains to form the five quartic shape functions follows a line of reasoning similar to that used for the generalized procedure. As such taking the product of the quartic functions in ξ, Eq. B.7, times the above linear function in η, the 2-D starting interpolatory functions corresponding to the five quartic nodes are:

$$
\begin{aligned}
\ell_5(\xi,\eta) &= \frac{1}{12}(4\xi^3 + 4\xi^2 - \xi - 1)\,(\xi)(1+\eta) \\
\ell_6(\xi,\eta) &= \frac{8}{12}(2\xi^3 + \xi^2 - 2\xi - 1)\,(-\xi)(1+\eta) \\
\ell_7(\xi,\eta) &= \frac{1}{2}(4\xi^4 - 5\xi^2 + 1)(1+\eta) \\
\ell_8(\xi,\eta) &= \frac{8}{12}(2\xi^3 - \xi^2 - 2\xi + 1)\,(-\xi)(1+\eta) \\
\ell_9(\xi,\eta) &= \frac{1}{12}(4\xi^3 - 4\xi^2 - \xi + 1)\,(\xi)(1+\eta) \qquad \text{(B.8)}
\end{aligned}
$$

Expressions for each of the transition-elements can thus be given according to the subdivision below.

B.2.2 Serendipity/Heterosis

Quadratic nodes

$$
\begin{aligned}
f_1(\xi,\eta) &= \frac{1}{4}(1-\xi)\,(1-\eta)\,(-\xi-\eta-1) \\
f_2(\xi,\eta) &= \frac{1}{2}(1-\xi^2)\,(1-\eta) \\
f_3(\xi,\eta) &= \frac{1}{4}(1+\xi)\,(1-\eta)\,(\xi-\eta-1) \\
f_4(\xi,\eta) &= \frac{1}{2}(1+\xi)\,(1-\eta^2) \\
f_{10}(\xi,\eta) &= \frac{1}{2}(1-\xi)\,(1-\eta^2)
\end{aligned}
\tag{B.9}
$$

Quartic nodes

$$
\begin{aligned}
f_5(\xi,\eta) &= \ell_5(\xi,\eta) - \frac{1}{2}f_4(\xi,\eta) \\
f_6(\xi,\eta) &= \ell_6(\xi,\eta) \\
f_7(\xi,\eta) &= \ell_7(\xi,\eta) \\
f_8(\xi,\eta) &= \ell_8(\xi,\eta) \\
f_9(\xi,\eta) &= \ell_9(\xi,\eta) - \frac{1}{2}f_{10}(\xi,\eta)
\end{aligned}
\tag{B.10}
$$

and the eleventh central node for the Heterosis is:

$$
f_{11}(\xi,\eta) = (1-\xi^2)\,(1-\eta^2) \tag{B.11}
$$

B.2.3 Lagrange

Quadratic nodes

$$
\begin{aligned}
f_1(\xi,\eta) &= \frac{1}{4}(1-\xi)\,(1-\eta)\,(\xi\eta) \\
f_2(\xi,\eta) &= \frac{1}{2}(1-\xi^2)\,(1-\eta)\,(-\eta) \\
f_3(\xi,\eta) &= \frac{1}{4}(1+\xi)\,(1-\eta)\,(-\xi\eta)
\end{aligned}
$$

$$
\begin{aligned}
f_4(\xi,\eta) &= \frac{1}{2}(1+\xi)\,(1-\eta^2)\,(\xi) \\
f_{10}(\xi,\eta) &= \frac{1}{2}(1-\xi)\,(1-\eta^2)\,(-\xi)
\end{aligned} \tag{B.12}
$$

Quartic nodes

$$
\begin{aligned}
f_5(\xi,\eta) &= \ell_5(\xi,\eta) - \frac{1}{2}f_4(\xi,\eta) \\
f_6(\xi,\eta) &= \ell_6(\xi,\eta) \\
f_7(\xi,\eta) &= \ell_7(\xi,\eta) - \frac{1}{2}f_{11}(\xi,\eta) \\
f_8(\xi,\eta) &= \ell_8(\xi,\eta) \\
f_9(\xi,\eta) &= \ell_9(\xi,\eta) - \frac{1}{2}f_{10}(\xi,\eta)
\end{aligned} \tag{B.13}
$$

Central node

$$
f_{11}(\xi,\eta) = (1-\xi^2)\,(1-\eta^2) \tag{B.14}
$$

Appendix C

EQUIVALENT LOADS

C.1 Introduction

Expressions for equivalent nodal loads are developed based on a side whose three-nodes are flushed with the free-edge across which the 'end-cap' part of the internal-pressure and the in-plane bending are transmitted. For the type of treatment considered here, no moments would originate. The following 1-D quadratic shape functions would be useful:

$$f_i(\eta) = \begin{cases} \frac{1}{2}\eta\,(\eta - 1) & ; \; i = 1 \\ (\eta + 1)\,(1 - \eta) & ; \; i = 2 \\ \frac{1}{2}(1 + \eta)\,\eta & : \; i = 3 \end{cases} \tag{C.1}$$

C.2 End-Cap Pressure

For a closed mitre under internal-pressure p_0, the 'end-cap' part of the pressure can be replaced by a uniformly distributed force (q) acting per unit length along the symmetric half-circumference (πa). For an element (e) whose side is adjacent to the free-edge, the consistent nodal load vector corresponding to the three nodes on that side can be written as

$$p_i^e = \int_s f_i^T(s) q ds \tag{C.2}$$

where s is the arc distance from the intrado and $f(s)$ is a quadratic shape function in s coordinate. By mapping to the η-space and noting that $ds = Jd\eta$, where $J = S^e/2$ is the Jacobian of the transformation, Eq. C.2 becomes

$$p_i^e = q\frac{S^e}{2}\int_{\eta=-1}^{\eta=+1} f_i^T(\eta)\, d\eta \tag{C.3}$$

Equation C.3 can be evaluated using Eq. C.1 to give

$$p_i^e = \begin{cases} q\frac{S^e}{6} & ; \ i = 1 \\ 4q\frac{S^e}{6} & ; \ i = 2 \\ q\frac{S^e}{6} & ; \ i = 3 \end{cases} \tag{C.4}$$

in which S^e is the element (arc) length along the symmetric half-circumference. Therefore the consistent nodal force vector p^e can be explicitly written in matrix form as

$$p_i^e = \begin{Bmatrix} p_1 \\ p_2 \\ p_3 \end{Bmatrix} = \frac{\pi a^2 p_0}{12 N_H} \begin{Bmatrix} 1 \\ 4 \\ 1 \end{Bmatrix} \tag{C.5}$$

It should be noted that for the internal-pressure, the value for a represents the internal radius of the mitre pipe rather than the pipe mean radius.

C.3 In-Plane Bending

Under in-plane bending, the state of stress at the free-edge of the mitre is essentially axial and assumes $\cos\theta$ distribution such that:

$$q = q_0 \cos\theta \tag{C.6}$$

where

$$q_0 = \frac{M}{\pi a^2} \tag{C.7}$$

Therefore, the equivalent nodal load vector will be:

$$p_i^e = \int_s f_i^T(\theta)\, q(\theta)\, ds \tag{C.8}$$

Transforming to $\xi - \eta$-space, the above equation after some expansion becomes:

$$p_i^e = J\, q_0 \int_\eta f_i^T(\eta) \cos\theta(\eta)\, d\eta \tag{C.9}$$

in which $f_i(\eta)$ is already defined in Eq. C.1 as the 1-D quadratic shape function and J is the Jacobian of the transformation. The angle $\theta(\eta)$ is therefore now a function of η through the relation $ad\theta = Jd\eta$. By exact integration of Eq. C.9 it can be shown that:

$$p_i^e = \left[\mu f_i(\eta)\sin\theta(\eta) + \mu^2 \frac{d}{d\eta} f_i(\eta)\cos\theta(\eta) - \mu^3 \frac{d^2}{d\eta^2} f_i(\eta)\sin\theta(\eta)\right]_{\eta=-1}^{\eta=+1} \tag{C.10}$$

where $\mu = a/J$.

Noticing that at $\eta = -1$, $\theta = \theta_1$ and at $\eta = +1$, $\theta = \theta_3$ and after getting the indicated derivatives using Eq. C.1, an explicit evaluation of Eq. C.10 for $i = 1, 2$, and 3 would give:

$$\begin{Bmatrix} p_1 \\ p_2 \\ p_3 \end{Bmatrix} = aq_0 \begin{Bmatrix} -\sin\theta_1 & \frac{1}{2}(\cos\theta_3 + 3\cos\theta_1) & -(\sin\theta_3 - \sin\theta_1) \\ 0 & -2(\cos\theta_3 + \cos\theta_1) & 2(\sin\theta_3 - \sin\theta_1) \\ \sin\theta_3 & \frac{1}{2}(3\cos\theta_3 + \cos\theta_1) & -(\sin\theta_3 - \sin\theta_1) \end{Bmatrix} \begin{Bmatrix} \mu \\ \mu^2 \\ \mu^3 \end{Bmatrix} \tag{C.11}$$

The nodal quantities θ_1 $(, \theta_2)$, and θ_3 are the angular positons (in radians) of the three nodes taking in the positive direction of the hoop angle θ.

Vita

- Aliyu Shazali Mohammed
- Hailed from Yola, Kano state, Nigeria.
- Received **B.Eng.**(Civil) Degree from Ahmadu Bello University (**ABU**), Zaria-Nigeria in September 1988.
- Worked with Abubakar Tafawa Balewa University (**ATBU**), Bauchi-Nigeria as a Graduate Assistant (1989-1992) and obtained **M.Eng.**(Struct.) Degree in February 1992.
- Joined the Department of Civil Engineering at King Fahd University of Petroleum and Minerals (**KFUPM**), Dhahran, Saudi Arabia as a Research Assistant in February 1992.
- Received **M.S.** Degree in Civil Engineering from KFUPM, Saudi Arabia in June 1995.